

FEDERAL UNIVERSITY OF ITAJUBÁ – UNIFEI  
MECHANICAL ENGINEERING INSTITUTE  
POSTGRADUATE PROGRAM IN MECHANICAL  
ENGINEERING

Rafael Augusto Gomes

Enhancing Mechanical Properties of  
Auxetic Structures through  
Optimization and Experimental Testing

Itajubá/MG

2024

FEDERAL UNIVERSITY OF ITAJUBÁ – UNIFEI  
MECHANICAL ENGINEERING INSTITUTE  
POSTGRADUATE PROGRAM IN MECHANICAL  
ENGINEERING

Rafael Augusto Gomes

# Enhancing Mechanical Properties of Auxetic Structures through Optimization and Experimental Testing

Dissertation submitted to the Postgraduate Program in Mechanical Engineering, from Mechanical Engineering Institute of the Federal University of Itajubá, as a requirement to obtain the title of Master of Science in Mechanical Engineering.

**Concentration area:** Design, Materials and Processes.

**Supervisor:** Prof. Dr. Guilherme Ferreira Gomes

**Co-supervisor:** Prof. Dr. Matheus Brendon Francisco

Itajubá/MG

2024

FEDERAL UNIVERSITY OF ITAJUBÁ – UNIFEI  
MECHANICAL ENGINEERING INSTITUTE  
POSTGRADUATE PROGRAM IN MECHANICAL  
ENGINEERING

Rafael Augusto Gomes

# Enhancing Mechanical Properties of Auxetic Structures through Optimization and Experimental Testing

Dissertation approved by the examining board on  
July 5th, 2024, awarding the author the title of  
**Master of Science in Mechanical Engineering.**

*Dissertation Committee*

Prof. Dr. Tulio Hallak Panzera (UFSJ)

Prof. Dra. Marília Sonego (UNIFEI)

Prof. Dr. Matheus Brendon Francisco (UNIFEI)

Prof. Dr. Guilherme Ferreira Gomes (UNIFEI)

Itajubá

2024

*I dedicate this work to the Lord God, who has allowed me to reach this professional stage. To my family, who, with love, have always supported me through challenges and achievements.*

# ACKNOWLEDGEMENTS

To my parents, Geovani and Vanuza, whose unwavering support and presence during the moments of this journey have been my constant source of strength and inspiration.

To my advisor, Prof. Dr. Guilherme Ferreira Gomes and co-advisor Prof. Dr. Matheus Brendon Francisco, whose patience, insightful guidance, meticulous corrections, and friendship have been invaluable. Thank you for sharing your knowledge and for being such an integral part of my academic journey.

To GEMEC (Grupo de Pesquisa em Métodos Numéricos e Otimização), it has been an honor to be a part of this research group. I am profoundly grateful for the opportunity to learn from and work alongside such talented and inspiring individuals.

To friends Bruno, Lucas, Rubens, and Marcos, for always being there, for your ideas, discussions, and countless moments of laughter. Your companionship and support have been invaluable throughout this journey, and to all my friends who have been with me every step of the way.

To the esteemed professors at UNIFEI from whom I have had the privilege to learn during my Master's program, and to the dedicated technicians whose assistance was instrumental in making this project possible.

To express my sincere gratitude to FAPEMIG for its invaluable financial support, which was instrumental in enabling the successful completion of this research.

*“All our dreams can come true  
if we have the courage to pursue them.”*

*Walt Disney.*

# RESUMO

Materiais e estruturas auxéticas têm atraído atenção devido às suas propriedades mecânicas, notadamente sua alta capacidade de absorver energia. Alguns tipos de estruturas tubulares auxéticas têm sido estudados e projetados para aplicação em diversos campos da engenharia, como engenharia mecânica, aeroespacial e médica. No presente estudo, inspirado pela forma da asa da libélula, uma nova célula unitária auxética foi desenvolvida e aplicada em uma estrutura tubular com o objetivo de propor uma nova estrutura com menor concentração de tensões e, conseqüentemente, maior absorção de energia. As células unitárias em forma de asa de libélula (DFW) foram integradas em uma estrutura tubular, e amostras experimentais foram produzidas utilizando um processo de manufatura aditiva. Para validar a capacidade de absorção de energia da nova célula unitária, foi feita uma comparação com a estrutura tubular auxética reentrante clássica usando dois parâmetros diferentes: peso e número de células unitárias, que foram desenvolvidas em duas diferentes estruturas DFW. Os resultados dos testes de compressão mostraram que a forma inspirada na asa da libélula, em ambas as configurações propostas, demonstrou excelente absorção de energia em comparação com a estrutura reentrante clássica. Especificamente, a estrutura com a mesma quantidade de células unitárias e a estrutura com o mesmo peso absorveram 163% e 79% mais energia, respectivamente. Subseqüentemente, foi conduzido um processo de otimização para aprimorar as propriedades mecânicas da estrutura. Um framework de otimização foi implementado para minimizar simultaneamente três objetivos estruturais críticos: razão de Poisson, massa e tensões. Simulações numéricas facilitaram a metamodelagem via o método de superfície de resposta, criando modelos substitutos que representam com precisão cada variável de resposta. Uma técnica de otimização metaheurística, o Algoritmo Genético de Ordenação Não-dominada (NSGA-II), foi então empregada para otimizar essas respostas para desempenho em compressão. A validação experimental corroborou os achados numéricos, com duas configurações otimizadas propostas. O primeiro design (TOPSIS 1) apresentou reduções na razão de Poisson de até 3% e nas tensões de 45%, enquanto o segundo design (TOPSIS 2) demonstrou uma redução nas tensões de 537%. Adicionalmente, a validação experimental revelou melhorias significativas nas capacidades de absorção de energia, com TOPSIS 1 e TOPSIS 2 aumentando a absorção de energia em 58% e 545%, respectivamente, em comparação com a estrutura de referência. O presente estudo apresenta o potencial significativo das estruturas auxéticas bio-inspiradas para aplicações de alta complexidade que exigem alta capacidade de absorção de energia.

**Palavras-chaves:** Auxético; Estruturas Tubulares; Coeficiente de Poisson Negativo; Otimização; Manufatura Aditiva.

# ABSTRACT

Auxetic materials and structures have been attracting attention due to their mechanical properties, also the notably their high capacity to absorb energy. Some types of auxetic tubular structures have been studied and designed for application in diverse engineering fields such as mechanical, aerospace, and medical engineering. In the present study, inspired by the dragonfly wing shape, a novel auxetic unit cell was developed and applied in a tubular structure with the goal of proposing a new structure with lower stress concentration and consequently increased energy absorption. The dragonfly wing (DFW) shaped unit cells were integrated into a tubular structure, and experimental samples were produced using an additive manufacturing process. To validate the energy absorption capability of the novel unit cell, a comparison was made with the classical reentrant auxetic tubular structure using two different parameters: weight and the number of unit cells, which were developed in two different DFW structures. The results from the compression tests showed that the bio-inspired dragonfly wing shape, in both proposed configurations, demonstrated excellent energy absorption compared to the classical reentrant structure. Specifically, the structure with the same quantity of unit cells and the structure with the same weight absorbed 163% and 79% more energy, respectively. Subsequently, an optimization process was conducted to enhance the mechanical properties of the structure. An optimization framework was implemented to simultaneously minimize three critical structural objectives: Poisson's ratio, mass, and stress. Numerical simulations facilitated metamodeling via the response surface method, creating surrogate models that accurately represent each response variable. A metaheuristic optimization technique, the Non-dominated Sorting Genetic Algorithm (NSGA-II), was then employed to optimize these responses for compression performance. Experimental validation supported the numerical findings, with two optimized designs proposed. The first design (TOPSIS 1) showed reductions in Poisson's ratio by up to 3% and stress by 45%, while the second design (TOPSIS 2) demonstrated a stress reduction of 537%. Additionally, experimental validation revealed significant improvements in energy absorption capabilities, with TOPSIS 1 and TOPSIS 2 increasing energy absorption by 58% and 545%, respectively, compared to the baseline. The present study present the significant potential of bio-inspired auxetic structures for high complexity applications requiring high energy absorption capacity.

**Key-words:** Auxetic; Tubular structures; Negative Poisson's Ratio; Optimization; Additive Manufacture.



# LIST OF FIGURES

Figure 1.1 – Difference between (a) a non-auxetic material and (b) a auxetic material (adapted from [3]). . . . .	19
Figure 1.2 – Circular tubes in nature: (a) tubular sheep horn (adapted from [18]), (b) bamboo (adapted from [19]), (c) human bone (adapted from [20]), (d) blood vessel (adapted from [21]). . . . .	20
Figure 3.1 – (a) Number of publications on the topic of auxetic tubular structures per year since 2001, (b) Countries where researchers are studying the auxetic tubular structure, (c) Institutions of auxetic tubular structure research. . . . .	25
Figure 3.2 – Auxetic structures: (a) re-entrant honeycomb [43], (b) S-shaped [44], (c) Star-shaped [45], (d) rotational [46], (e) Double Arrowhead [47], (f and g) Missing Rib [48], (h and i) Perforated [49], (j) Elliptical [50], (k) Hexachiral structures [51], (l) Anti-tetrachiral structures [51], (m) Trichiral structures [51], (n) Anti-trichiral structures [51], and (o) Tetrachiral structures [51]. . . . .	26
Figure 3.3 – Auxetic structures: (a) Hybrid reentrant honeycomb [56], (b) Reentrant hexagonal honeycomb [57], (c) Hybrid reentrant-chiral [58], (d) Reentrant missing rib [59], (e) S-shape with star [60], and (f) Chiral reentrant [61]. . . . .	28
Figure 3.4 – Poisson’s ratio behavior of tubular structures under tensile load: (a) non-auxetic tube; (b) auxetic tube (adapted from [63]). . . . .	30
Figure 3.5 – Analyses of the percentage of the auxetic tubular structure models that are more commonly used. . . . .	33
Figure 3.6 – Auxetic tubular structure energy absorption, correlation of FEA numerical simulations and experimental tests (adapted from [50]). . . . .	36
Figure 3.7 – Compression tests comparison between the FEA numerical simulations and the experimental tests in the peanut-shaped hole auxetic tubular structure (adapted from [69]). . . . .	36
Figure 3.8 – Numerical results of (a) compression analysis, (b) buckling analysis, and (c) mode shapes (adapted from [32]). . . . .	37
Figure 3.9 – Comparison of the auxetic tubular structure geometry: (a) non-optimized to (b) optimized (adapted from [30]). . . . .	39
Figure 3.10–Comparison of the auxetic tubular structure geometry: (a) non-optimized to (b) optimized (adapted from [32]). . . . .	40

Figure 3.11–Comparison of energy absorption (EA) per displacement between the double-V structures without optimization and the optimized structure (adapted from [30]). . . . .	41
Figure 3.12–Additive manufacturing: (a) 3D printing process; (b) auxetic tube (adapted from [32]). . . . .	43
Figure 3.13–The recovery behavior of two examples of deformed structures after compression testing, being released and processed with heating and cooling treatment (adapted from [10]). . . . .	44
Figure 3.14–The cutting process and the fabricated specimens of auxetic tubes: (a) laser cutting; (b) auxetic tube (adapted from [50]). . . . .	45
Figure 3.15–The braided fabrication process of the auxetic tubular structures (a) The braiding machine used; (b) The schematic of the braiding process (adapted from [120]). . . . .	47
Figure 3.16–Comparison of cross-sectional shapes in folding regions under quasi-static loading: (a) anti-tetrachiral tube; (b) arrow tube; (c) reentrant tube; and (d) honeycomb tube (adapted from [16]). . . . .	50
Figure 3.17–Comparison of cross-sectional shapes in folding regions under quasi-static loading: (a) solid tube; (b) reentrant tube; and (c) honeycomb tube (adapted from [16]). . . . .	51
Figure 3.18–The deformed and undeformed shape of cellular tubes compared to conventional tubes with different aspect ratios (adapted from [92]). . .	52
Figure 3.19–The schematic of the manufacturing process of foam-filled tubes [16]. .	53
Figure 3.20–Comparison of auxetic and non-auxetic tubes deformation modes under quasi-static loading: (a) REF, (b) ARF, (c) ACF, and (d) HOF [16]. . .	54
Figure 3.21–(a) Design of an extension-induced structure, (b) Finite Element Analysis of the structure, and (c) Experimental analyses (adapted from [7]).	55
Figure 3.22–Typical forms of buckling collapse observed in the numerical simulations: the ripple pattern formed at the compressed side and evolves into a single kink (adapted from [86]). . . . .	56
Figure 3.23–Typical forms of buckling collapse observed in the numerical simulations: the ripple pattern forms at the compressed side and evolves into a single kink (adapted from [129]). . . . .	56
Figure 3.24–Auxetic structures unit cell diagrams: (a) Reentrant [130], (b) Arrow-head [131], (c) Chiral [52] and (d) Rotational squares [46]. . . . .	57
Figure 3.25–Comparison between experiments and numerical simulation (a) Stress-strain curves from repeated mechanical tests and numerical prediction (b) Evolution of Poisson’s ratio as a function of applied strain (c) and (d) Measured and simulated deformation patterns(adapted from [91]). .	59

Figure 3.26–The schematic of oesophageal stent placement (a), and the diagram of a stent inserted into a stenosed vessel (b), (adapted from [138], [86]). . . . .	62
Figure 3.27–Illustration of auxeticity for auxetic nails: (a) During push-in and pull-out, (b) 3D-printed different types of nails in four nail groups using brass and stainless steel material (adapted from [105]). . . . .	63
Figure 3.28–Conceptual automotive applications of auxetic tubular structure: (a) NPR bumper system (adapted from [142]), (b) energy absorbers used in vehicle safety (adapted from [144]), (c) FEM model of the FEM crash box (adapted from [22]), and (d) Implementation of a star-shaped tube-bean structure into the front door (adapted from [143]). . . . .	64
Figure 4.1 – Dragonfly-wing-shape pattern [149]. . . . .	68
Figure 4.2 – Flowchart of dragonfly-wing-shape unit cell geometric parametrization. . . . .	68
Figure 4.3 – The influence of $r_1$ and $r_2$ in the relative density of the DFW unit cell. . . . .	70
Figure 4.4 – Negative Poisson’s behavior of the DFW unit cell applied in the tubular structure: (a) undeformed, (b) under compression, and (c) under traction. . . . .	70
Figure 4.5 – Auxetic tubular structure: (a) DFW-A auxetic tubular structure and (b) DFW-B auxetic tubular structure. . . . .	72
Figure 4.6 – Auxetic tubular structure: (a) Reentrant unit cell parametrization and (b) Reentrant auxetic tubular structure (adapted from [32]). . . . .	73
Figure 4.7 – Material proprieties: (a) printing process, (b) compression sample test, (c) compression test, (d) stress vs strain curve. . . . .	74
Figure 4.8 – Finite element methodology process: (a) DFW-A, (b) DFW-B, and (c) RE. . . . .	75
Figure 4.9 – Printing process of the structure using PLA and final auxetic structure: (a) DFW-A, (b) DFW-B, and (c) RE. . . . .	76
Figure 4.10–Experimental test setup. . . . .	77
Figure 4.11–Auxetic structure from DIC: (a) DFW-A, (b) DFW-B, and (c) Reentrant. . . . .	78
Figure 4.12–Numerical Von-Misses stress ratio: (a) DFW-A, (b) DFW-B, and (c) RE. . . . .	79
Figure 4.13–The comparison of deformation model between EXP and FEM: (a) DFW-A, (b) DFW-B, and (c) RE. . . . .	80
Figure 4.14–Numerical <i>vs.</i> Experimental Poisson’s ratio results. . . . .	81
Figure 4.15–Main Effect Chart: (a) Stress, (b) Poisson. . . . .	82
Figure 4.16–Compression results for the auxetic tubular structures: (a) DFW-A, (b) DFW-B, and (c) RE. . . . .	84
Figure 4.17–Compression results for the DFW-A auxetic tubular structures. . . . .	84
Figure 4.18–Compression results for the DFW-B auxetic tubular structures. . . . .	85
Figure 4.19–Compression results for the RE auxetic tubular structures. . . . .	85
Figure 4.20–Experimental energy absorption results for the auxetic tubular structures: (a) DFW-A, (b) DFW-B, and (c) Reentrant. . . . .	86

Figure 4.21–Experimental specific energy absorption results for the auxetic tubular structures: (a) DFW-A, (b) DFW-B, and (c) RE. . . . .	86
Figure 4.22–Comparison of the mechanical proprieties (legend: ■ DFW-A, ■ DFW-B, ■ Reentrant). . . . .	87
Figure 5.1 – NSGA-II algorithm structure (adapted from [155]). . . . .	93
Figure 5.2 – Metal models CAD generated from the RSM data. . . . .	96
Figure 5.3 – Material Proprieties: (a) ASTM D638 parameters, (b) Samples, (c) Traction test, (d) Stress vs Strain curve. . . . .	97
Figure 5.4 – Finite Element Method: (a) SOLID 187, (b) Auxetic tubular structure meshes without convergence, (c) Auxetic tubular structure meshes with convergence. . . . .	98
Figure 5.5 – Manufacture Process: (a) Printing process, (b) BaseLine, (c) TOPSIS 1 and (d) TOPSIS 2. . . . .	100
Figure 5.6 – Quasi-static compression test setup: (b) BaseLine, (c) TOPSIS 1 and (d) TOPSIS 2. . . . .	101
Figure 5.7 – Pareto Chart: (a) Poisson, (b) Mass, (c) Stress. (Legend: A: r1, B: r2 and C: t). . . . .	103
Figure 5.8 – Main Effect Chart: (a) Poisson, (b) Mass, (c) Stress. . . . .	104
Figure 5.9 – Experimental responses plotted by pairs around the center point in one variable. . . . .	105
Figure 5.10–Pareto Surface (○ non-dominated solutions and ★ Topsis solution). . . . .	106
Figure 5.11–Auxetic tubular structures: (a) Baseline, (b) Nadir 1, (c) Nadir 2, (d) Nadir 3. . . . .	107
Figure 5.12–Optimized Structures: (a) TOPSIS 1, (b) TOPSIS 2. . . . .	108
Figure 5.13–Finite Element Analysis: (a) Stress of the baseline, (b) Displacement of the baseline, (c) Stress of the TOPSIS 1, (d) Displacement of the TOPSIS 1, (e) Stress of the TOPSIS 2, (f) Displacement of the TOPSIS 2. . . . .	109
Figure 5.14–Compression results for the auxetic tubular structures: Baseline, TOPSIS 1 and TOPSIS2. . . . .	112
Figure 5.15–Energy absorption of Baseline, TOPSIS 1 and TOPSIS 2. . . . .	112
Figure 5.16–Specific Energy Absorption of Baseline, TOPSIS 1 and TOPSIS 2. . . . .	113
Figure 5.17–Graphical visualization of structure properties (legend: — Baseline, — TOPSIS 1, — TOPSIS 2). . . . .	114
Figure 5.18–Displacement Explicitly Dynamic Finite Element Analysis: (a) Baseline, (b) TOPSIS 1, (c) TOPSIS 2. . . . .	115
Figure 5.19–Numerical Poisson ratio result. . . . .	116

# LIST OF TABLES

Table 3.1 – Types of tubular auxetic structure. . . . .	34
Table 3.2 – Numerical analyses performed in tubular auxetic structures. . . . .	38
Table 3.3 – Types of auxetic tubular structure manufactured by additive manufacturing. . . . .	42
Table 3.4 – Energy absorption analyses of different types of auxetic tubular structures. . . . .	49
Table 4.1 – Parameters of the auxetic dragonfly-wings-shape unit cell used in the tube construction. . . . .	72
Table 4.2 – Parameters of the auxetic reentrant cell used in the tube construction. . . . .	73
Table 4.3 – Properties of PLA (ASTM D695 ). . . . .	74
Table 4.4 – Experimental results of auxetic tubular structures manufactured with PLA filament . . . . .	87
Table 5.1 – Lower and upper bounds for the design variables. . . . .	95
Table 5.2 – Properties of high performance resin (ASTM D638). . . . .	97
Table 5.3 – Design of experiments and responses of a DFW auxetic tubular structure. . . . .	102
Table 5.4 – Regression coefficients with corresponding P-Values. . . . .	103
Table 5.5 – Model Summary Table for fit regression model. . . . .	105
Table 5.6 – Nadir solutions of the Pareto surface. . . . .	107
Table 5.7 – TOPSIS solutions of the Pareto surface. . . . .	107
Table 5.8 – Parameters of the auxetic DFW tubular structure. . . . .	110
Table 5.9 – Comparing Optimized Model to Finite Element Analysis (FEA). . . . .	110
Table 5.10–Comparison of Baseline FEM values to TOPSIS 1 and TOPSIS 2. . . . .	110
Table 5.11–Comparison of Baseline FEM values to TOPSIS 1 and TOPSIS 2. . . . .	113

# ABBREVIATIONS AND ACRONYMS

<i>AM</i>	Additive Manufacturing
<i>b</i>	Base of the unit cell (mm)
<i>CAD</i>	Computer Aided Design
<i>CNC</i>	Computerized Numerical Control
<i>d</i>	Loading displacement
$D_i$	Inner diameter (mm)
$D_o$	Outer diameter (mm)
<i>DED</i>	Direct Energy Deposition
<i>DFW</i>	Dragonfly-wing shape
<i>DIC</i>	Digital Image Correlation
<i>DOE</i>	Design of Experiments
<i>E</i>	Young's modulus (MPa or GPa)
<i>EA</i>	Energy Absorption (J)
<i>e</i>	Edge thickness (mm)
<i>Et</i>	Tangent Modulus (MPa)
<i>ESO</i>	Evolutionary Structural Optimization
<i>FDM</i>	Fused Deposition Modeling
<i>FEA</i>	Finite Element Analysis
<i>FEM</i>	Finite Element Methodology
<i>G</i>	Shear Modulus (MPa or GPa)
<i>GEMEC</i>	Grupo de Estudos em Mecânica Experimental e Computacional
<i>h</i>	Length of the unit cell (mm)
<i>K</i>	Bulk Modulus (MPa or GPa)
<i>L</i>	Length of the structure (mm)
<i>LCD</i>	Laser Cladding Deposition
<i>LOM</i>	Laminated Object Manufacturing
<i>m</i>	Mass (g)
<i>MCF</i>	Main Crushing Force (N)
<i>MJF</i>	Multijet Fusion
<i>MOPSO</i>	Multi-Objective Particle Swarm Optimization
$N_h$	Number of the unit cell composed in the horizontal direction
$N_v$	Number of the unit cell composed in the vertical direction
<i>NPR</i>	Negative Poisson's Ratio
<i>NSGA – II</i>	Non-Dominated Sorting GA

<i>PCL</i>	Polycaprolactone
<i>PLA</i>	Polylactic Acid
<i>PPR</i>	Positive Poisson's Ratio
$\rho$	Density of the structure's material (kg/m <sup>3</sup> )
$\bar{\rho}$	Relative density
$\rho_r$	Ratio of the apparent density of the cellular structure
$\rho_s$	Density of the cellular structure's material
$r_1$	Radius of the first circumference (mm)
$r_2$	Radius of the second circumference (mm)
<i>RE</i>	Reentrant
<i>RSM</i>	Response Surface Methodology
<i>Sd</i>	Standard Deviation
<i>SEA</i>	Specific Energy Absorption (J/g)
<i>SLA</i>	Stereolithography
<i>SLM</i>	Selective Laser Melting
<i>SLS</i>	Selective Laser Sintering
<i>t</i>	Thickness (mm)
<i>T</i>	Structure thickness (mm)
<i>TPU</i>	Thermoplastic polyurethane
<i>x</i>	Center distance (mm)
<i>ZPR</i>	Zero Poisson's Ratio
$\sigma$	Stress (MPa)
$\sigma_f$	Failure Stress (MPa)
$\sigma_u$	Max. Stress (MPa)
$\sigma_y$	Yield Stress (MPa)
$\mathcal{F}_1$	Mass (g)
$\mathcal{F}_2$	Poisson
$\mathcal{F}_3$	Stress (MPa)
$\nu$	Poisson's ratio
$\varepsilon_x$	strains in the $x$ direction
$\varepsilon_y$	strains in the $y$ direction
$\varepsilon_z$	strains in the $z$ direction
$\lambda$	$\lambda = r_1/r_2$

# CONTENTS

<b>1</b>	<b>INTRODUCTION</b>	<b>19</b>
<b>2</b>	<b>RESEARCH OBJECTIVES</b>	<b>23</b>
<b>3</b>	<b>THEORETICAL REVIEW</b>	<b>24</b>
<b>3.1</b>	<b>RESEARCH CONTRIBUTORS</b>	<b>24</b>
<b>3.2</b>	<b>DESIGN OF NPR STRUCTURES</b>	<b>25</b>
3.2.1	DESIGN OF HYBRID AUXETIC STRUCTURE	28
3.2.2	DESIGN OF TUBULAR AUXETIC STRUCTURE	29
<b>3.3</b>	<b>NUMERICAL ANALYSIS, OPTIMIZATION AND MANUFACTURE</b>	<b>35</b>
3.3.1	NUMERICAL ANALYSIS OF AUXETIC TUBULAR STRUCTURE	35
3.3.2	OPTIMIZATION OF AUXETIC TUBULAR STRUCTURES	38
3.3.3	AUXETIC TUBULAR STRUCTURES MANUFACTURING PROCESS	41
3.3.3.1	ADDITIVE MANUFACTURE	41
3.3.3.1.1	3D PRINTING:	41
3.3.3.1.2	4D PRINTING:	43
3.3.3.2	LASER CUTTING	44
3.3.3.3	TEXTILE MANUFACTURE	46
<b>3.4</b>	<b>MECHANICAL PROPERTIES OF AUXETIC TUBULAR STRUCTURES</b>	<b>47</b>
3.4.1	ENERGY ABSORPTION	48
3.4.1.1	THE ENERGY ABSORPTION CAPACITY OF THE AUXETIC TUBULAR STRUCTURE IN COMPARISON TO THE CONVENTIONAL TUBULAR STRUCTURE	50
3.4.1.2	FOAM-FILLED HOLLOW AUXETIC TUBULAR STRUCTURE	52
3.4.2	TWIST DEFORMATION	54
3.4.3	BENDING PERFORMANCE	55
3.4.4	NEGATIVE POISSON'S RATIO AND SPECIFIC YOUNG'S MODULUS	57
3.4.4.1	NEGATIVE POISSON'S RATIO (NPR)	57
3.4.4.2	SPECIFIC YOUNG'S MODULUS	60
<b>3.5</b>	<b>APPLICATIONS OF AUXETIC TUBULAR STRUCTURES</b>	<b>61</b>
3.5.1	MEDICAL	61
3.5.2	NAILS	62
3.5.3	AUTOMOTIVE	63
<b>4</b>	<b>A NOVEL DRAGONFLY WING SHAPE AUXETIC TUBULAR STRUCTURE WITH NEGATIVE POISSON'S RATIO</b>	<b>65</b>



<b>4.1</b>	<b>CHAPTER INTRODUCTION</b>	<b>65</b>
<b>4.2</b>	<b>DRAGONFLY-WING-SHAPED MODEL (DFW)</b>	<b>67</b>
4.2.1	TUBULAR STRUCTURE DESIGN	71
4.2.1.1	TUBULAR DRAGONFLY-WINGS-SHAPE (DFW)	71
4.2.1.2	REENTRANT (RE)	72
4.2.2	MATERIAL PROPERTIES	73
4.2.3	FINITE ELEMENT MODELING SIMULATIONS	75
<b>4.3</b>	<b>EXPERIMENTAL STUDY</b>	<b>76</b>
4.3.1	SAMPLES MANUFACTURING	76
4.3.2	COMPRESSIVE TEST	77
4.3.2.1	DIGITAL IMAGE CORRELATION (DIC)	77
<b>4.4</b>	<b>NUMERICAL-EXPERIMENTAL RESULTS</b>	<b>78</b>
4.4.1	COMPARATIVE ANALYSIS: EXPERIMENTAL FINDINGS AND NUMERICAL SIMULATIONS	78
4.4.2	MECHANICAL PROPRIETIES	83
<b>4.5</b>	<b>CHAPTER CONCLUSION</b>	<b>88</b>
<b>5</b>	<b>OPTIMIZATION OF AUXETIC TUBULAR STRUCTURES WITH DRAGONFLY-WING-SHAPE CELLS THROUGH ADVANCED MULTI-OBJECTIVE OPTIMIZATION TECHNIQUES</b>	<b>90</b>
<b>5.1</b>	<b>CHAPTER INTRODUCTION</b>	<b>90</b>
5.1.1	RESPONSE SURFACE METHOD (RSM)	92
5.1.2	MULTI-OBJECTIVE NON-DOMINATED SORTING GA (NSGA-II)	93
<b>5.2</b>	<b>Numerical-Experimental Methodology</b>	<b>95</b>
5.2.1	DFW STRUCTURE META-MODELLING THROUGH RSM	95
5.2.2	TUBULAR META-STRUCTURE DESIGN	95
5.2.3	NUMERICAL MODEL	96
5.2.3.1	MATERIAL PROPERTIES	96
5.2.3.2	NUMERICAL ANALYSIS	97
5.2.4	MULTI-OBJECTIVE PROBLEM STATEMENT	99
5.2.5	EXPERIMENTAL VALIDATION	99
5.2.5.1	SAMPLES MANUFACTURING	99
5.2.5.2	QUASI-STATIC COMPRESSIVE TEST	100
<b>5.3</b>	<b>RESULTS AND DISCUSSION</b>	<b>101</b>
5.3.1	RSM ANALYSIS	101
5.3.2	MULTI OBJECTIVE DESIGN OPTIMIZATION	106
5.3.3	QUASI-STATIC COMPRESSION: TEST RESULTS AND ANALYSIS	111
<b>5.4</b>	<b>CHAPTER CONCLUSION</b>	<b>116</b>
<b>6</b>	<b>FINAL REMARKS</b>	<b>118</b>

**Bibliography** . . . . . 120

# 1 INTRODUCTION

Over the decades, the need to develop new materials and structures capable of meeting the stringent specifications of engineering projects in various fields has emerged. This includes sectors such as aeronautical, aerospace, automotive, medical, and sports industries, where there is growing interest in structures that demonstrate exceptional mechanical properties and performance surpassing those of traditional structures.

Moreover, as advancements in material and design science have propelled the development of structures with exceptional mechanical properties, attention has increasingly turned towards innovative solutions. One such intriguing development arises from understanding the counter intuitive behavior of certain materials. While conventional materials elongate in the direction of stretch and thin in cross-section, a paradigm shift occurs with materials possessing a Negative Poisson's Ratio (NPR). These materials, termed auxetic structures, exhibit a rare characteristic where they contract laterally under compression and expand laterally when stretched. This phenomenon, initially reported by Lakes in 1987 [1] and later called auxetic by Evans in 1991 [2], derived from the Greek word "*auxetos*" where it opens new possibilities for engineering applications across various industries.

Figure 1.1 presents the comparison and the difference between the non-auxetic structure and the auxetic structure.

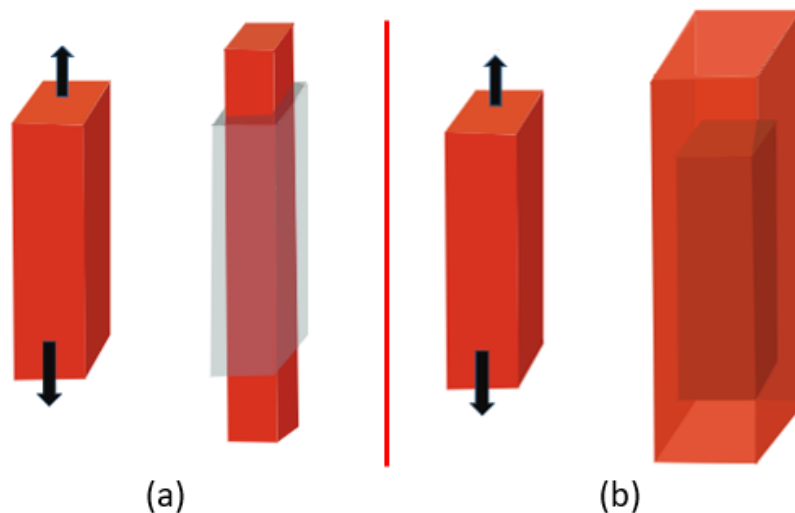


Figure 1.1 – Difference between (a) a non-auxetic material and (b) a auxetic material (adapted from [3]).

Most auxetic materials documented in the literature are polymers, which tend to have poor mechanical stress resistance. One potential solution to this issue is to design structures using materials with a Positive Poisson's Ratio (PPR) that exhibit auxetic behavior. This can be achieved through the configuration of unit cell designs in the struc-

ture, which produce a negative Poisson's ratio behavior. Examples of such designs include reentrant, chiral, anti-chiral, double-V, and perforated models. Each of these models has its own advantages and disadvantages, and the choice of geometry and material depends on the specific application of the structure and the manufacturing tools available [4], [5].

In contrast, nature is often used as inspiration to create many designs applied in diverse fields such as civil engineering, mechanical engineering, and medicine around the world. The case of auxetics is no different, where many authors have been proposing novel unit cells inspired by nature, composed of NPR behavior, with goals to improve the mechanical properties of structures and expand their applications. For instance, Zhang *et al.* [6] developed a novel butterfly-shaped auxetic structure with a NPR and enhanced stiffness. Farrell *et al.* [7] developed an auxetic cylindrical structure inspired by deformed cell ligaments. Wang *et al.* [8] developed an auxetic structure inspired by the peanut shape. Hamzehei *et al.* [9], inspired by the 2D image of a DNA molecule, introduced a 2D Zero Poisson's Ratio (ZPR) bio-inspired metamaterial. Additionally, the same author, Hamzehei *et al.* [10], recently presented a novel class of bio-inspired materials based on a parrot's beak, applied to a cylindrical metamaterial.

Auxetic models, when compared to conventional structures, demonstrate a range of superior mechanical properties. These properties include exceptional energy absorption capabilities [11, 12], outstanding bending performance [13], enhanced shear modulus and resistance to indentation [2], superior twist deformation [7], and significantly improved fracture toughness [14].

Additionally, it's important to highlight that the second structure under discussion is the tubular structure, a prevalent component in various engineering fields. Tubular structures are commonly encountered in everyday life, such as in sports stadiums, buildings, and bridges. Circular shapes can also be found in natural and biological structures like blood vessels, the trachea, sheep horns, and the stems of many plants, including bamboo. Figure 1.2 illustrates some of these natural tubular structures. Research indicates that tubular structures possess excellent mechanical properties, particularly in terms of impact energy absorption and crashworthiness [15, 16, 17].

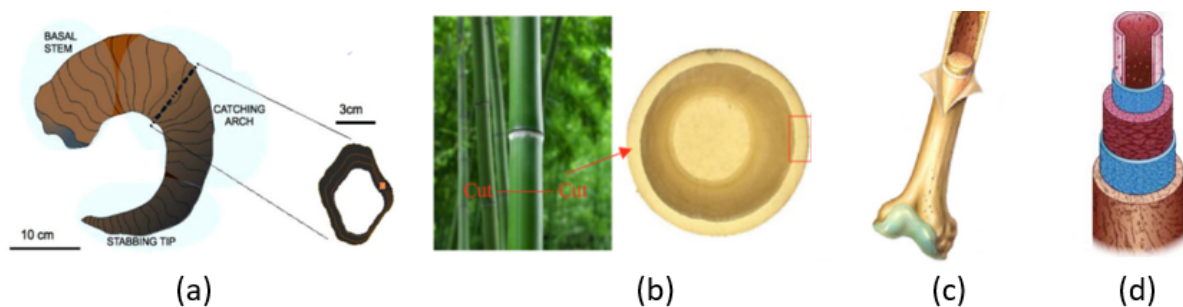


Figure 1.2 – Circular tubes in nature: (a) tubular sheep horn (adapted from [18]), (b) bamboo (adapted from [19]), (c) human bone (adapted from [20]), (d) blood vessel (adapted from [21]).

Combining the excellent mechanical properties of tubular structures with the unique behavior of NPR structures, auxetic tubular structures have garnered significant attention from researchers. Due to their distinctive characteristics, auxetic tubular structures are being considered for a wide range of applications. In the automotive industry, they are used in vehicle crash boxes [22] and jounce bumper suspension systems [23]. In the medical field, they are utilized in stents, such as angioplasty stents [24], esophageal stents [25], bone stents [26], and annuloplasty rings [27].

Furthermore, as described by Gomes *et al.* [28], achieving the optimal performance of auxetic tubular structures is best attained through optimization. This process involves obtaining the best possible results under specific conditions by optimizing the structure layout within a defined project space, considering particular forces, boundary conditions, and constraints, where the goal is to maximize or minimize the structure's performance [29].

Considerable research has been conducted worldwide with the aim of optimizing tubular auxetic structures, with a focus on improving their performance and efficiency. Gao *et al.* [30] developed a cylindrical double-V tubular structure demonstrating auxetic behavior. The authors optimized the structure's geometry to enhance peak crushing force and specific energy absorption. Consequently, they observed a 10.3% reduction in peak crushing force and a 39.3% increase in specific energy absorption. Novak *et al.* [31] developed and optimized a dimensionally graded axisymmetric chiral auxetic structure to determine the optimal geometric configuration. This optimized structure exhibits significantly enhanced stiffness and a more consistent mechanical response when strain energy density is utilized as the optimization objective. Consequently, specific energy absorption increased by 4.25 times.

In recent work, Francisco *et al.* [32] undertook the optimization of an auxetic tube, considering a range of structural responses including mass, critical buckling load, natural frequency, Poisson's ratio, and maximum compression load. They employed the Response Surface Methodology (RSM) to develop a metamodel consisting of a set of non-linear equations and utilized the Lichtenberg algorithm proposed by Pereira *et al.* [33] to identify optimal configurations. This optimization led to improvements of up to 43% compared to the initial model. Similarly, Behinfar *et al.* [34] utilized RSM to investigate the mechanical properties of auxetic stents with a tetra-star-chiral structure. They optimized the stent's elasticity parameters using both RSM and Non-dominated Sorting Genetic Algorithm II (NSGA-II) methods.

Identifying a research gap aimed at developing an improved structure compared to classical designs, this study draws inspiration from nature and builds upon insights from previous global investigations. Nature-inspired structures have consistently yielded remarkable outcomes, with each design demonstrating unique advantages. Through meticulous examination of animals, plants, and insects, particularly focusing on their mechanical

---

properties and shapes conducive to auxetic behavior, attention was drawn to the intricate structure of dragonfly wings. With records of its existence about 300 million years ago [35], the dragonfly is known as one of the world's most skilled fliers, displaying attractive structural mechanical properties [36, 37], such as the ability to generate significant lift forces [38], excellent maneuverability [39], a range of flying styles [40], and the capacity for sideways and backward movements [41]. Consequently, analyzing the shape of the four wings of the dragonfly, it is possible to define an auxetic pattern and behavior, which inspired the proposal of a novel unit cell based on the shape of dragonfly wings.

The currently study presents an auxetic structure inspired by the dragonfly-wing shape with the goal of increasing the energy absorption compared to the conventional reentrant and conduct a comprehensive parametric analysis of a novel auxetic unit cell inspired by the intricate structures of dragonfly wings, applied within a tubular structure.

Subsequently, a study was conducted to explore variations in the design parameters of these nature-inspired auxetic unit cells with the aim of evaluating their impact on critical properties such as Poisson's ratio, mass, and strength. To achieve optimal structural performance, RSM was employed to develop a metamodel comprising nonlinear equations. Subsequently, a multi-objective optimization utilizing the NSGA-II was carried out to determine the best configurations under diverse conditions. Prototypes were subsequently manufactured using additive manufacturing techniques. To validate our findings, a combination of finite element analysis and experimental compression tests was conducted.

The present study is based on three papers. The first, presented in Chapter 3, provides a comprehensive review of auxetic tubular structures, examining over a hundred papers. The second paper, presented in Chapter 4, draws inspiration from nature, particularly the shape of dragonfly wings, to propose a novel and enhanced auxetic unit cell for application in tubular structures. This innovative design demonstrates significant advantages in mechanical properties, especially in terms of energy absorption, when compared to classical reentrant structures. Finally, the third paper, presented in Chapter 5, involves a multi-objective optimization aimed at minimizing mass, Poisson's ratio, and stress. The results emphasize the critical importance of optimization analysis in achieving more efficient structural designs.

## 2 RESEARCH OBJECTIVES

The main objective of this work is the develop, parameterize and optimize a novel auxetic model applied in a tubular structure using numerical analyzes through the finite element method, statistics and experimental with the aim of studying their behavior.

The specific objectives are:

- Synthesize the main concepts, methods, and analyses related to auxetic unit cells and their application in tubular structures.
- Develop and parameterize a novel auxetic unit cell inspired by nature.
- Apply numerical analysis, specifically the Finite Element Method (FEM), to predict the behavior of the novel unit cell when applied in a tubular structure.
- Study and application of the additive manufacturing methodologies to manufacture the structures.
- Evaluate the mechanical proprieties experimentally the compression behavior of the auxetic tubular structure and compare it with a classical tubular structure.
- Perform the optimization process using methodologies such as Response Surface Methodology and Finite Element Analysis, as well as metaheuristics.
- Validate the optimized structure through experimental compression testing.

## 3 THEORETICAL REVIEW

In an attempt to present the latest research on auxetic tubular structure in a more compact way, some topics will be described. It will present important topics concerning the negative Poisson's ratio in tubular structures: first, the auxetic design geometries and methods used to develop the tubular auxetic structure; then, the numerical analysis used to make the structural analyses; the structural optimization; and the manufacturing techniques used around the world to produce the structures. Then, the mechanical properties of Negative Poisson Ratio (NPR) tubular structures are reviewed with a focus on energy absorption, twist deformation, bending behavior, and the negative Poisson's ratio. Finally the potential applications of auxetic tubular structures are presented.

### 3.1 RESEARCH CONTRIBUTORS

Since Lakes reported the first NPR structure in 1987, called the reentrant structure, and Xu *et al.* ([42]) reported the first tubular auxetic structure in 1999, there has been a significant increase in research on auxetic tubular structures with the passing of the year, possibly due to the mechanical properties and the diverse fields to which these kinds of structures can be applied.

From the search performed using the Scopus site containing the search strings ("Auxetic" AND "Tube" AND "Structure"), was possible to analyse the research influence of auxetic tubular structure. Figure 3 (a), present the total number of papers published about the auxetic tubular structure in the last years was 68, with the number of publications increasing from 3 in 2013 to 20 in 2022, for a total of 61 papers in the period, representing a 95% increase. Using the same data source as in Figure 3 (b), we can also see the countries where researchers are studying the auxetic tubular structure, and we can see that China has the most papers published in this period, totaling 31; Australia and the United Kingdom, both with 13 papers published; and Iran, Malaysia, and the United States, all with 6 papers published. It is possible to notice that auxetic structures, particularly those discussed in this paper, have been attracting a lot of attention over the years, indicating a rapid increase in academic papers on NPR tubular structures and witnessing the topic of auxetics become more popular.

In Figure 3.1(c), some institutions of auxetic tubular structure research are presented, such as the Mechanical Engineering Institute department and the study group GEMEC, localized at the Federal University of Itajuba in Brazil. Center for Innovative Structures, College of Civil Engineering, Nanjing Tech University, Jiangsu, Nanjing, China. Center for Innovative Structures and Materials, School of Engineering, RMIT University, Melbourne, Australia. Bristol Center for Nanoscience and Quantum Informa-



tion (NSQI), University of Bristol, Bristol, United Kingdom. Department of Engineering, School of Science and Technology, Nottingham Trent University, Nottingham, UK.

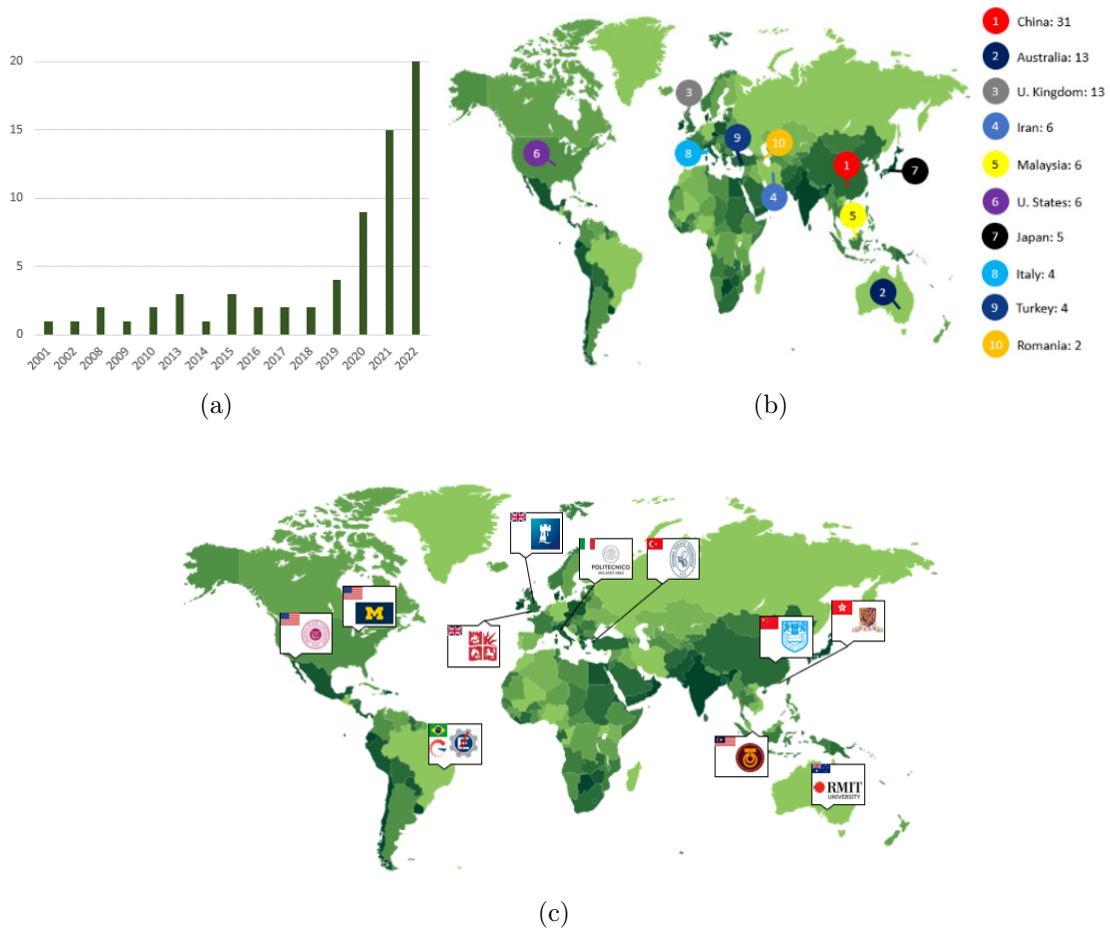


Figure 3.1 – (a) Number of publications on the topic of auxetic tubular structures per year since 2001, (b) Countries where researchers are studying the auxetic tubular structure, (c) Institutions of auxetic tubular structure research.

## 3.2 DESIGN OF NPR STRUCTURES

NPR structures can be developed and constructed with conventional materials with a positive Poisson's ratio since they adopt a design that provides an auxetic behavior. Many of these structure configurations, which are recognized in literature, have been used in several studies and articles around the world [4].

Figure 3.2 present the several structures with NPR behavior have been developed over the years using various methodologies, for example: Reentrant, Chiral, Star Shape, Rotational, Double Arrowhead.

The reentrant structure was the first model studied by Roderic Lakes [1] in 1987. They studied the mechanical properties and performed experimental tests to validate the reentrant structure. After 10 years since the development of reentrant structures, Lansen

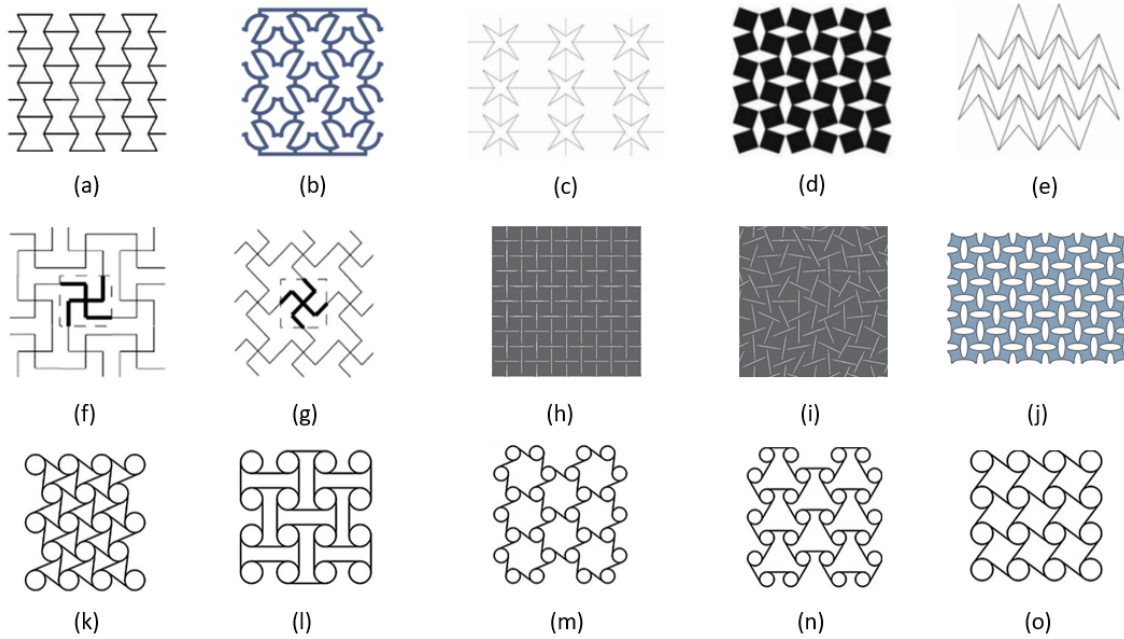


Figure 3.2 – Auxetic structures: (a) re-entrant honeycomb [43], (b) S-shaped [44], (c) Star-shaped [45], (d) rotational [46], (e) Double Arrowhead [47], (f and g) Missing Rib [48], (h and i) Perforated [49], (j) Elliptical [50], (k) Hexachiral structures [51], (l) Anti-tetrachiral structures [51], (m) Trichiral structures [51], (n) Anti-trichiral structures [51], and (o) Tetrachiral structures [51].

*et al.* [47], in 1997, started the study of a new geometry with NPR behavior: the double arrowhead structure. To certify the design, the authors optimized the design and fabricated the samples. For posterity, they performed experimental tests to verify the structure’s mechanical properties, and the results presented good linearity until the moment where buckling appeared. In the same year, 1997, Lakes and Prall [52] studied chiral geometry, where the chiral modes of the structure rotate when it receives a compressive force, causing the auxetic behavior. The authors studied the properties of a chiral honeycomb with a Poisson’s ratio of -1 and concluded that the Poisson’s ratio is maintained over a significant range of strain, in contrast to the variation with strain seen in known NPR materials. Also in 1997, P. Theocaris *et al.* [45] proposed a new structure with a star geometry exhibiting auxetic behavior. The authors showed numerically that mainly the shape of the re-entrant corner of a non-convex, star-shaped microstructure influences the apparent (phenomenological) Poisson’s ratio.

In the year 2000, Grima and Evans [46] developed a structure with a rotational design. According to the authors, the geometry modeled here is commonly found as a projection of a plane in inorganic crystalline materials involving octahedrally coordinated atoms. They also verified that the new structure proposed presented a negative Poisson’s ratio. Also in the same year, Smith *et al.* [53] developed a novel mechanism for generating auxetic behavior in reticulated foams, based upon the selective removal of ribs from a network without changes in internal angles; the authors called the structure the “missing

rib foam model”.

With the passage of time since the first models studied and due to the increasing interest in these structures, many authors have been proposing new models or models with improved designs. In 2010, Bertoldi *et al.* [54] proposed a new model of auxetic structure with a circular and elliptical hole. To validate the mechanical proprieties and the behavior of the new structure proposed, the authors performed compression tests, and they conclude that the overriding features of the system explored are the simplicity of the construction and the robustness of the behavior. In 2016, Grima *et al.* [49] proposed a novel class of perforated systems containing quasi-random cuts based on the rotating squares motif and looked at how the Poisson’s ratios and stiffness in such systems are affected by “randomness” or “disorder” in slit orientations. After 3 years, Singamneni *et al.* [44] developed a new auxetic structure with significantly reduced stress concentration effects, where the authors proposed the unit cell in an S-shaped. The authors compared the deformation response to the reentrant structure, where the responses obtained of the S-shaped auxetic structure were far superior to those of the reentrant structure, as there was no cracking and failure of the elements of the structure.

In 2020, Wang *et al.* ([8]) developed an auxetic structure inspired by a peanut-shaped hole. To verify the auxetic behavior of the structure, the authors performed numerical and experimental tensile tests, and they concluded that the auxetic behavior of the new structure design is fully controlled by the geometrical parameters, which alter the micro-structure of unit cells. Also inspired by nature’s geometries, in 2021, Zhang *et al.* [55] proposed a novel butterfly-shaped auxetic structure with a negative Poisson’s ratio and enhanced stiffness, where the structure design was based on the butterfly pattern structure and the star-shaped honeycomb structure. To validate the structure, the authors compared the new structure with the traditional re-entrant hexagonal honeycomb structure and the star-shaped honeycomb structure, where, according to the authors, the relative elastic modulus and auxetic effect of the new structure were greatly improved, and the stiffness of the novel structure was improved while maintaining a high auxetic effect. After a year, in 2022, Hamzehei *et al.* [9] inspired by the 2D image of a DNA molecule, developed multi-stiffness unit cells composed of two multi-stiffness re-entrant unit cells, so-called “soft and stiff re-entrant unit cells”. To validate the mechanical properties of the new design proposed, the authors compare the new design to the conventional auxetic models, where they performed numerical analyses evaluating the deformation patterns, and to validate the obtained results, they performed experimental tests. As a result, the multi-stiffness reentrant unit cells exhibited the highest energy absorption capacity, and the new unit cell design compared to the traditional unit cells exhibits superior energy absorption.

### 3.2.1 DESIGN OF HYBRID AUXETIC STRUCTURE

Another important structure that has been developed by researchers around the world is a combination of two or more auxetic unit cells called auxetic hybrid structures. In Figure 3.3, it is possible to see six examples of types of hybrid auxetic structures:

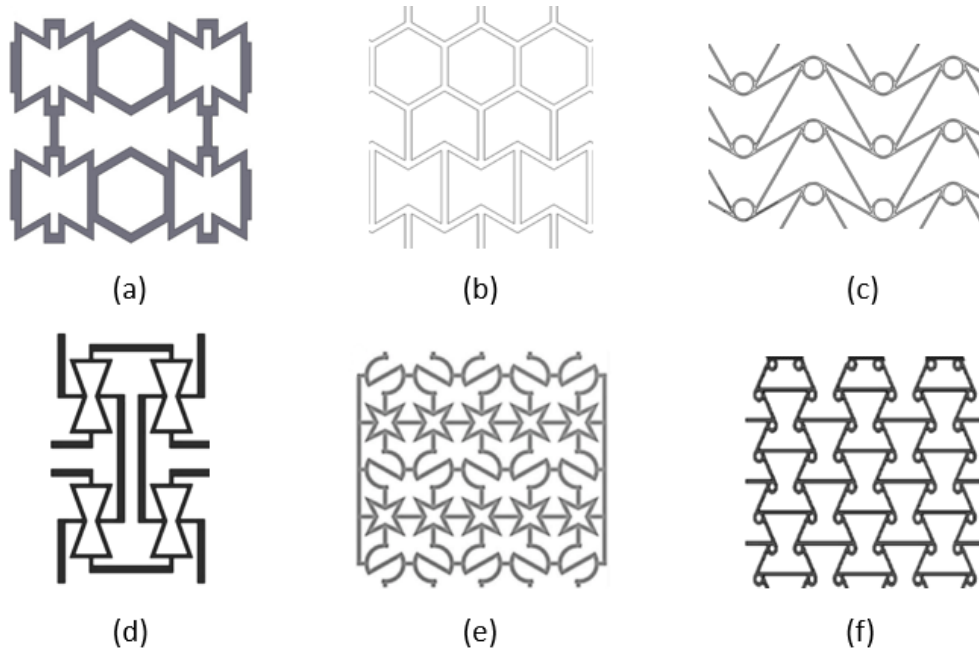


Figure 3.3 – Auxetic structures: (a) Hybrid reentrant honeycomb [56], (b) Reentrant hexagonal honeycomb [57], (c) Hybrid reentrant-chiral [58], (d) Reentrant missing rib [59], (e) S-shape with star [60], and (f) Chiral reentrant [61].

In 2017, Ingore *et al.* [56] designed and modeled an auxetic and hybrid honeycomb structure, proposing two different auxetic-strut/honeycomb hybrid cell structures. To validate the new structure, the authors conducted a numerical and experimental test comparing it to the other three structures: honeycomb, reentrant, and the new design of reentrant auxetic strut. The hybrid structures, achieved 65% high compressive strength than the re-entrant auxetic structure and 300% more than that of honeycomb structure also the energy absorbed by the auxetic-strut design is 70% more than honeycomb and 30% more than that of re-entrant auxetic models. After two years, Xu *et al.* [57] created a unit cell configuration that represents a hybrid structure made up of two different types of cells: hexagonal honeycomb and auxetic structure (reentrant hexagonal honeycomb). To validate the structure, the authors performed tests to verify the energy absorption and mechanical properties of the new structure. They compare the structure developed to a honeycomb structure; the hybrid structure demonstrated superior mechanical properties where, in the x-direction, the modulus and collapse stress were improved by more than 16%, and the specific energy absorption has also has been enhanced by >38%. In 2020, Guo *et al.* [62] designed and characterized a 3D AuxHex lattice structure, where the structure is composed of auxetic re-entrant and hexagonal components. To validate

the structure, the authors performed a compression test and compared it to a traditional reentrant auxetic lattice structure, revealing that the hybrid structure has better energy absorption performances under both quasi-static and dynamic compression. Recently in 2021, Zhang *et al.* [59] developed a new type of hybrid auxetic structure combining a re-entrant or cross-chiral core unit cell with lateral missing ribs. The authors performed a numerical and experimental test of the new re-entrant missing rib metamaterials featuring optimized geometry parameters to understand the behavior of these architectures under large deformations. According to the authors, the results from the mechanical experiments and the systematic Finite Element Methodology simulations show that the in-plane effective stiffness and Poisson's ratio of the hybrid new design can be widely enhanced and tuned by tailoring the independent geometric parameters under a large interval of strains. In the same year, Meena and Singamneni [60] proposed a new type of hybrid structure with an S-shaped unit cell and star reentrant. To validate the mechanical properties of the newly developed structure, the authors conducted a numerical and experimental test, with the authors claiming that the numerical and experimental results were sufficiently correlated, demonstrating significant increases in auxeticity as high as -3 and mechanical properties with the hybrid structures. Also in 2021, Li and Yan [58] proposed an innovative two-dimensional (2D) hybrid auxetic composed with reentrant triangular and chiral unit cell applied in the structure, where the authors investigated the band gap characteristics and longitudinal elastic wave attenuation based on theoretical lumped mass-in-mass models and the finite element method, and they conclude that the vibration attenuation of the finite-size lattice demonstrates an ultra-wide vibration attenuation frequency range in the directional band gaps.

The main idea of this paper is to discuss the NPR geometries applied to a tubular shape, so in the next section, the design of a tubular NPR structure will be discussed.

### 3.2.2 DESIGN OF TUBULAR AUXETIC STRUCTURE

Matching the NPR geometries with the tubular shape makes it possible to develop a tubular auxetic structure. To create the tubular auxetic design, many authors have used computer-aided design (CAD) tools and methodologies to develop the structure.

In Figure 3.4, show a simulation made by Lee *et al.* [63] where it is possible to see the Poisson's ratio behavior before and after the tensile load is applied to the auxetic tubular structure composed of missing rib unit cells compared to a non-auxetic tubular structure composed of a positive Poisson's ratio unit cell.

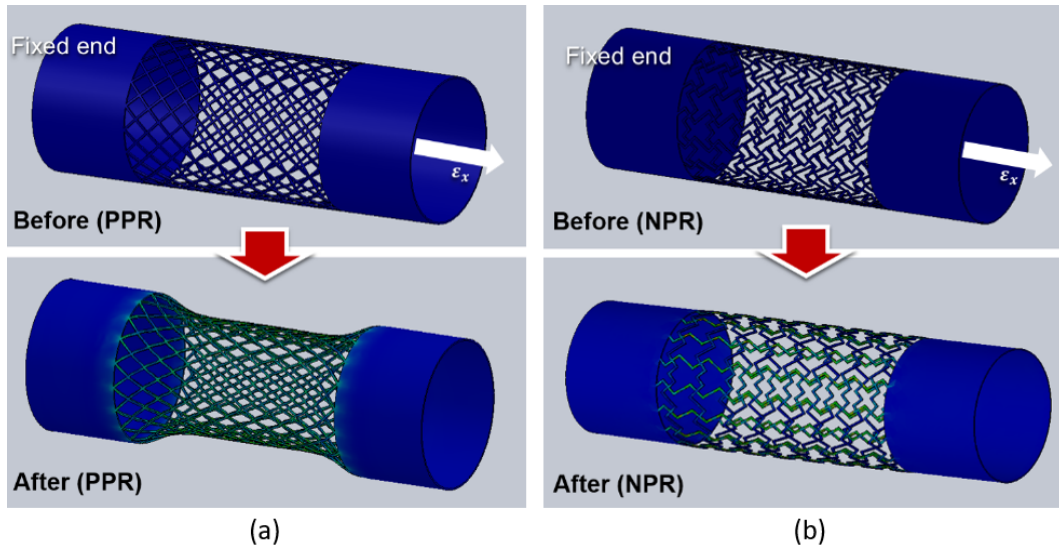


Figure 3.4 – Poisson's ratio behavior of tubular structures under tensile load: (a) non-auxetic tube; (b) auxetic tube (adapted from [63]).

The first NPR tubular structure was proposed by Xu *et al.* [42] in 1999, where the authors proposed a reentrant unit cell, also they proposed a manufacturing procedure composed of electrodeposition on a gold-coated PDMS membrane to produce an auxetic tubular structure. More recently, in 2006, Kuribayashi *et al.* developed medical stents using tubular structures with NPR behavior, where the authors used a reentrant design [24]). Also using the reentrant model, in 2008, Scarpa [13], designed and analyzed the buckling behavior of auxetic tubular structures; according to the authors, the analytical model based on the simple bending stiffness of the cell ribs provided satisfactory approximations when the  $y$  direction of the cells is aligned with the axis of the tubes.

The rotational structure is also an important type of auxetic structure. Ali *et al.* [64] developed a rotational tubular structure geometry using polymer material; the author's choice was specifically polyurethane due to its non-toxicological behavior. These structures were developed to be used as a medical stent.

Wu *et al.* [65], [66] proposed two types of chiral structures: one is anti-tetrachiral with circular and elliptical nodes, and the other is a hierarchical anti-tetrachiral with circular and elliptical nodes; both of these structures were developed for the purpose of use as medical stents. Ruan *et al.* [61], developed a tubular auxetic design that combines two different types of geometries, reentrant and antichiral, calling this type of structure an Antichiral-Reentrant Hybrid, and also created this structure with the intention of using it as a medical stent.

Based on the NPR structure's auxetic deformation characteristics and mechanics benefits, Wang *et al.* [23], [67] developed a design of a cylindrical 3D double-V tubular structure, investigated the behavior under compression forces, and made a parametric analysis. Using a similar structure in 2021, Gao *et al.* [68] designed and optimized a cylindrical NPR with a double-V geometry, and the authors compared the energy absorption

in different configurations.

In 2021, C. Zhang *et al.* [69] developed a new geometry of tubular structure based on a peanut shape; this structure presents an auxetic behavior. The authors first created a planar sheet, which was then rolled up at its mid-surface to form a tubular structure. The auxetic cylindrical structure with peanut-shaped holes on the wall exhibited great and unique deformation characteristics under uniaxial compression.

X. Zhang [6] developed an auxetic structure in the radial direction with a rotation geometry; the authors cite the possibilities to develop other geometries like reentrant, star-shaped, and chiral. To create the structure, the authors use the rotation method, dividing it into three steps: Step 1: choose the auxetic unit cells to generate the tubular structure; Step 2: determine the number of repeating cells according to the thickness and height of the tube wall; and Step 3: determine the diameter of the tubular structure and rotate the section  $360^\circ$  around the rotation axis to obtain a complete auxetic tubular structure.

W. Zhang *et al.* [70] developed a tubular structure with an asymmetrical reentrant configuration and an anti-tetrachiral tubular structure. To develop the asymmetrical geometry, the authors modified some parameters, like the horizontal length, vertical height, inclined cell angle, and wall thickness. The asymmetric geometry provides a stiffer in-plane mechanical response and more widely tunable auxetic behavior compared to a conventional anti-tetrachiral model.

Chen *et al.* [71], discussed the use of the coordinate transformation method, where the two-dimensional auxetic structure is rolled to form a perfect three-dimensional auxetic tubular structure. Where, according to the authors, the method can be used to roll plane structures into 3D tubes. In 2016, Grima *et al.* [49] reported an auxetic structure design with a perforated system, using the random cut method, and proposed two different arrangements: ordered perforated and disordered perforated. Also with the same idea of these structures in 2018, Ren *et al.* [72] developed a tubular structure using the coordinate transformation method, with the two models being ordered and disordered perforated. Han *et al.* [73] proposed the design of a thickness gradient auxetic tubular structure, the geometry of which was also developed using the coordinate transformation method.

Ling *et al.* [74] designed two types of NPR structures, reentrant and double arrow, the geometry curvature was created using the number of unit cells denoted  $N$  and the diameter of the required tube. The number of cells  $N$  used in the structure was compared to the deformation capacity properties of the structures developed by the authors.

Doudaran *et al.* [16] designed three types of auxetic tubular structures currently described in the literature: reentrant, double-arrow, and anti-tetrachiral. The authors also developed and manufactured the polyurethane foam-filled auxetic tubular structures; they compared and tested the energy absorption between the hollow and the foam-filled

structures.

Farrell *et al.* [7] proposed a new tubular auxetic structure, which the authors called “rolled chiral”. According to the authors, this structure showed a strong potential for development as a mechanical actuator due to its hollow cylindrical shape and near linear twist deformation relationships. The rolled cylindrical structure was designed using some parameters like the number of longitudinal cells, the number of lateral cells around the shell, the angle of the axial twist of the structure, the radius, and the thickness of the cylinder.

In 2022, Zolfagharian *et al.* [75] used multi-stiffness unit cells composed of two multi-stiffness re-entrant unit cells, called “soft and stiff unit cells”. With the idea to validate the mechanical properties of these new unit cells, the authors introduce the structure applied in a cylindrical tube with two main goals: vibration isolation performance in low-frequency bands prior to resonance and global buckling control of a long cylindrical tube. According to the authors, the multi-stiffness re-entrant unit cells offer global buckling control of long cylindrical tubes (with a length to diameter ratio of 3.7). The simultaneous existence of multi-stiffness re-entrant unit cells provides a feature for designers to adjust and control the deformation patterns and unit cells’ densification throughout cylindrical tubes.

Recently, in 2023, Hamzehei *et al.* [10] presented a novel class of bioinspired materials inspired by a parrot’s beak and applied to a cylindrical metamaterial, introducing contact friction, bi-stability, and interlock mechanisms at micro- and macro-scales. The authors designed different models of the parrot beak shape that led to different combinations of these mechanisms and various desired structural mechanical behaviors, such as high support stiffness, non-global buckling, zero Poisson’s ratio, and better energy-absorbing and dissipating performance. As a result, the design is presented as very robust, although the constituent materials possess an elastic-plastic property.

Han *et al.* [76], designed a novel lightweight auxetic tube based on the optimization of the original auxetic tube composed of elliptical unit cells, where the original auxetic tube and novel auxetic tube were obtained by means of the array and cylindrical coordinate transformation. To evaluate the new design proposed, the authors performed numerical and experimental quasi-static compression tests. According to the authors, the NAT presented excellent mechanical properties when compared to the OAT, such as higher specific energy absorption (SEA).

Another important point to highlight is that the auxetic tubular structures aren’t present only at the macroscopic scale. Microscopic tubular structures can also have an auxetic behavior. Goldstein *et al.* [77], [78], [79] investigated microscopic auxetic tubular structures such as carbon nanotubes and graphene. To design the tubes, the author used a method based on rolling up the rectilinearly anisotropic crystalline plates into the curvilinearly anisotropic crystalline nano and microtubes. Yao *et al.* [80] based on an energy equivalent approach, created a zigzag structure for single-walled nanotubes. The



author made a speculative investigation into the required combinations of geometrical and force constant parameters to achieve auxetic functionality, which might arise from Single-Walled Nanotubes (SWNTs) derived from alternatives to carbon, either through external temperature, pressure, stress loading through end-capping, or functionalization of the structure. Posteriorly, Scarpa *et al.* [81] studied a deformation mechanism leading to an auxetic behavior in single-wall carbon nanotubes, where according to the authors, the nanotubes can be created by ion and/or electronic irradiation.

Figure 4.1 presents an analysis of the most common types of NPR tubular structures designed and studied over the years. To carry out this analysis, references to the articles presented and discussed in this article were used, which were acquired through the Scopus website. Where 60 papers were analyzed that reported on a total of 72 tubular structures and 20 different models, filtering the articles based on how the authors approached auxetic. According to Figure 4.1, it is possible to conclude that the reentrant was the auxetic structure most developed and studied since 1999; the second most reported structure was the rotational, elliptical hole, and double-V.

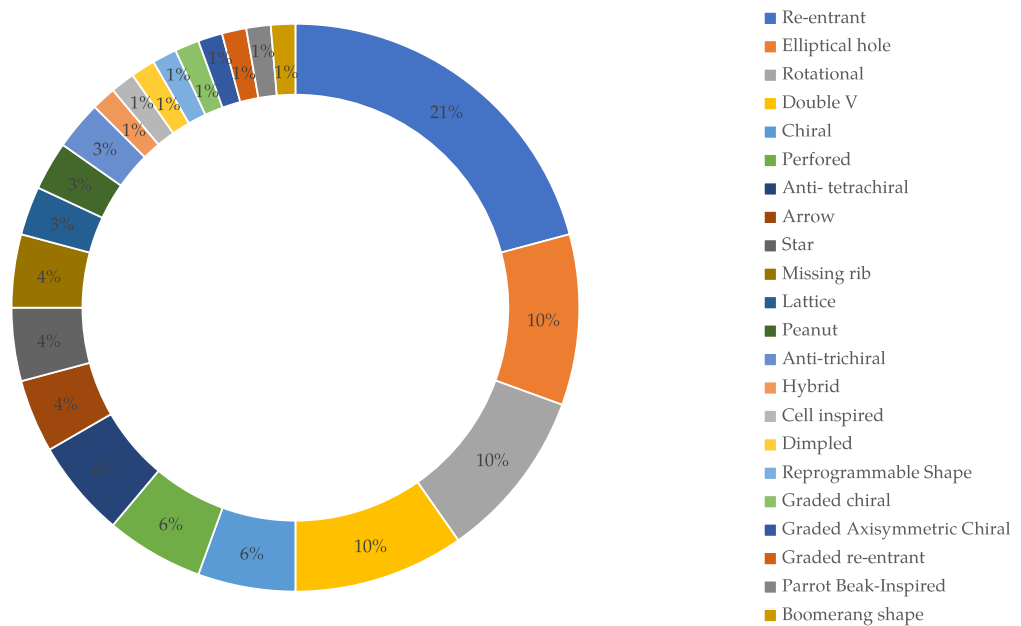
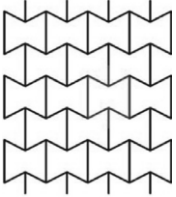
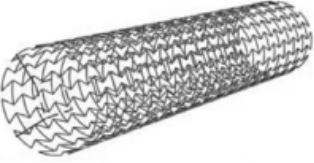
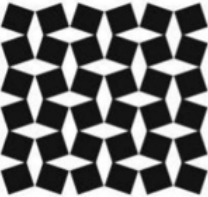
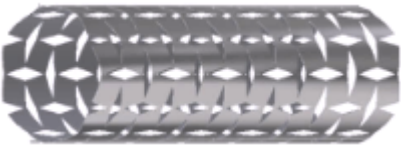
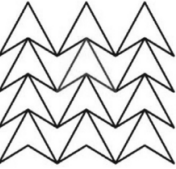
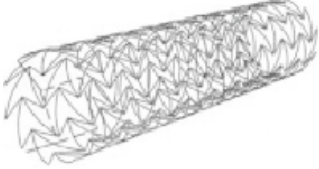
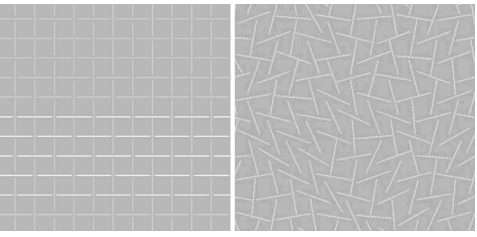
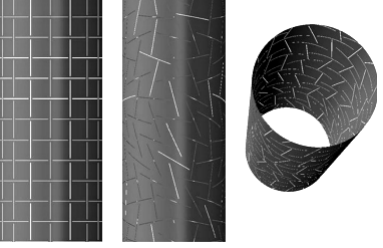
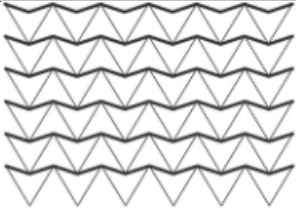
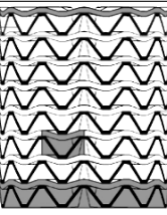
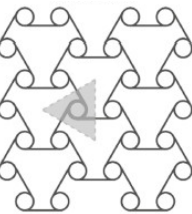


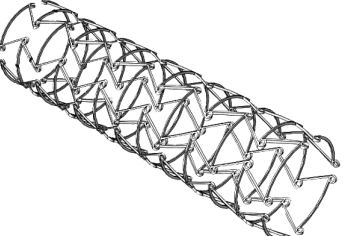


Figure 3.5 – Analyses of the percentage of the auxetic tubular structure models that are more commonly used.

Equally important, Table 3.1 presents some auxetic models applied to a tubular structure, and the main idea is to present the auxetic tubular structure.

Table 3.1 – Types of tubular auxetic structure.

<p>REENTRANT</p>  <p>[74]</p>	<p>REENTRANT TUBULAR</p>  <p>[74]</p>
<p>ROTATIONAL</p>  <p>[46]</p>	<p>ROTATIONAL TUBULAR</p>  <p>[82]</p>
<p>ARROW</p>  <p>[74]</p>	<p>ARROW TUBULAR</p>  <p>[74]</p>
<p>PERFORED</p>  <p>[72]</p>	<p>PERFORED TUBULAR</p>  <p>[72]</p>
<p>DOUBLE V</p>  <p>[67]</p>	<p>DOUBLE V TUBULAR</p>  <p>[67]</p>
<p>ANTI-CHIRAL</p>  <p>[83]</p>	<p>ANTI-CHIRAL TUBULAR</p>  <p>[84]</p>
<p>CHIRAL REENTRANT</p>  <p>[61]</p>	<p>TUBULAR CHIRAL REENTRANT</p>  <p>[61]</p>

## 3.3 NUMERICAL ANALYSIS, OPTIMIZATION AND MANUFACTURE

### 3.3.1 NUMERICAL ANALYSIS OF AUXETIC TUBULAR STRUCTURE

A numerical simulation of the structure after the model has been designed is an important or essential step in ensuring that it meets the project conditions proposed, where the methodology of finite element analyses (FEA) is widely used to predict and study the structure's behavior. When used correctly, this methodology has many advantages, including lower product and project costs, shorter project timelines, and greater flexibility. Many authors have been using the finite element method with the support of commercial software to evaluate and simulate the auxetic tubular structure's behavior and mechanical properties in many analysis simulations, such as deformation, compression, twist deformation, and energy absorption. This method has been very useful and important to analyze the auxetic tubular structure's behavior.

The methodology of finite elements is composed of the structure of discretization in finite elements connected by nodes. This methodology does not provide an exact analysis answer; rather, it provides an approximate solution by simulating the structure as a finite-length assembly of elements [85].

Figure 3.6 shows the experimental and numerical simulation made by Ren *et al.* [50] for an auxetic tubular structure with an elliptical hole model. The authors used the FEA methodology, where they adopted the Abaqus/Explicit solver in compressed simulation for considering the large deformations, to make a numerical simulation and evaluate the structure's energy absorption behavior, and later made a prototype and performed experimental tests. The authors made a comparison between the results based on numerical and experimental tests, and the error of the load–displacement curve was only about 10%.

With the idea of predicting the behavior of the structure, Figure 3.7 also presents the comparison of the numerical simulation to the experimental test made by Zhang *et al.* [69]. The authors performed a compression study to analyze the deformation of the peanut-shaped hole in the auxetic tubular structure. To perform the numerical analysis, the authors used the FEA methodology, where they adopted the ANSYS solver to evaluate the deformation under compression forces. With the objective of validating the numerical analyses, the authors made a prototype composed of VeroWhitePlus material and performed experimental tests. The study compares the outcomes of numerical and experimental experiments, and according to the authors, the results and the FEM simulation of the present cylindrical tube were in excellent agreement throughout the compressive deformation characteristics and the auxetic response.

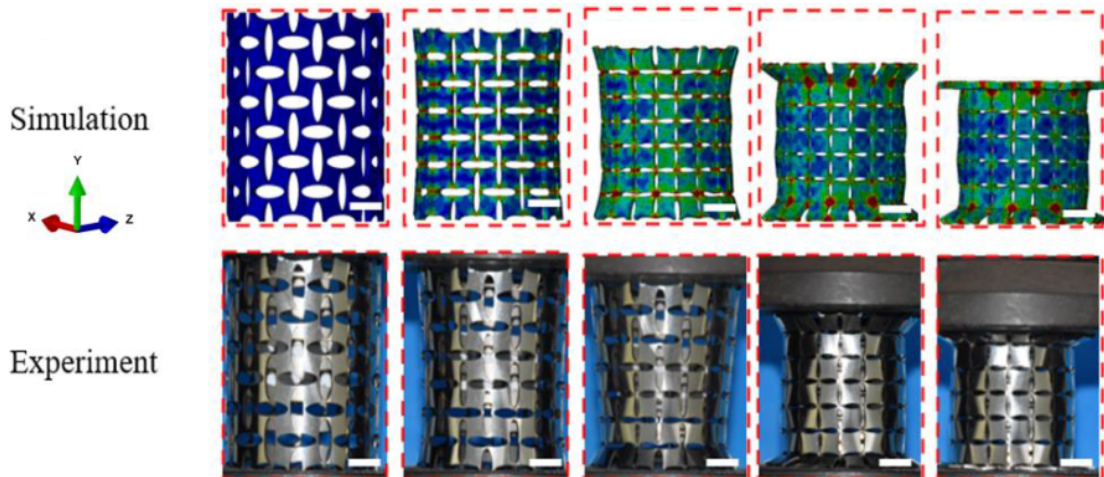


Figure 3.6 – Auxetic tubular structure energy absorption, correlation of FEA numerical simulations and experimental tests (adapted from [50]).

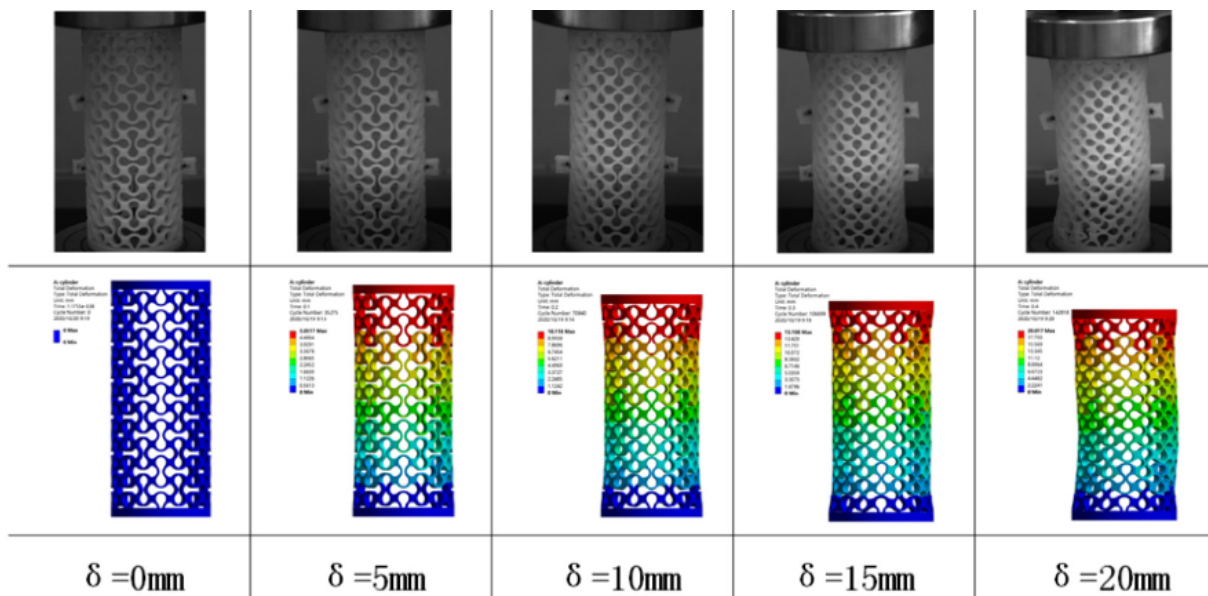


Figure 3.7 – Compression tests comparison between the FEA numerical simulations and the experimental tests in the peanut-shaped hole auxetic tubular structure (adapted from [69]).

Also, using the finite element methodology, Francisco *et al.* [32] performed a numerical analysis of a reentrant sandwich auxetic tubular structure with the objective to evaluate the compression test to analyze the failure load, the buckling test to analyze the critical buckling load, and vibration analysis to analyze the natural frequency, as seen in Figure 3.8. To perform the analysis, the authors used commercial software with the finite element method solver; also, to validate the analysis, three specimens of the sandwich composite tube were fabricated and submitted to a compression and vibration test. The results were compared with a numerical analysis to verify if the model generates substantial results, where the error of the load–displacement curve was only about 1.18% and the error of natural frequency was 5.34%.

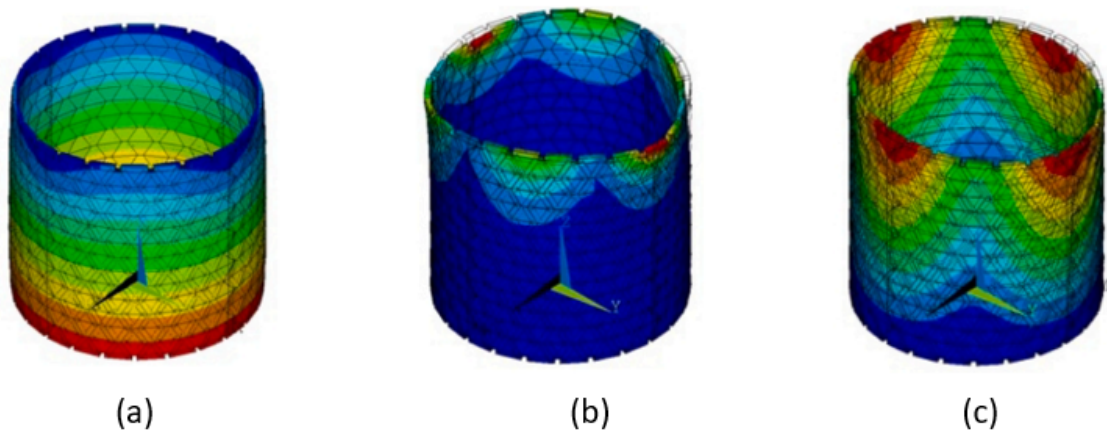


Figure 3.8 – Numerical results of (a) compression analysis, (b) buckling analysis, and (c) mode shapes (adapted from [32]).

Table 4.2 depicts some analyses performed using the FEA methodology in auxetic tubular structures, presenting the types of structures utilized, the analysis performed, and the software used by the authors.

Table 3.2 – Numerical analyses performed in tubular auxetic structures.

Authors	Design	Analysis	Software
Karnessis <i>et al.</i> [86]	Reentrant	Kinking response	MSC.Marc
Wang <i>et al.</i> [23]	Cyl. Double V	Compression	ABAQUS
Ren <i>et al.</i> [87]	Circular	Compression	ABAQUS
Yang <i>et al.</i> [17]	Dimpled	Uniaxial Compress	ABAQUS
Wu <i>et al.</i> [65]	H. anti-tetrachiral	In-plane	ABAQUS
Ruan <i>et al.</i> [61]	Antichiral-Reentrant	Compression	-
Wu <i>et al.</i> [66]	Anti-tetrachiral	In-plane	ABAQUS
Ren <i>et al.</i> [72]	Perfored	Derformation	ABAQUS
Lei <i>et al.</i> [88]	D. Reprogrammable	Derformation	ABAQUS
Geng <i>et al.</i> [89]	Chial	Mechanics Properties	ABAQUS
Farrell <i>et al.</i> [7]	Def. cell inspired	Twist-deformation	ABAQUS
Gao <i>et al.</i> [90]	Double Arrow	Impact Loading	LS-Ddyna
Jiang <i>et al.</i> [91]	Lattice	Stress-Strain	ABAQUS
Hamzehei <i>et al.</i> [84]	Anti-trichiral	Compression	ABAQUS
Nejad <i>et al.</i> [92]	Celular-Reentrant	Compression	ABAQUS
Zhang <i>et al.</i> [69]	Peanut Shape	Compression	ANSYS
Zhang <i>et al.</i> [93]	Elliptical hole	Compression	ABAQUS
Tabacu <i>et al.</i> [94]	Anti-tetra chiral	Reaction force	LD-Dyna
Zhang <i>et al.</i> [6]	Elliptical hole	Compression	ABAQUS
Gao <i>et al.</i> [68]	Cyl. Double V	Energy absorption	LS-Dyna
Jiang <i>et al.</i> [95]	Lattice	Compression	ABAQUS
Zhang <i>et al.</i> [70]	A. re-entrant	Compression	ABAQUS
Doudaran <i>et al.</i> [16]	Anti-tetrachiral	Energy absortion	ABAQUS
Doudaran <i>et al.</i> [16]	Double-V	Energy absortion	ABAQUS
Doudaran <i>et al.</i> [16]	Re-entrant	Energy absortion	ABAQUS
Han <i>et al.</i> [73]	Elliptical hole	Compression	ABAQUS
Ren <i>et al.</i> [50]	Elliptical hole	Energy absortion	ABAQUS
Novac <i>et al.</i> [31]	Axisymmetric Chiral	Compression	Ls-dyna
Solak <i>et al.</i> [96]	Peanut Shape	Mechanics Properties	Workbench
Zhang <i>et al.</i> [97]	Anti-tetra chiral	Eff. Poisson's Ratio	ABAQUS
		Eff. Elastic Modulus	

Analyzing Table 4.2, it is possible to conclude that the finite element methodology has been used by many authors all over the world, where the method's efficiency can be applied in the design of many different structures and perform many analyses such as energy absorption, kinking response, compression, deformation, and impact load.

### 3.3.2 OPTIMIZATION OF AUXETIC TUBULAR STRUCTURES

Optimization is a mathematical method that optimizes the material layout inside a determined space in the project for a specific set of forces, boundary conditions, and restrictions with the goal of maximizing the structure's performance. This method enables designers to find a suitable structural layout for the required project specifications, and it has been attracting a lot of attention around the world because, using this methodology, it

is possible to create an optimized structure with the best performance required [98], [99], [100]. Several optimization methods that are integrated with finite element analysis have been proposed, and techniques for topology optimization and multi-objective optimization have been developed, such as the Evolutionary Structural Optimization (ESO) method [101], the homogenization method [102]), and optimal algorithms such as the Lichtenberg algorithm [33].

The number of authors studying the optimization of the auxetic tubular structure is recent but has been increasing over the past few years. In 2018, Gao *et al.* [30] developed a cylindrical double-V tubular structure with auxetic behavior, where the authors made an optimization in the structure geometry, and the objective optimization was based on the specific energy absorption and the peak crushing force. After multi-objective optimization, the geometry changed the most important parameters, where the number of layers NL passed from 7 to 11, the number of cells NC passed from 7 to 13, the height of the S-beam HS passed from 25 mm to 10 mm, the thickness of the L-beam TL stayed the same, and the thickness of the S-beam TS passed from 2 mm to 1.2 mm. The comparison of the non-optimized and optimized structures is presented in Figure 3.9. The authors obtained as a result an increase in specific energy absorption of 39.3% while the peak crushing force decreased by 10.3%. It shows the effectiveness of the methodology of optimization.

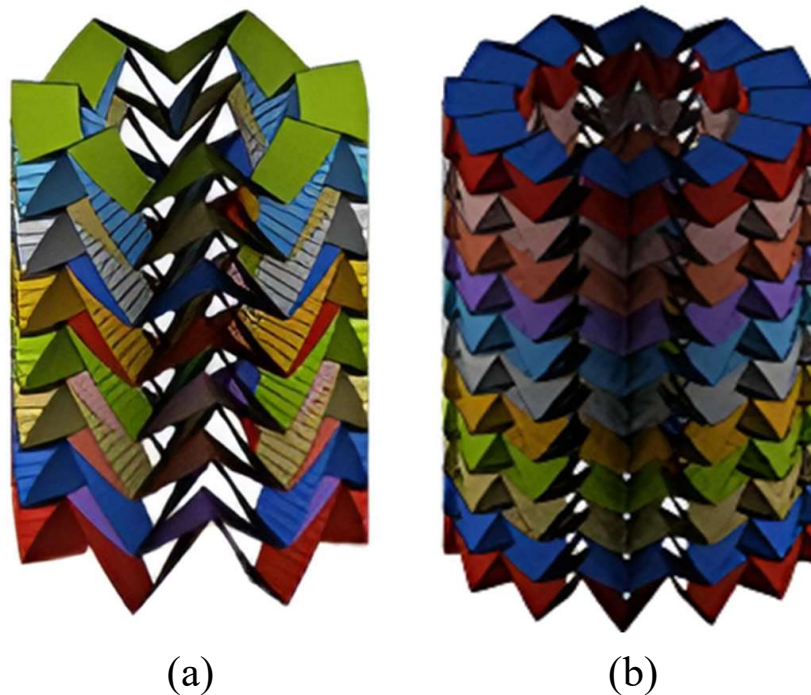


Figure 3.9 – Comparison of the auxetic tubular structure geometry: (a) non-optimized to (b) optimized (adapted from [30]).

After 3 years, in 2021, Gao *et al.*[68], also using the cylindrical double-v, made an optimization using the Multi-Objective Particle Swarm Optimization (MOPSO) algorithm; the objective of these optimizations was also the energy absorption, and after

the optimization was performed, the authors found an increase in the energy absorption of almost 2.5 times. Novak *et al.* [31] in 2022 developed a three-dimensional graded axisymmetric chiral auxetic structure and conducted structural optimization on one unit cell of the validated computational model to determine the optimal geometrical configuration. Considering the target strain energy density as the optimization objective function, the optimized axisymmetric chiral auxetic structure provides a much stiffer mass and a more normalized mechanical response, which is reflected in an increased specific energy absorption of 4.25 times.

Recently, Francisco *et al.* [32] designed and optimized a sandwich composite tube with an auxetic model composed of a reentrant unit cell using the multi-objective Lichtenberg algorithm based on metamodeling. The authors performed the multi-objective optimization of the model in two cases: modal performance and static performance. In the performance modal, the Poisson's ratio could be improved by more than 56%, as could the mass and natural frequency in relation to the initial structure, and in the static performance, the failure load, buckling load, Poisson's ratio, and mass could all be improved. Figure 3.10 presents the comparison between the initial tubular structure and the optimized structure, where the authors adopted three parameters to perform the optimization: the number of cells in horizontal directions ( $N_c$ ); the angle between the horizontal and oblique bars ( $\alpha$ ); and the height of the unit cell ( $h$ ).

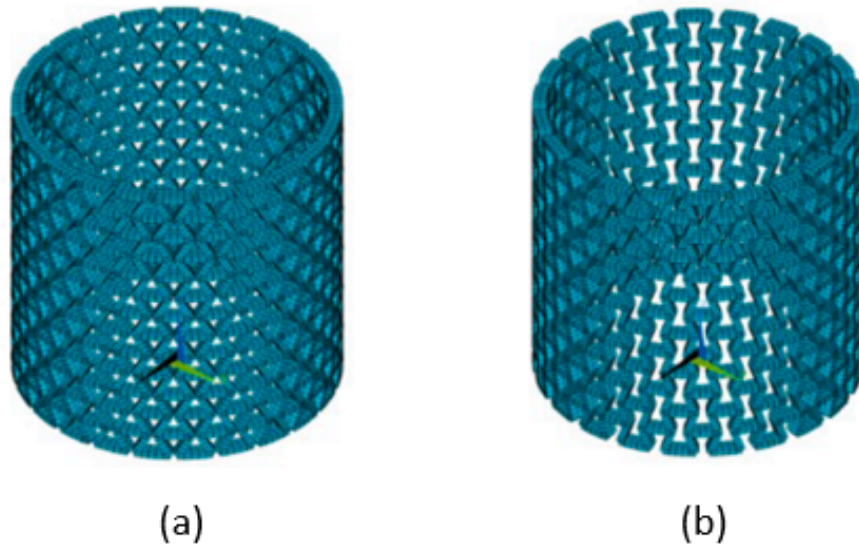


Figure 3.10 – Comparison of the auxetic tubular structure geometry: (a) non-optimized to (b) optimized (adapted from [32]).

Figure 3.11 was adapted from Gao *et al.* [30], who compared the capacity to absorb energy per displacement of an initial cylindrical double-V without optimization and an optimized cylindrical double-V. It can be noticed that the structure after performing an optimization with the objective of improving the energy absorption has a great increase in the capacity of the energy absorption when compared to the initial structure developed.



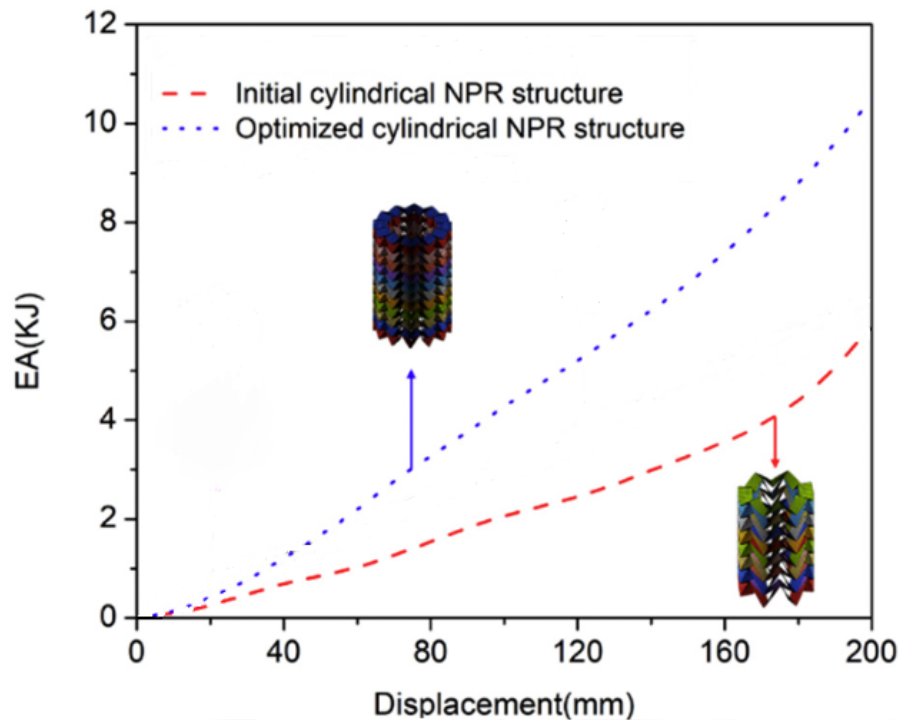


Figure 3.11 – Comparison of energy absorption (EA) per displacement between the double-V structures without optimization and the optimized structure (adapted from [30]).

### 3.3.3 AUXETIC TUBULAR STRUCTURES MANUFACTURING PROCESS

Due to the complex geometries of an auxetic tubular structure, some manufacturing methods, such as 3D printing, 4D printing, laser cutting, and textile manufacture, are required to produce these structures. This section will go over the production methods utilized by the authors over the years.

#### 3.3.3.1 ADDITIVE MANUFACTURE

##### 3.3.3.1.1 3D PRINTING:

Is a technology that is considered an additive manufacture (AM) process technique for the fabrication of a variety of components, structures, and complex geometries in 3D. Methods of additive manufacturing have been developed to meet the demand of printing complex structures at fine resolutions; the most common method of 3D printing using polymer filament is known as Fused Deposition Modeling (FDM); other methods include additive manufacturing of powders by Selective Laser Sintering (SLS), Selective Laser Melting (SLM), or liquid binding in three-dimensional printing; as well as inkjet printing, contour crafting, Stereolithography (SLA), Direct Energy Deposition (DED), and Laminated Object Manufacturing (LOM) [103].

Auxetic structures frequently have complex shapes, making them more difficult to produce. With the advancement of manufacturing methods, the use of additive manufacturing has facilitated the production of complex geometric structures such as NPR, improving their properties and multifunctional capabilities. The use of AM has provided a good balance between the cost and efficiency of the resulting structure, resulting in good material quality when compared with other manufacturing processes [104].

Additive manufacturing has been the main production process used by many authors around the world to produce NPR tubular structures. Table 3.3 presents some papers where the authors used 3D printing to fabricate the samples, presenting the design utilized and the material used to produce the structures.

Table 3.3 – Types of auxetic tubular structure manufactured by additive manufacturing.

Authors	Tubular Structure Design	Material
Ren <i>et al.</i> [87]	Circular	Brass
Yang <i>et al.</i> [17]	Dimpled	Brass
Ren <i>et al.</i> [105]	Elliptical hole	Brass
Ruan <i>et al.</i> [61]	Antichiral-Reentrant	Photopolymer resin
Gao <i>et al.</i> [30]	Cylindrical Double-V	ABS Plastic
Lee <i>et al.</i> [106]	Reentrant	Metal (SLM <sup>®</sup> 280H)
Geng <i>et al.</i> [89]	Chiral	Nylon SLS
Lei <i>et al.</i> [88]	Reprogrammable Shape	Fused filament fabrication
Farrell <i>et al.</i> [7]	Deformed cell inspired	TPU 95a
Jiang <i>et al.</i> [91]	Lattice	FLX95595-DM
Hamzehei <i>et al.</i> [84]	Triangular anti-trichiral	TPU
Zhang <i>et al.</i> [69]	Peanut-shape	VeroWhitePlus
Zhang <i>et al.</i> [93]	Elliptical hole	10 TPU
Jiang <i>et al.</i> [95]	Lattice	VeroWhitePlus
Zhang <i>et al.</i> [70]	Asymmetrical re-entrant	Nylon (PA12)
Wang <i>et al.</i> [107]	Boomerang-shaped tetrachiral	VeroWhitePlus
Brendon <i>et al.</i> [5]	Reentrant	PLA

Analyzing Table 3.3, it is possible to conclude that additive manufacturing is an excellent option to produce the auxetic tubular structure due to the possibilities to produce complex design geometries with many types of materials, such as metallics, polymers, and composites. These are the largest and most widely used manufacturing processes used by the authors to create the auxetic tubular structure.

In Figure 3.12, which was adapted from Francisco *et al.* [32], the process of additive manufacturing is presented, where the authors created an auxetic tubular structure with a reentrant design. According to the authors, the structures shown in Figure 3.12 were manufactured via 3D printing on the Ultimaker<sup>®</sup> 2+ printer using PLA filament with a diameter of 1.75 mm.

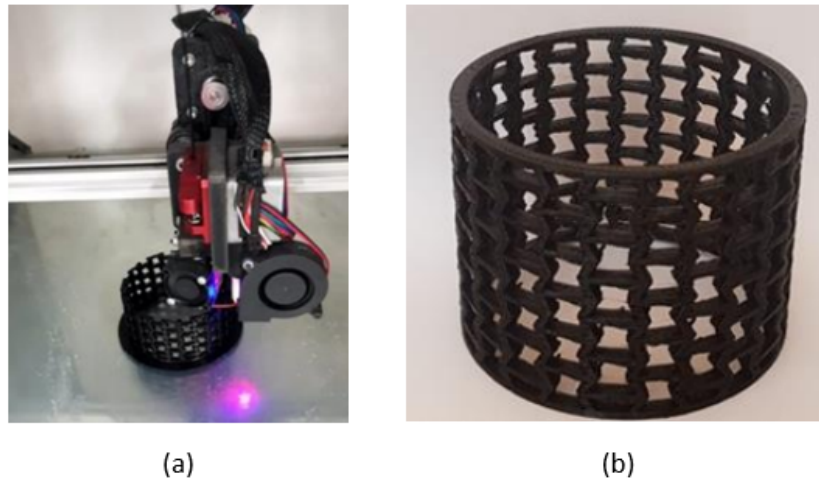


Figure 3.12 – Additive manufacturing: (a) 3D printing process; (b) auxetic tube (adapted from [32]).

#### 3.3.3.1.2 4D PRINTING:

Is a recently created technology still considered additive manufacturing. Originally, it was characterized as 4D printing, which stands for 3D printing plus time, which allows a structure to change in shape, property, or function over time. 4D printing is the next step in the progression of 3D printing in terms of shape, property, functionality, and self-repair. The facility for 3D printing, the stimulus, the stimulus-responsive material, the interaction mechanism, and mathematical modeling are the basic components of 4D printing [108].

The simplest method for 4D printing is to 3D print a single smart material, which has lately attracted a lot of interest from scientists [109]. Where it also includes the interest of researchers in applying 4D printing to auxetic tubular structures. In 2020, Xin *et al.* [110] designed and fabricated auxetic structures by 4D printing a novel programmable and tunable chiral meta-material. To produce the samples, the authors used a technology called Laser Cladding Deposition (LCD) 3D printer (ANYCUBIC Photon) to fabricate auxetic meta-materials. The application of these structures to a cylinder demonstrated the usefulness of meta-materials as a biological scaffold. According to the authors, the cylindrical shell was magnified twice because the auxetic behavior of the meta-material was not affected by the scale presented. Also, due to the tunability of mechanical properties and 4D printing technology, the scaffold can match the blood vessel in terms of mechanical properties and geometry, and the programming of the cylindrical shell presented ability in different deformation modes of compression, torsion, and stretch–torsion coupling, demonstrating the feasibility of meta-materials. Recently, Hamzehei *et al.* [10], designed the auxetic structure in a bio-inspired parrot beak shape with different combinations to evaluate the mechanisms and the various desired structural mechanical behaviors, such as high support stiffness, non-global buckling, ZPR's, and better energy-absorbing and

dissipating performance. The mechanical performance of the metamaterial structures has been 3D printed and investigated on both micro- and macroscales. To manufacture the structures the authors used in the macrostructure, they used a Multijet Fusion (MJF) 3D printer with Polyamide 12, and to print the microstructure, they used a commercial 3D printer (Photonic Professional GT+, Nanoscribe GmbH) based on two-photon lithography. The ability to recover to their original shapes is depicted in Figure 3.13, where when the authors performed a heating–cooling process, heating the macro cylindrical metamaterials and cooling them down to room temperature, they observed the samples exhibited a fully recoverable behavior, thus presenting the 4D behavior.

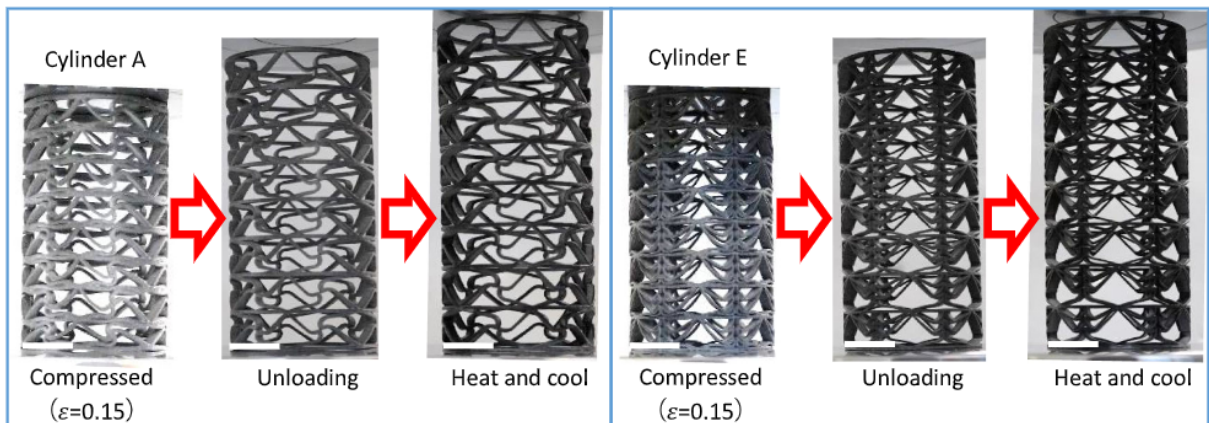


Figure 3.13 – The recovery behavior of two examples of deformed structures after compression testing, being released and processed with heating and cooling treatment (adapted from [10]).

### 3.3.3.2 LASER CUTTING

Laser cutting is a thermal process that uses energy to create parts by cutting them with a laser. This process is one of the most widely used for cutting metals such as steel, aluminum, etc. This production method has been receiving a lot of attention due mainly to the many advantages compared to the conventional machine, such as providing a high quality of cut, minimizing material loss in processing, and maintaining high precision and accuracy. The drawback of the laser cutting process is its high input [111].

Due to its capacity to produce a high quality of cut and the maintenance of precision and accuracy, laser cutting is considered a good option to produce the auxetic tubular structure. Because of the complex geometries it involves, some authors have used the laser cutting process around the world to develop and study the behavior of the auxetic tubular structure. In 2013, Bhullar *et al.* [112] developed an auxetic tubular structure applied to a medical stent with a rotating-square geometry. The authors used a Computerized Numerical Control (CNC) guided laser cutting machine to produce the prototypes, which were composed of polyurethane material. It was possible to achieve an auxetic stent with a lighter weight and improved mechanical design with a tailored negative Poisson's ratio.

After 2 years, Amin *et al.* [113] also developed an auxetic tubular structure with a rotating-square geometry applied to medical stents for the treatment of coronary heart disease. To produce the stent, the laser cutting process was used, and the materials utilized to produce the structure were 316L stainless steel, cobalt-chromium alloy, and titanium. Was it possible to develop a stent with an advantage over the commercially available stents, where the stent developed has a perfect match for the anisotropic structural properties of coronary vessels. In the same year, Munib *et al.* [26] developed an auxetic bone stent with a connected-star design composed of polyurethane material, and to manufacture the stents, the authors also used the laser cutting technique. After the fabrication, the authors performed the mechanical characterization of the auxetic bone stent in order to study its properties and deformation behavior. The tensile and expansion tests have confirmed that the rotating triangle geometry gives the stent an anisotropic mechanical behavior, and it is hypothesized that such characteristics will allow it to conform well to the intermedullary bone canal after deployment and expansion of the device. More recently, in 2022, Doudaran *et al.* [16] developed three auxetic tubular structures with different geometries: reentrant, arrowhead, and anti-tetrachiral. The structures were manufactured using the steel STL-12, and the cylindrical tube geometric specimens were composed of 0.9 mm of thickness and 24.2 mm of inner radius. To fabricate the structures, a 1000-watt rotary fiber laser cutting machine was used. After manufacturing the structures, the authors performed the energy absorption test and compared the results of the different design structures.

Figure 3.14 was adapted from Ren *et al.* [50], where the authors developed a steel auxetic tubular structure with an elliptical hole design. To manufacture the samples, the authors used the laser cutting process, which can be seen in the below image showing the production process of the structures. The process was conducted using an automatic laser cutting machine.

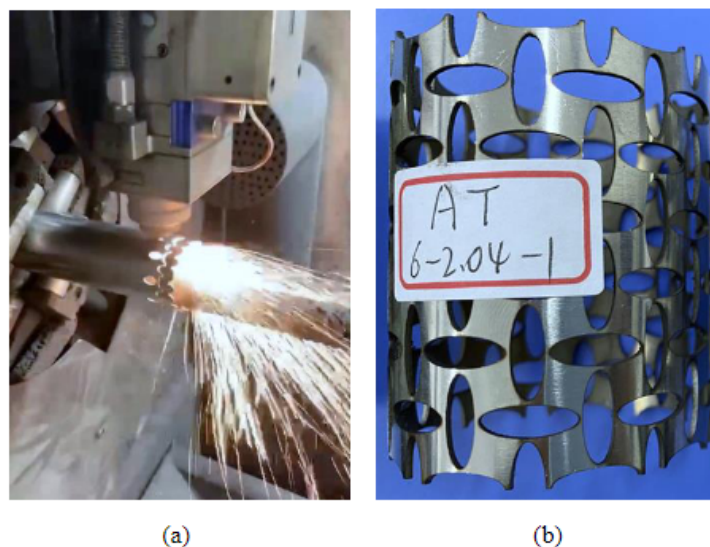


Figure 3.14 – The cutting process and the fabricated specimens of auxetic tubes: (a) laser cutting; (b) auxetic tube (adapted from [50]).

### 3.3.3.3 TEXTILE MANUFACTURE

Knitting technology is one attractive textile technology that can be used for the fabrication of auxetic tubular structures due to its high structural variety [114]. The tubular fabrics are produced in either double-faced or single-faced forms on circular machines, while on flat knitting machines, they are made in a single-faced shape with two sets of given needles. Each needle set knits in the knitting pattern in alternate cycles, and the yarn only moves from one needle bed to the next at the ends' two selvedge needles. The two single-faced fabrics created on each needle set are joined together in this action to close the tube's edges. The machine knits the tubular structure by moving loops between the front and back needle beds [115].

In 2018, Boakye *et al.* [115] developed a knitted tubular structure with an auxetic effect. The authors proposed using three types of yarn in the knitting process: nylon (430D/48F), PES (84Dtex/144F-d20L), and cotton yarn (40s/22). They used a re-entrant and arrowhead design with three different numbers of face and reverse loops ( $4 \times 4$ ,  $6 \times 6$ , and  $8 \times 8$ ). The samples were knitted on a LXC-252SC (Long Xing) V-bed flat knitting machine with gauge 14 at Jiangsu Jinlong Technology Co., Ltd., using the Longxing KnitCAD software. The authors compared the auxetic effect through the Poisson ratio between the structures developed. After 2 years, Boakye *et al.* [116] used the knitting process to develop an auxetic-knitted composite tube. The Kevlar yarn with the JH-5539 epoxy was used to fabricate the composite samples, where the authors produced three different auxetic arrow-head structures ( $4 \times 4$ ,  $6 \times 6$  and  $8 \times 8$  structure). In the first step, Kevlar yarn was used in the knitting Vacuum assisted resin transfer molding process was used to fabricate the tubular weft-knitted Kevlar tube with a JH-5539 epoxy resin as the matrix. After producing the samples, the authors performed compression tests on the structures developed to verify the capacity of energy absorption.

The other process type reported was the braided process, which is a minor but distinctive form of textile production that consists of three or more flexible materials interlaced diagonally with each other. This manufacturing process has existed for a long time and was originally produced by a manual process, but now it has evolved into an industrial manufacturing process using modern machines to produce the structures [117], [118]. If the braiding process is compared to other textile processes such as knitting, weaving, and non-woven fabric, braiding employs a method of weaving to produce a stronger product from yarn or fiber rather than weaving (in the knitting process), interlacing (in the weaving process), and interlocking (in the nonwoven process). Another important point to highlight is the excellent mechanical characteristics of braided structures, including flexural strength, impact strength, torsional integrity, and energy absorption [118], [119]. An excellent point of the braided process is its capacity for the creation of complicated and nearly net-shaped 3D structures, and it is one of the most economical methods for producing them [118]. The braiding process is appealing for creating the auxetic tubular

structure due to its ability to produce complicated, nearly net-shaped structures as well as its mechanical properties.

Jian *et al.* [120] proposed a novel type of braided tubular structure exhibiting auxetic behavior. The structure the authors developed is a helical auxetic yarn, which is made up of three components: stiff wrap yarn, low modulus elastic wrap yarns, and a low modulus elastic core. To produce the samples, the authors developed a manufacturing process, which is shown in Figure 3.15, where the process was based on tubular braiding technology to fabricate the structures. In the same year, the authors continued their work using the same production process and developed and improved standard tubular braiding technology to overcome the yarn slippage problem in the conventional helical auxetic yarn structure [121].

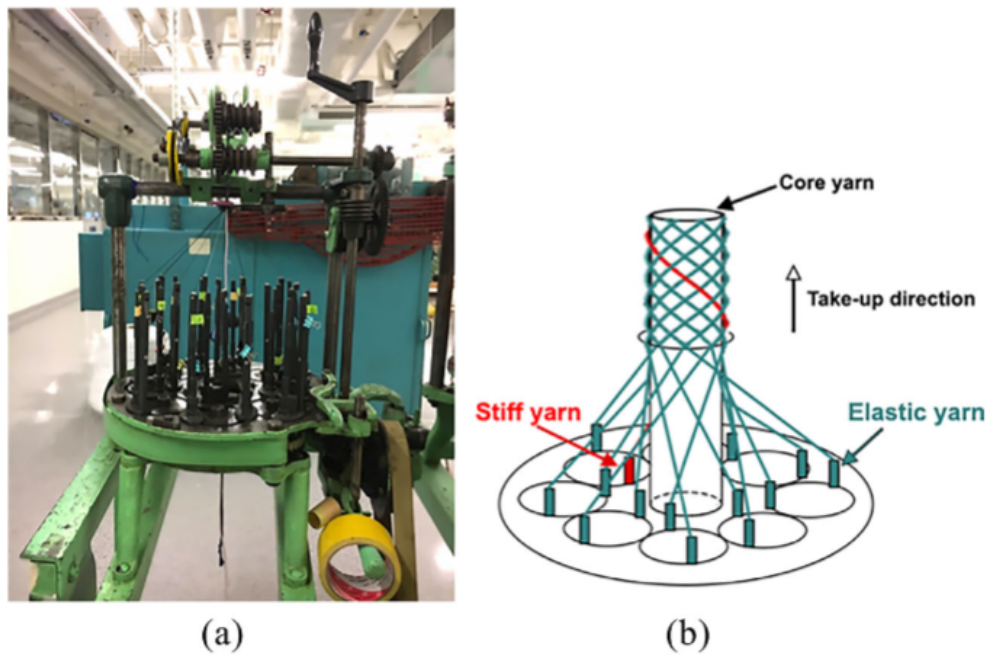


Figure 3.15 – The braided fabrication process of the auxetic tubular structures (a) The braiding machine used; (b) The schematic of the braiding process (adapted from [120]).

### 3.4 MECHANICAL PROPERTIES OF AUXETIC TUBULAR STRUCTURES

One of the most important characteristics of auxetic materials and structures is their attractive mechanical properties. This is also true of the tubular structure, which is one of the most common structures used in the engineering field due to its great mechanical properties. So matching these two types of structures, in these sections will be discussed the mechanical properties of the auxetic tubular structure, approaching the energy absorption capacity, the twist deformation, and the bending performance reported by the

authors over the years.

### 3.4.1 ENERGY ABSORPTION

When compared to other structures, the ability to absorb energy is one of the most important mechanical properties of the tubular [122] and auxetic structures, and extensive research has demonstrated that auxetic structures perform exceptionally well in terms of energy absorption [12], [123], [124], [68]. As a result of the mechanical properties of the structures, auxetic and tubular, both of which have good energy absorption properties, researchers have become increasingly interested in studying the energy absorption and impact resistance of the auxetic tubular structure.

To measure the energy absorption (EA), some authors have proposed characterizing the energy absorption capabilities of the inner tube during axial crushing or compression, performing from the methodology of finite elements or experimental tests which can be mathematically calculated using Equation 3.1 [68], [16], [50]:

$$EA = \int_0^{\delta} F(s) ds \quad [J] \quad (3.1)$$

where  $F(s)$  is the instantaneous crushing force in the impact direction, and  $\delta$  is the stroke distance. To calculate the Specific Energy Absorption (SEA), it is proposed to represent the energy absorption EA per mass ( $M$ ) (Equation 3.2).

$$SEA = \frac{EA}{M} \quad [J/g] \quad (3.2)$$

In addition, the energy absorption per loading displacement ( $d$ ) is defined in order to calculate the Main Crushing Force (MCF) of the NPR structure (Equation 3.3).

$$MCF = \frac{EA}{d} \quad [kN] \quad (3.3)$$

Table 3.4 presents the papers where the authors performed the energy absorption test. The design, material, diameter ( $D$ ), length ( $L$ ), thickness ( $t$ ), energy absorption (EA), specific energy absorption (SEA), and main crushing force (MCF) obtained on the tests were approached.



Table 3.4 – Energy absorption analyses of different types of auxetic tubular structures.

Ref.	Design	Material	Parameters	Mean Poisson	EA [J]	SEA [J/g]	MCF [kN]
[23]	Cylindrical Double V	PA and PU	L = 68.7mm	-	59.94	-	-
[17]	Dimpled	Brass	L = 100 mm D = 47.75 mm t = 0.57 mm	-	-	-	4.94
[30]	Cylindrical Double V	ABS Plastic	L = 250 mm	-0.800	-	6.060	-
[106]	Reentrant	SUS316L	L = 210 mm D = 90 mm t = 3 mm	-	-	≈ 2.40	-
[84]	Triangular Anti-trichiral	SUS316L TPU SUS316L	L = 110 mm D = 80 mm t = 1 mm	-2.190	≈ 24	-	-
[92]	Reentrant Cellular	Aluminum	D = 382 mm L/D = 1 mm L/D = 2 mm L/D = 3 mm L/D = 4 mm L/D = 5 mm	- -0.500 -0.500 -0.500 -0.500 -0.500	- 975 2334 3361 5723 7506	- 1.681 2.012 1.931 2.466 2.588	- - - - - -
[16]	Reentrant	Steel	L = 70 mm D = 48.4mm t = 0.9 mm	-0.447	175	3.380	4.34
[16]	Arrow	Steel	L = 70 mm D = 48.4mm t = 0.9 mm	-0.444	149.7	2.930	3.72
[16]	Anti-tetrachiral	Steel	L = 70 mm D = 48.4mm t = 0.9 mm	-1.603	180	3.480	4.5
[16]	Honeycomb tetrachiral	Steel	L = 70 mm D = 48.4mm t = 0.9 mm	1.106	165	3.920	4
[31]	Cellular Axisy Chiral	Steel 316L	L = 20 mm D = 20 mm t = 1 mm	-0.100	-	8.130	-
[50]	Elliptical holes AT4.5-2.72-1	Stainless Steel	L = 62.3 mm D = 51 mm t = 1 mm	-0.203	55.62	1.390	2.78
[50]	Elliptical holes AT4.5-2.72-2	Stainless Steel	L = 62.3 mm D = 51 mm t = 2 mm	- -1.030	- 306.8	- 3.92	- 15.34
[50]	Elliptical holes AT6-2.04-1	Stainless Steel	L = 62.3 mm D = 51 mm t = 1 mm	-0.895	14.91	0.38	0.75
[50]	Elliptical holes AT6-2.04-2	Stainless Steel	L = 62.3 mm D = 51 mm t = 2 mm	-1.068	88.43	1.01	4.42

Analyzing Table 3.4, it is possible to make some affirmations, where Doudaran *et al.* [16], using the same parameters to analyze and manufacture the tubes (length, diameter, and thickness), developed four tubular structures composed of different designs: reentrant, arrow, anti-tetrachiral, and honeycomb. It is possible to see the anti-tetrachiral absorb

more energy (EA) compared to the others, but when the authors measure the specific energy absorption (SEA), the honeycomb structure shows more efficiency due to the lower mass. In Figure 3.16, it is possible to see the comparison of cross-sectional shapes in folding regions under quasi-static loading performed by the authors. Also, by analyzing Table 3.4, it is possible to verify that the structures that present the highest specific energy absorption were the optimized structures, which are the cylindrical double V developed by Gao *et al.* [30] and the cellular asymmetric chiral developed by Novak *et al.* [31].

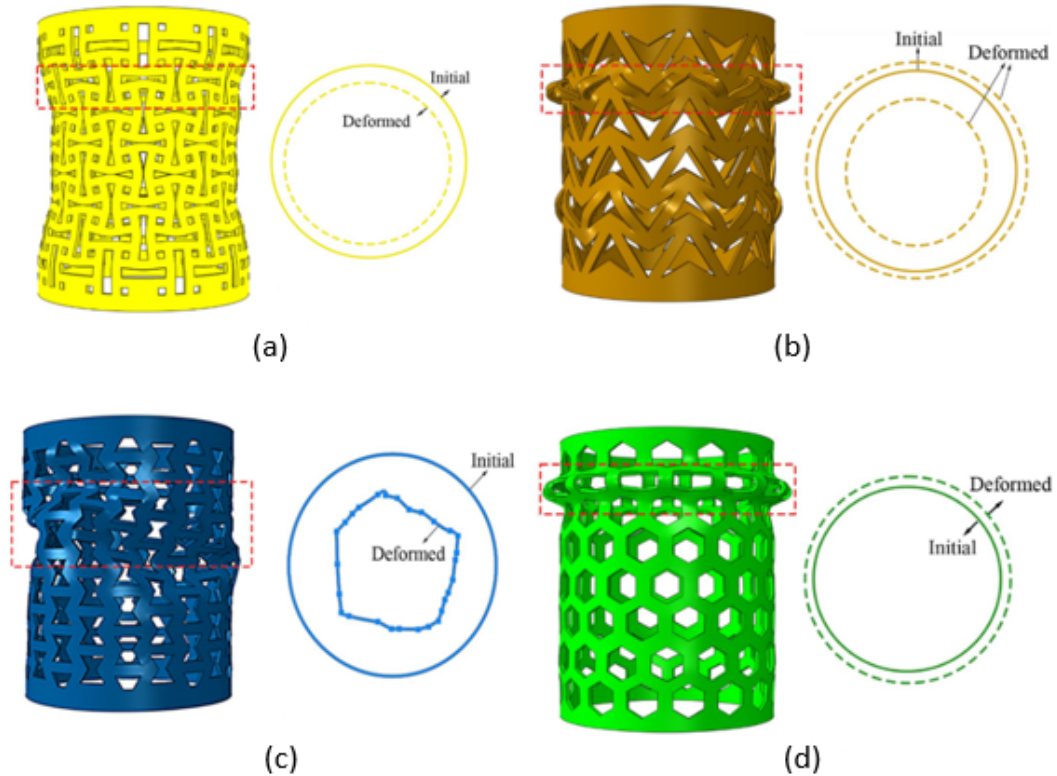


Figure 3.16 – Comparison of cross-sectional shapes in folding regions under quasi-static loading: (a) anti-tetrachiral tube; (b) arrow tube; (c) reentrant tube; and (d) honeycomb tube (adapted from [16]).

#### 3.4.1.1 THE ENERGY ABSORPTION CAPACITY OF THE AUXETIC TUBULAR STRUCTURE IN COMPARISON TO THE CONVENTIONAL TUBULAR STRUCTURE

To verify the improvement in the mechanical capacity of the auxetic tubular structure to absorb energy compared to the conventional solid tubular structure, some authors have been making this comparison through numerical analyses and experimental tests.

In Figure 3.17, it is possible to see the simulation made by Lee *et al.* [106], where the authors performed a numerical and experimental test to study the effect of auxetic structures on the crash behavior of a cylindrical tube. The authors developed three types of tubular structures: an auxetic structure with a reentrant design, a solid structure, and a honeycomb structure. The results of the test performed showed the auxetic structure

demonstrates superior performances to the other structures concerning the specific energy absorption due to the densification of the re-entrant units. Also, the auxetic tube does not only demonstrate enhanced specific energy absorption but also exhibits improved damping performance under the low impact condition as an energy absorber. Also using the same idea, in Figure 3.18 it is possible to see the simulation made by Nejad *et al.* [92], where the authors developed a 3D re-entrant cellular tubular structure and a solid tubular structure using different parameters such as length/diameter ( $L/D$ ) and analyzed the energy absorption in different structure configurations. The main idea of the authors was to make a comparison of the energy absorption properties between the auxetic tubular structure and the solid tubular structure, where comparing the results of solid tubes and cellular tubes shows that using a cellular structure can increase the crash resistance by more than 30%. The results show that the auxetic cellular tubes had better responses against compressive loading.

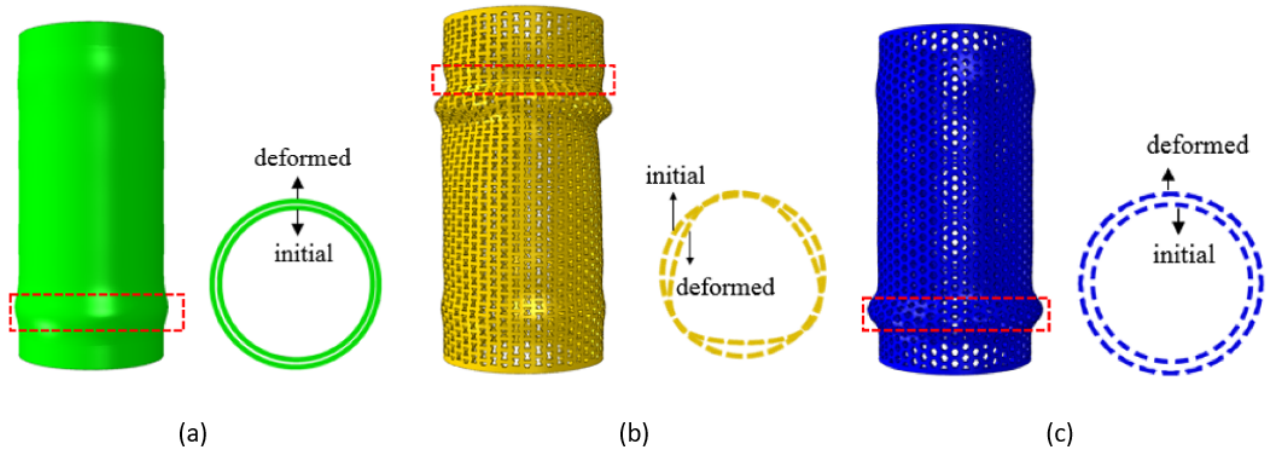


Figure 3.17 – Comparison of cross-sectional shapes in folding regions under quasi-static loading: (a) solid tube; (b) reentrant tube; and (c) honeycomb tube (adapted from [16]).

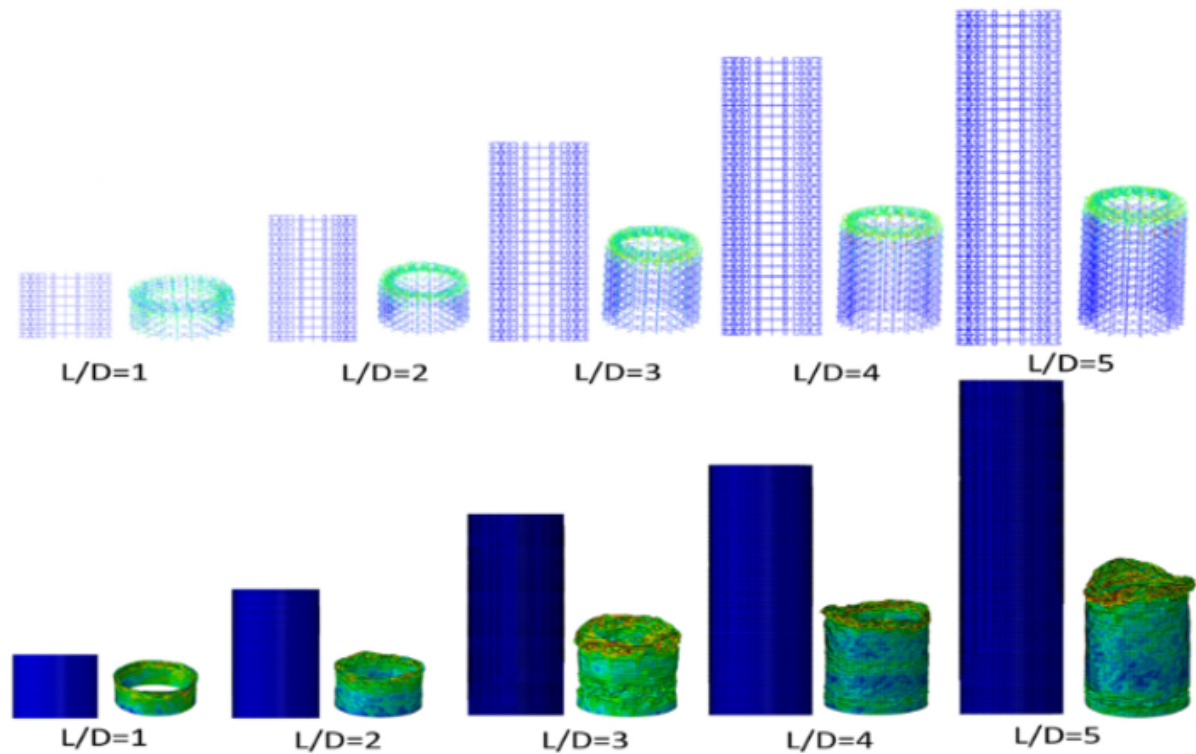


Figure 3.18 – The deformed and undeformed shape of cellular tubes compared to conventional tubes with different aspect ratios (adapted from [92]).

#### 3.4.1.2 FOAM-FILLED HOLLOW AUXETIC TUBULAR STRUCTURE

Some authors proposed developing and manufacturing a foam-filled hollow auxetic tubular structure with the goal of increasing energy absorption and specific energy absorption. Ren *et al.* [50] developed four types of auxetic structures using the elliptical hole design with different parameters (AT4.5-2.72-1, AT4.5-2.72-2, AT6-2.04-1, and AT6-2.04-2) and manufactured two samples of each, where one is a hollow structure (AT) and the other is foam-filled (FFAT) with polyurethane. The author conducted an energy absorption test on the samples and concluded that the designed foam-filled auxetic tube absorbs more specific energy than a hollow auxetic tube of the same size. From the article data, it is possible to describe the improvement of the structures as follows: AT4.5-2.72-1 to FFAT4.5-2.72-1 had a 67% SEA increase; AT4.5-2.72-2 to FFAT4.5-2.72-2 had a 5% SEA increase; AT6-2.04-1 to FFAT6-2.04-1 had a 69% SEA increase; and AT6-2.04-2 to FFAT6-2.04-2 had a 38% SEA increase.

Also, Doudaran *et al.* [16] developed four types of tubular structures: reentrant, anti-tetrachiral, arrow, and honeycomb, and manufactured two samples of each, where one is a hollow structure and the other is foam-filled with polyurethane. The schematic of the manufacturing process of a foam-filled tube can be seen in Figure 3.19. After manufacturing the samples, the authors performed the energy absorption test and compared the results, where the results show that the energy absorption in reentrant with foam and arrow with foam structures increased by 78% and 47%, respectively, compared to struc-

tures reentrant and anti-tetrachiral, while in honeycomb with foam and anti-tetrachiral with foam structures, the energy absorption was increased by 30% and 13%, respectively, compared to the empty tubes.

Recently, Ren *et al.* [125], designed and produced an aluminum foam-filled auxetic tube composed of elliptical unit cells. The authors proposed two hollow auxetic tubular structures composed of different elliptical unit cell geometric parameters (AT4.5–2.72–2 and AT5.63–2.174–2) and two different aluminum foams (A and B), which can be differentiated by the density. Combining the two hollow auxetic tubular structures with the two aluminum foams, the authors developed four aluminum foam-filled auxetic tubes with different parameters (FF-A 4.5–2.72–2, FF-A 5.63–2.174–2, FF-B 4.5–2.72–2, and FF-B 5.63–2.174–2). To validate the structure, the authors performed experimental and numerical analyses, and they presented that the  $P_{max}$ , EA, SEA, and Pm of the auxetic tubes were significantly improved by the aluminum foam filling. According to the authors, filling the auxetic tube with aluminum foam can increase the stability of the auxetic tube and improve its energy absorption capacity. Also, as the density of aluminum foam increases, the energy contribution ratio of the interaction improves.

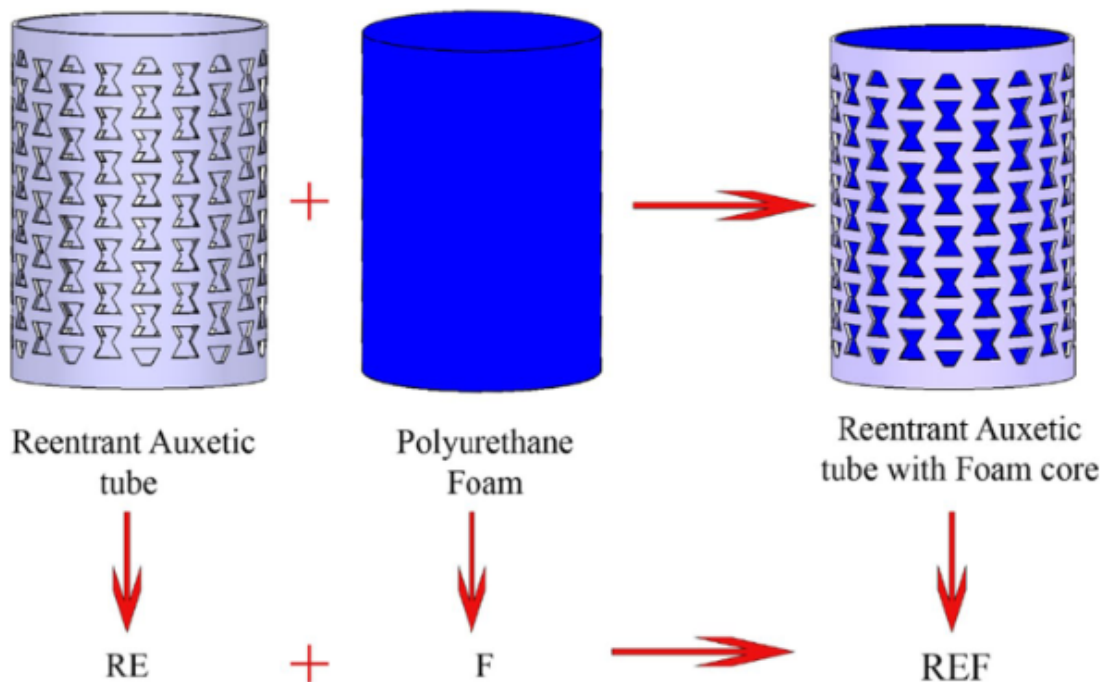


Figure 3.19 – The schematic of the manufacturing process of foam-filled tubes [16].

In Figure 3.20, is presented the comparison of numerical and experimental deformation modes under quasi-static loading performed by Doudaran *et al.* [16], where the authors compared the auxetic structures: reentrant, arrow, anti-tetra chiral, with the non-auxetic structure honeycomb. According to the authors the presence of foam filler in auxetic tubes, considering that the collapse of reentrant auxetic structure was not uniform and in arrowhead and anti-tetra chiral, folding occurred with shrinking compared to hon-

eycomb conventional structure, which caused the symmetry of deformation of reentrant with foam structure during crushing and the interaction in the arrowhead with foam, anti-tetra chiral with foam and honey comb with foam tubes with foam caused the folds of the tubes to expand outward.

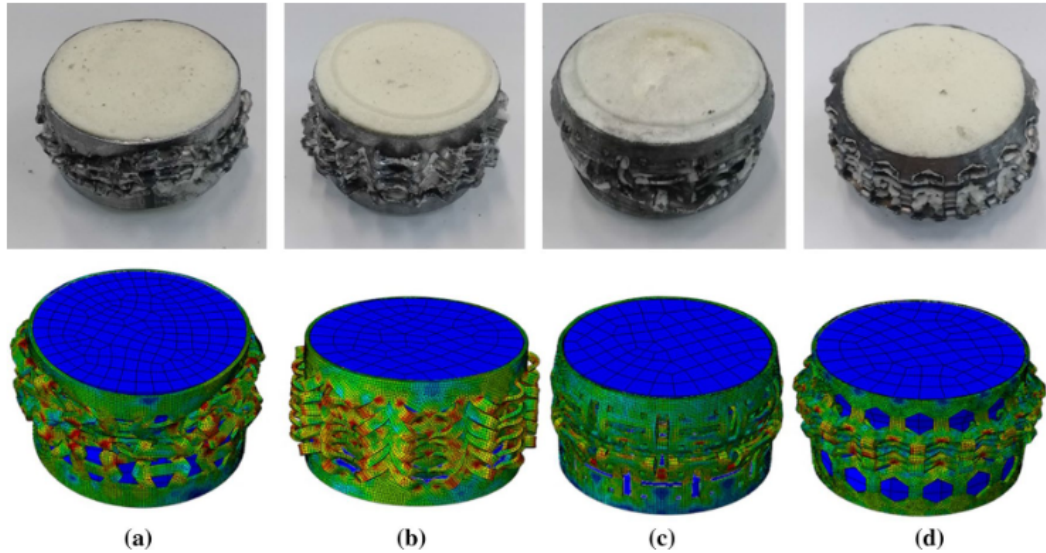


Figure 3.20 – Comparison of auxetic and non-auxetic tubes deformation modes under quasi-static loading: (a) REF, (b) ARF, (c) ACF, and (d) HOF [16].

### 3.4.2 TWIST DEFORMATION

One important mechanical property of the auxetic tubular thin-wall structure reported is the capacity for extension-torsion coupling, which is one of the most unusual deformations that occurs in such tubes and has kept the interest of researchers in studying this behavior increasing.

In 2019, Volkov *et al.* [126] performed a study of the variability of the Young's modulus, Poisson's ratios, and relative torsional stiffness. The authors concluded that such parameters as the chiral angle and the relative thickness of the tube walls can have a significant effect on the values of the Young's modulus, Poisson's ratio, and torsional stiffness. Singh *et al.* [127] presented a novel thin tube formulation to achieve coupled extension-torsion-inflation deformation in helically reinforced pressurized thin tubes. Where the authors wanted to understand the unusual extension-torsion and extension-inflation in such tubes, several analytical results were obtained in terms of the tube's fiber angle, material constants, and the imposed pressure.

Recently, in 2020, Farrel *et al.* [7] developed an auxetic cylindrical structure inspired by deformed cell ligaments with the goal of evaluating the extension-induced twist without the limitations of buckling presented in Figure 3.21(a). To make the numerical analyses, the authors used the finite element methodology shown in Figure 3.21(b), and subsequently, to validate the structure, they manufactured elastomer samples using addi-

tive manufacturing with Thermoplastic polyurethane (TPU) 95a filament and performed an experimental test shown in Figure 3.21(c). The authors concluded that the proposed structure exhibited efficient extension-induced twist up to  $60^\circ$  of axial twist for 40 mm of displacement. Further analysis determined the effect of lateral node count and tubular diameter on the twist deformation relationship.

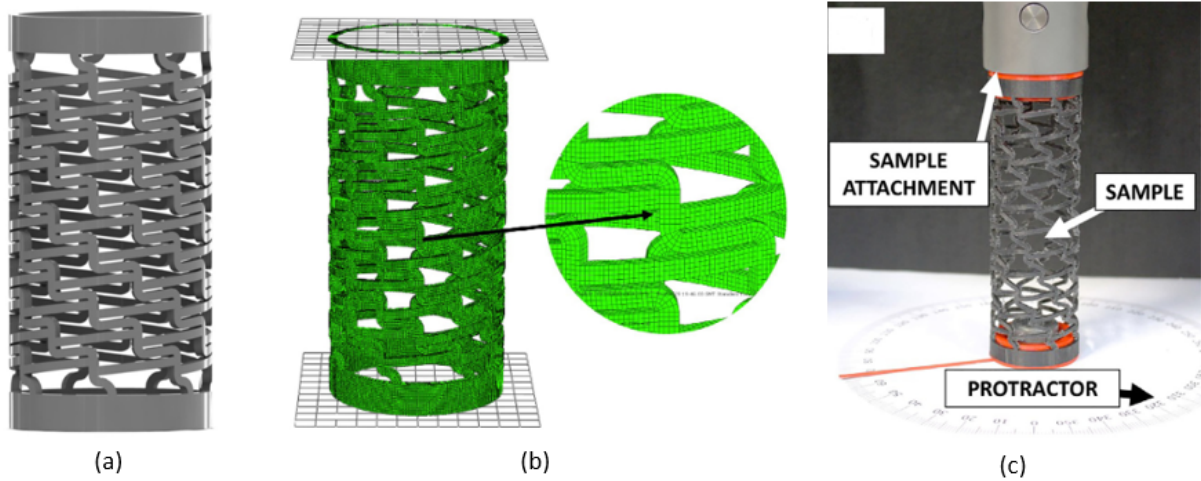


Figure 3.21 – (a) Design of an extension-induced structure, (b) Finite Element Analysis of the structure, and (c) Experimental analyses (adapted from [7]).

### 3.4.3 BENDING PERFORMANCE

One drawback of the thin-walled tubular structure is that it is prone to flexure problems [128]. Similarly, it can be stated that the auxetic tubular structure has the same drawback, but one mechanical characteristic of auxetic structures is their bending performance, where the negative Poisson's ratio determines mechanical characteristics significantly different from those of “standard” materials, such as higher flexural bending strength and enhanced resistance to buckling under pure bending, which can be defined as the ability of the material to resist bending without breaking by applying loads between the two extremities of the structure [86]. Some authors have studied this mechanical behavior. Scarpa *et al.* [13] conducted a theoretical study of the auxetic tubular structure with the reentrant design, and the authors concluded that the analytical model based on the simple bending stiffness of the cell ribs provides satisfactory approximations when the  $y$  direction of the cells is aligned with the axis of the tubes. Also, according to the FEM and continuum-based models, simulations suggest that the contributions of hinging and stretching of the ribs, as well as membranous states, contribute significantly to the overall mechanical properties of these tubular structures. In 2013, Karnesis and Burriesci [86] also performed a numerical model using the reentrant geometry, where the numerical models were used to analyze the response of these structures to local buckling under pure bending, as shown in Figure 3.22. According to the authors, the study identified

the influence of the different parameters defining the cell geometry on the phenomenon and demonstrated that the adoption of auxetic tubular structures, when appropriately designed, can contribute to considerably extending the curvature that the tube can reach before undergoing kinking. Recently, Abbaslou *et al.* [129] developed and performed a numerical and experimental test on the auxetic tubular structure, composed of the combination of three auxetic unit cells: re-entrant, trichiral, and anti-trichiral, called a re-entrant meta-trichiral auxetic. One of the authors objectives was to evaluate the bending flexibility of the vascular stent, which was investigated based on FEA and three-point bending experimental tests, which are presented in Figure 3.23. As a result, the authors found that the developed vascular stents made of Polycaprolactone (PCL) are more reliable for safely crossing among the natural curvatures of vessels.

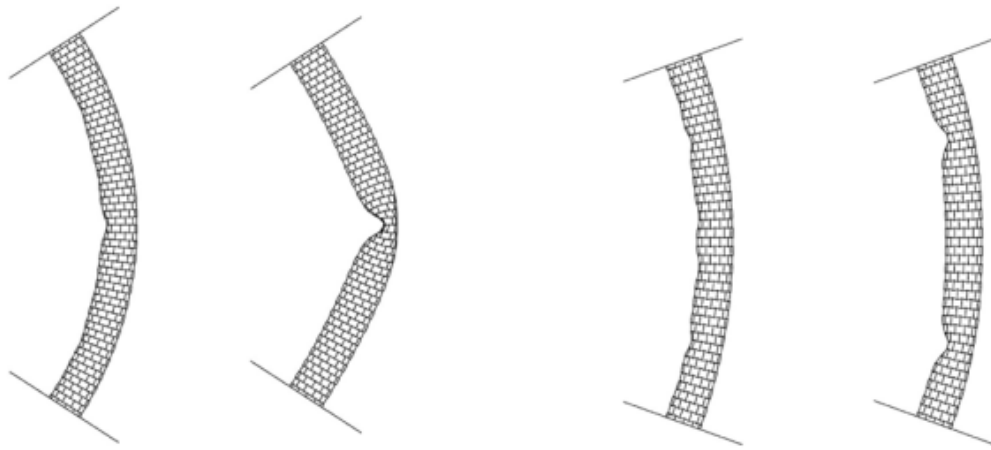


Figure 3.22 – Typical forms of buckling collapse observed in the numerical simulations: the ripple pattern formed at the compressed side and evolves into a single kink (adapted from [86]).

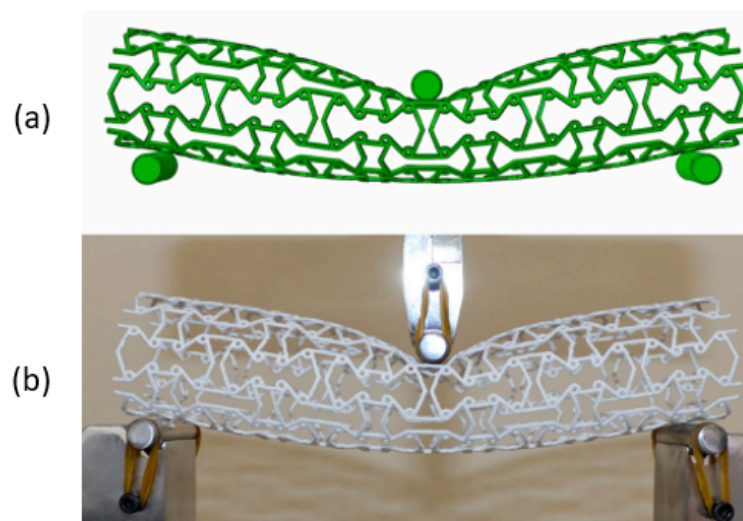


Figure 3.23 – Typical forms of buckling collapse observed in the numerical simulations: the ripple pattern forms at the compressed side and evolves into a single kink (adapted from [129]).



## 3.4.4 NEGATIVE POISSON'S RATIO AND SPECIFIC YOUNG'S MODULUS

## 3.4.4.1 NEGATIVE POISSON'S RATIO (NPR)

Since the first model proposed by Lakes in 1987 [1], many researchers around the world have been studying the behavior of the auxetic structures because they display a negative Poisson's ratio even if produced using a PPR material. Where it is possible, since the adopted configuration is suitable to generate an auxetic behavior. Therefore, starting from the diagrams of unit cells, it is possible to define important equations to calculate and evaluate the mechanical properties of the auxetic unit cell applied in a structure, such as the Young's modulus, Poisson's ratio, normal strain, and deformation [5]. In Figure 3.24, some of the most common diagrams of unit cells are presented, from which regular auxetic structures are formed by combining them. Classical designations and relationships for unit cells are shown in commonly recognized models of reentrant, arrowhead, chiral, and rotating squares. The objective of this section is to present a review of the Poisson's ratio analysis and experiments made by the authors in auxetic tubular structures.

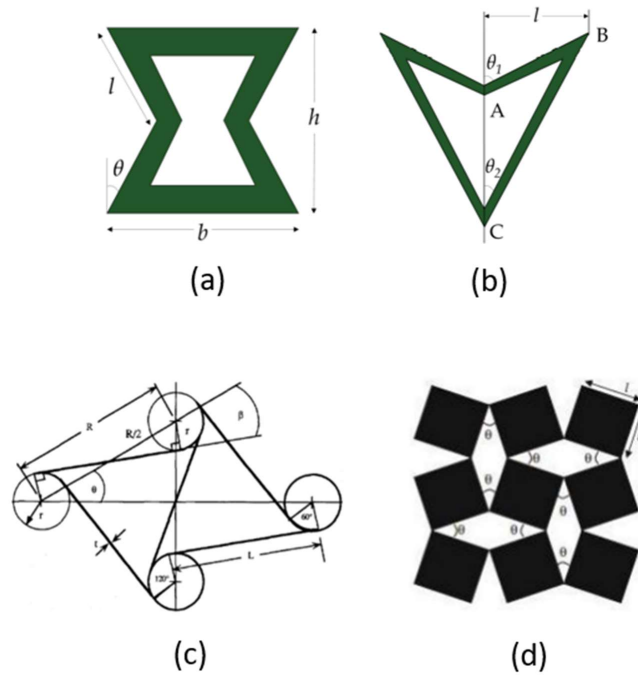


Figure 3.24 – Auxetic structures unit cell diagrams: (a) Reentrant [130], (b) Arrowhead [131], (c) Chiral [52] and (d) Rotational squares [46].

The Poisson's ratio provides the link between longitudinal and transverse strain (Equation 3.4). In conventional structures, the deformations have contrary signs, obtaining a positive Poisson's ratio. In auxetics, the strain has the same signal-generating NPR [5].

$$\nu = -\frac{\varepsilon_x}{\varepsilon_z} = -\frac{\varepsilon_y}{\varepsilon_z} \quad (3.4)$$

where ( $\nu$ ) is the Poisson's ratio, and  $\varepsilon_x$ ,  $\varepsilon_y$  and  $\varepsilon_z$  are the strains in the  $x$ ,  $y$ , and  $z$  directions, respectively. Many investigations were conducted to determine how this

attribute affected the behavior of the structures and to identify the model's weak and strong points. Also, another important point to highlight is that the Poisson's ratio of isotropic materials depends on the modulus of elasticity ( $E$ ), the shear modulus ( $G$ ), and the bulk modulus ( $K$ ), as shown in Equation 3.5 and Equation 3.6 ([5]).

$$G = \frac{E}{2(1 + \nu)} \quad (3.5)$$

$$K = \frac{E}{3(1 - 2\nu)} \quad (3.6)$$

Due to being considered one of the most important auxetic structures mechanical properties, many NPR studies have been performed in the auxetic tubular structures, evaluating the NPR in the most diverse unit cells.

Francisco *et al.* [32] analyzed the NPR behavior in the auxetic tubular structure composed by re-entrant unit cells. Where the authors conducted an exploratory analysis of the optimal points of the parameters and defined the following search intervals for the variables: The number of cells in horizontal directions varies, as do the angle ( $\alpha$ ) between the horizontal and oblique bars and the height of the unit cell. Also with the idea to evaluate the structure's Poisson's ratio Bhullar *et al.* [112] study the influence of a negative Poisson's ratio on stent applications using the rotational square design with and without role. To analyze the structures the authors fabricated and performed experimental studies of auxetic esophageal stents of rotating squares with circular holes having enhanced mechanical properties through the tailored negative Poisson's ratio. According to the authors, the stents with the geometry of rotating squares with holes and an average Poisson's ratio of -0,76 are lighter weight compared to auxetic stents without holes and a Poisson's ratio of -0,72. Still studying the Poisson's ratio behavior of auxetic stents, Wu *et al.* [66] performed a numerical analysis to evaluate the mechanical properties, including the Poisson's ratio of anti-tetrachiral auxetic stents, where the authors designed an anti-tetrachiral stent and a hierarchical anti-tetrachiral stent with circular and elliptical nodes. After the numerical analyses, the authors concluded that with the increase of struct numbers along the circumferential direction, the negative Poisson's ratio decreases; with the increase of struct numbers along the axial direction for stents with elliptical and circular nodes, the negative Poisson's ratio increases; and with the increase of the elliptical radius ratio, the negative Poisson's ratio decreases.

Ren *et al.* [72], performed a numerical investigation of tubular structures generated by the cutting method and pattern scale factor method, where the authors evaluated the Poisson's ratio of two kinds of unit cells that were then perforated sheet structures with different slits, one with ordered V-H slits and the other with disordered slits that were distributed randomly. As presented, the Poisson's ratio and diameter change rate of these two structures under different strains were calculated, respectively. As a result, the Product, Sum, Factor method had a Poisson's ratio range of -0.9 to -0.6, and the V-H

cut tubular structure dropped sharply at the beginning of the tensile deformation, and the minimal Poisson's ratio was -3.8; after that, it rose sharply to -1.2 and then increased slowly with the normalized strain.

In Figure 3.25, adapted from Jiang *et al.* [91] present the comparison between experiments to numerical simulation of an auxetic tubular structure composed of lattice unit cells in stress-strain curves from repeated mechanical tests and numerical prediction, the evolution of Poisson's ratio as a function of applied strain, and the measured and simulated deformation patterns. Where according to the authors, the experimental and numerical values presented a good agreement, especially when the strain is small. At  $\varepsilon = 0.05$ , a negative Poisson's ratio value of -0.65 is reported, which is comparable to that of most 3D auxetic lattices.

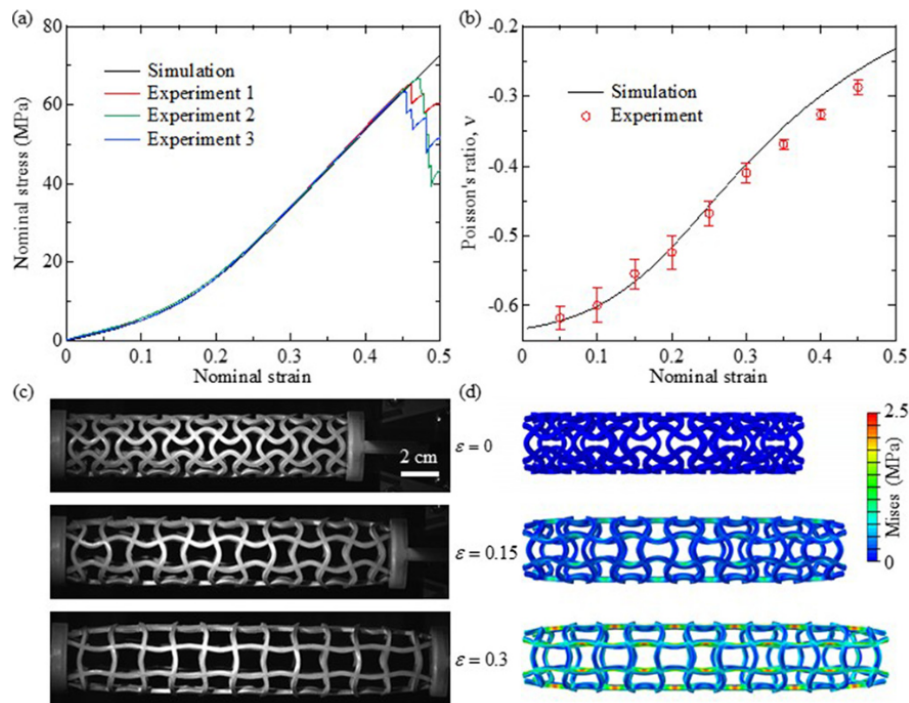


Figure 3.25 – Comparison between experiments and numerical simulation (a) Stress-strain curves from repeated mechanical tests and numerical prediction (b) Evolution of Poisson's ratio as a function of applied strain (c) and (d) Measured and simulated deformation patterns(adapted from [91]).

Finally, from the analysis of Table 3.4, which examined the mean Poisson ratio, it is evident that the auxetic tubular structure composed of triangular anti-trichiral units from the study performed by [84] exhibited the lowest Poisson ratio. Additionally, Doudaran *et al.* [16] compared three different auxetic unit cells Reentrant, Arrowhead, and Anti-tetrachiral when applied to a tubular structure of identical dimensions. Their results also indicated that the Anti-tetrachiral unit cell had the lowest Poisson ratio.

### 3.4.4.2 SPECIFIC YOUNG'S MODULUS

In this section will be discussed about the specific Young's modulus analyses performed in auxetic tubular and cylindrical auxetic structures. The specific Young modulus is an important mechanical property of the material and is used to find materials with the objective of manufacturing structures with minimum weight, as well as when the primary design limitation is deflection or physical deformation.

The Young's modulus divided by the mass density of a material is known as the specific Young's modulus. The stiffness-to-weight ratio or specific stiffness are other names for it. The Equation 3.7, where  $\rho$  and the Young modulus  $E$ , can be written as [132]:

$$\text{Specific Young's Modulus} = \frac{E}{\rho} \quad (3.7)$$

In 2018, Carneiro and Puga [133], designed and manufactured a novel generation of auxetic materials based on the 3D printing of cylindrical axisymmetric reentrant lattices. The authors evaluate the specific Young's modulus by numerical and experimental tests, comparing to other papers in the literature, and it was possible to conclude that the cylindrical structure displayed a relatively advantageous specific Young's modulus/density  $(E^*/E_0)/(\rho^*/\rho_0)$  for some specific densities ( $0.28 < \rho^*/\rho_0 < 0.35$ ). After two years, using a similar idea, Yang and Ma [134], designed and manufactured an axisymmetric auxetic. The axisymmetric auxetics are obtained by the revolution of two-dimensional curved auxetic configurations composed of two structures using reentrant unit cells and one structure using a double-U unit cell along the axis of rotation and composed of shell elements. According to the authors, after performing the numerical and mechanical experiments, it was possible to reveal that the axisymmetric deformation mechanism causes a transversely isotropic negative Poisson's ratio and enhances the specific Young's modulus compared to corresponding 2D and 3D cellular structures. Also, as a result of the comparison made by the authors, they conclude that the overall specific stiffness level is 2D structures  $<$  3D block structures  $<$  cylindrical structures for the same auxetic configuration.

Li *et al.* [135], in 2022, designed and characterized novel bi-directional auxetic cubic and cylindrical metamaterials. Where the models created by the authors were based on the two-dimensional double arrow structure being a three-dimensional cubic structure and a three-dimensional cylindrical structure. To validate the structures, the authors designed and performed numerical and experimental analyses in four samples of each structure, cubic and cylindrical, varying the parameters of the models, where the unit cell construction could be determined by geometric parameters such as the angles, height, width, and length. The cubic samples were used as parameters for the height and thickness, and for the cylindrical samples, geometric parameters of the outer diameter, the inner diameter, and the height were used. As a result according to the authors found the value of specific stiffness  $(E_y/E_s)/(\rho/\rho_s)$  of CU-4 is between CU-1 and CU-2, and the specific

stiffness of the proposed CY-4 is 52.12% higher than that of the CY-1. The results obtained by the authors present that the alterations in the unit cell parameters of the structure can modify the specific Young's modulus.

## 3.5 APPLICATIONS OF AUXETIC TUBULAR STRUCTURES

Due to the unusual behavior and excellent mechanical properties already discussed in the previous sections, the auxetic tubular structure has been attracting a lot of attention for applications in diverse fields such as automotive, medical, civil engineering, and aerospace. In this section, the possible applications reported will be discussed, focusing on the medical, nail, and automotive fields.

### 3.5.1 MEDICAL

Because the behavior of the tubular auxetic structure has a negative Poisson's ratio, which tends to increase under traction force, the tubular auxetic structure's main application in medical fields is as stents, which are small tubular structures that are inserted into the diseased region and provide mechanical support for the damaged artery or some other hollow organ to restore lumen and blood flow conditions in arteries. Its configuration as an auxetic stent to be used, for example, in the palliative treatment of esophageal cancer and for the prevention of dysphagia is the main objective [112]. Medical stents have piqued the interest of researchers, and many studies have recently been proposed by authors for designing mechanical stents used in a variety of medical procedures, such as angioplasty stents [24], [136], [66], [61], bone stents [26], annuloplasty rings [27], and oesophageal stents [25], [64] as show in Figure 3.26(a). Ali *et al.* [25], [64], [137] developed an auxetic structure with a rotational design. The structure was configured as an oesophageal stent with the potential to be used for palliative treatment of oesophageal cancer. Bhullar *et al.* [112] used a similar application to create an oesophageal stent with rotating-square geometry and holes, with the goal of creating a lighter stent. Hamzehei *et al.* [84] created anti-trichiral stents with equilateral triangular cores and conducted a parametric study to investigate the Poisson's ratio dependence on triangle edge lengths. The triangular-cored stents exhibited up to three times better energy absorption capability and twice as many lateral displacements as conventional anti-trichiral stents.

Oesophageal stents are a necessary component of palliative care for patients enduring oesophageal cancer. In Figure 3.26(a), the schematic of a tumor in the oesophagus is represented. Once positioned, the stent is expanded, bracing open the stricture of the mucosal walls of the oesophagus and thus alleviating symptoms. A diagram of a stent insert into a stenosed vessel is also shown in Figure 3.26(b).

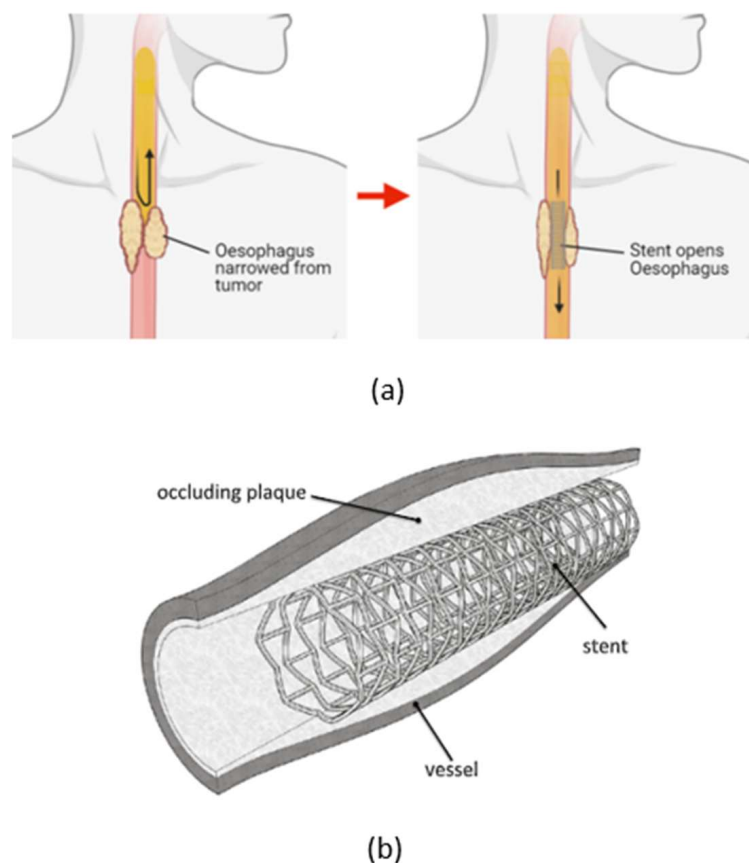


Figure 3.26 – The schematic of oesophageal stent placement (a), and the diagram of a stent inserted into a stenosed vessel (b), (adapted from [138], [86]).

### 3.5.2 NAILS

Some authors have proposed a nail composed by auxetic design in order to develop a faster nail, where the turning makes it easier to insert and harder to pull out, as represented in Figure 3.27(a). The pioneers to develop the auxetic nail were Choi and Lakes in 1991 [139]; since then, some authors have studied the behavior and applications of auxetic nails. In 2018, Ren *et al.* [105] designed, fabricated, and experimentally studied the behavior of auxetic nails, as shown in Figure 3.27(b). The authors developed and manufactured four different types of structures, including four different groups containing different parameter nails, including auxetic and non-auxetic nails, and performed the tests of push-in and pull-out. According to the authors, when compared with conventional nails, auxetic nails could be easier to push into and more difficult to pull out based on their behavior, but it was found that auxetic fasteners do not always exhibit superior push-in and pull-out performance to conventional nails. Yao *et al.* [140] created and produced auxetic bone screws utilizing the Selective Laser Melting (SLM) 3D printing technique to help improve the bone-screw fixation. An important point to highlight is that the auxetic nail discussed in this section is the result of an application of the tubular structure adapted from a nail.

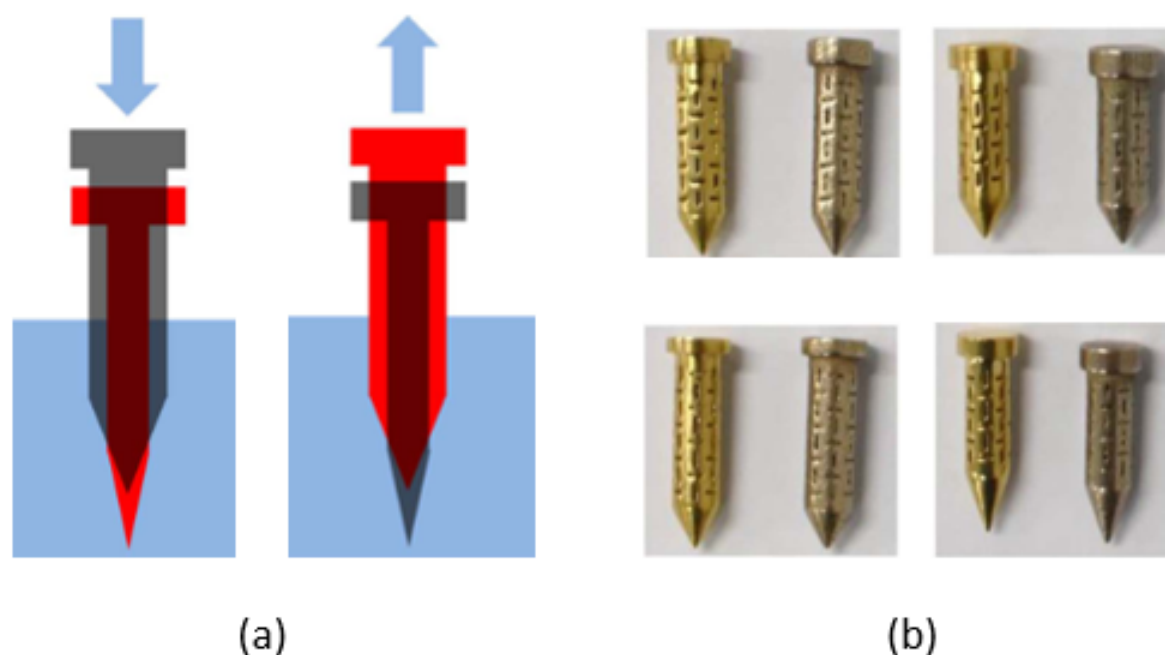


Figure 3.27 – Illustration of auxeticity for auxetic nails: (a) During push-in and pull-out, (b) 3D-printed different types of nails in four nail groups using brass and stainless steel material (adapted from [105]).

### 3.5.3 AUTOMOTIVE

As discussed in Section 3.4.1, energy absorption is one of the most important mechanical properties of the tubular auxetic structures. The use of these structures has sparked a lot of interest and attention in the automotive field in order to design lightweight and, most importantly, safe parts. One of the most common applications in vehicles is the crash box structure, which is responsible for ensuring a car's safety, as seen in Figure 3.28(a). The function of this part is to absorb energy in the event of a frontal collision during car accidents Figure 3.28(b). Zhou *et al.* [22] created an optimized novel NPR crash box; to develop it, the authors combined the NPR structure-filled core with a traditional crash box, as shown in Figure 3.28(c). The authors concluded that the NPR crash box outperformed the traditional crash box and the aluminum foam-filled crash box significantly. Tan *et al.* [141] created a similar optimized NPR crash box by combining the original box with auxetic hierarchical honeycomb. The authors performed the crashworthiness numerical test and concluded that, compared with the foam-filled crash box and the traditional crash box, the auxetic hierarchical crash box exhibits the strongest energy absorption ability. Also with the idea of improving the crash box system, Wang *et al.* [142] proposed a bumper system consisting of a NPR beam and an NPR absorber made of a large number of inner hexagonal cellular structures arranged in a periodic pattern, as shown in Figure 3.28(a). Wang *et al.* [143] studied and developed an auxetic structure with a star-shaped tube-beam design to protect the occupants in the case of a lateral

crash in the front door of the vehicle shown in Figure 3.28(d). The authors conducted numerical crash simulation and concluded that, when compared to the conventional rigid beam, the novel star-shaped NPR beam application improves occupant safety and structural crashworthiness. Wang *et al.* [23] utilized NPR material to design jounce bumpers; the authors made a comparison with the traditional jounce bumpers, which improved the noise, vibration, and harshness performance of the vehicle.

Because of the great and promising application of the energy absorber, as reported in this section, NPR thin-walled crash tubes have received a lot of attention from researchers in the automotive field and show, due to their mechanical properties, an efficient structure, making them indispensable to saving lives during automotive accidents.

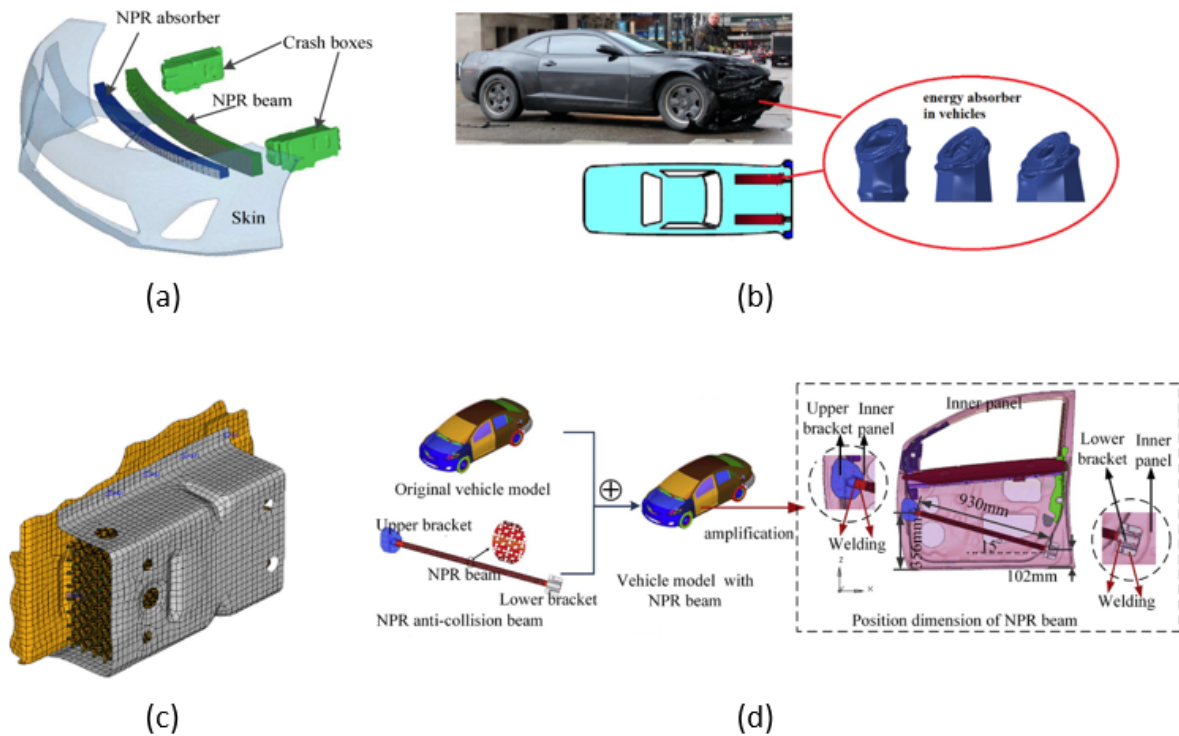


Figure 3.28 – Conceptual automotive applications of auxetic tubular structure: (a) NPR bumper system (adapted from [142]), (b) energy absorbers used in vehicle safety (adapted from [144]), (c) FEM model of the FEM crash box (adapted from [22]), and (d) Implementation of a star-shaped tube-beam structure into the front door (adapted from [143]).



# 4 A NOVEL DRAGONFLY WING SHAPE AUXETIC TUBULAR STRUCTURE WITH NEGATIVE POISSON'S RATIO

## 4.1 CHAPTER INTRODUCTION

Due to the advance of technologies, new structures are being developed that could meet the high engineering project specifications with a focus on energy absorption, where they have a vast field of application such as aerospace, aeronautical, and automotive.

A possible solution is the use of materials and structures composed of Negative Poisson Ratio (NPR), behavior which have been increasing the attention due their excellent mechanical proprieties highlighting the ability to absorb energy. It can be possible due the unusual behavior, where the materials and structures which present a NPR, under compression, they contract transversely and, under traction, they expand transversely, whatever this behavior of the material is controlled by the fundamental mechanical properties of the material, the Poisson's ratio ( $\nu$ ) [145]. The first foam with a NPR behavior was reported in 1987 by Lakes [1], and posterity in 1991 Evans *et al.* [146] called this structure as auxetic (from the Greek *auxetos*) which means tend to increase.

The main reason these structures provide NPR behavior is due to the complex geometry configuration of the unit cell designs used in the structure. These structures have been proposed and developed by authors around the world since the first structure reentrant[147]; after this, many other structures were proposed, such as rotational [46], chiral [51], anti-chiral [51], double-arrow [47], perforated models [49], S-shape [44], and missing-rib [53]. These models have advantages and disadvantages, and the choice of geometry and material will depend on the application of the structure and the tools available to manufacture it [4, 5].

When the auxetic structures compared to the conventional material and structures it exhibit attractive mechanical properties, such as excellent energy absorption capabilities [50, 12, 92], bending performance [129], shear modulus and identification resistance [145], twist deformation [7], and better fracture toughness [14]. Therefore, due to the auxetic structures being composed of complex geometries, the most common manufacturing process is generally not possible to be used where it is necessary to use advanced manufacturing procedures such as 3D printing, which has the possibility to manufacture complex geometry. Where it is possible to design and manufacture auxetic structures using conventional materials composed of positive Poisson ratio materials [28].

Nature is a source of inspiration for many projects developed in the course of his-

tory, and in the case of auxetic structures, it isn't different, where nature has been a fundamental inspiration for the authors to develop new unit cells that present the NPR behavior with goals to improve the mechanical proprieties of the structure and expand the applications. Wang *et al.* [8], developed an auxetic structure inspired by the peanut shape, and the authors could conclude that the auxetic behavior of the structure is fully controlled by the geometrical parameters. Also inspired by nature's geometries, Zhang *et al.* [6] developed a novel butterfly-shaped auxetic structure composed by a negative Poisson's ratio and enhanced stiffness. The structure was designed based on the butterfly wings, and the star-shaped honeycomb structure formed a hybrid auxetic structure, according to the authors, relative elastic modulus and auxetic effect of the butterfly-shaped were greatly improved, and the stiffness of the novel structure was improved while maintaining a high auxetic effect. Farrel *et al.* [7] developed an auxetic cylindrical structure inspired by deformed cell ligaments with the goal of evaluating the extension-induced twist without the limitations of buckling. Tung *et al.* [148] inspired by natural Bouligand-type energy absorbers, developed and investigated a series of novel helically oriented tubular structures. Hamzehei *et al.* [9] inspired by the 2D image of a DNA molecule introducing a 2D Zero Poisson Ratio bio-inspired metamaterial, the authors developed multi-stiffness unit cells composed of two multi-stiffness re-entrant unit cells, so-called soft and stiff re-entrant unit cells, according to the authors, the ZPR comprised multi-stiffness unit cells and presented high energy absorption performance. Also, recently Hamzehei *et al.* [10] presented a novel class of bio inspired materials inspired by a parrot's beak and applied to a cylindrical metamaterial, introducing contact friction, bi-stability, and interlock mechanisms at micro- and macro-scales. As a result, the design is presented as very robust, although the constituent materials possess an elastic-plastic property.

Consequently, based on the outcomes of previous studies performed around the world, each structure whose design drew inspiration from nature shapes achieved outstanding results. By exploring the shapes and mechanical properties of animals, plants, and insects that exhibit auxetic behavior, the shape of dragonfly wings was observed as a significant source of inspiration. With reports of its existence in prehistory about 300 million years ago [35], the dragonfly is known as one of the world's most skilled fliers, and many works of literature present attractive structural mechanical properties [36, 37], such as notable features of their flapping flight, including the ability to generate significant lift forces [38], excellent maneuverability [39], a range of flying styles [40], and the capacity for sideways and backward motions [41]. Therefore, when analyzing the format of the four wings composed in the insect dragonfly, as presented in Figure 4.1 it is possible to define an auxetic standardization and behavior, which was also a source of inspiration to propose a novel unit cell composed of the dragonfly wings shape.

The present work presents an auxetic structure inspired by the dragon-fly wings shape with the goal of increasing the energy absorption compared to the conventional

reentrant, based on the methodology step by step proposed by Gomes *et al.* [28]. From the wings shape of the dragonfly, with the purpose of reducing the stress concentration, the auxetic unit cell was designed, reducing all possible points that could generate a stress concentration during the compression analysis with the goal of resisting more force and displacement, which consequently increased the energy absorption properties.

To validate the novel auxetic tubular structure, the unit cell was applied in a tubular structure, performing a comparison with a classical reentrant (RE) structure based on a previous study proposed by Francisco *et al.* [32]. The tubular structure followed two different parameters to compare the mechanical proprieties of the dragonfly-wing shape to the reentrant: the first was the number of unit cells, and the second was the weight of the structures. To perform the analysis, a compression experimental test was performed, and to validate the analysis, a numerical analysis using Finite Element Analysis (FEA), which made it possible to see a greater agreement between the two, indicating the analysis's efficiency. The samples were manufactured using a 3D printer with Polylactic Acid (PLA) filament material, and comprehensive testing was conducted using a universal testing machine.

The results provide valuable insights into the force-displacement relationship, energy absorption, specific energy absorption, main crushing force, and Poisson's ration, where the Dragon-fly Wings shape presented greater results by being able to absorb more energy when compared to the Reentrant auxetic tubular structure.

## 4.2 DRAGONFLY-WING-SHAPED MODEL (DFW)

The conceptualization of the unit cell configuration finds its fundamental inspiration rooted in the evolved morphology of the dragonfly's wings shape and an improvement of the classical reentrant unit cell, a testament to nature's ingenuity, vividly depicted in Figure 4.1. In the quest for achieving optimal design efficiency, the bionic approach has been judiciously adopted, wherein the structural blueprint of the dragonfly wings has been ingeniously emulated using a circular format. The underlying rationale behind this innovative design is to proactively address the issue of stress concentration, an inherent vulnerability in traditional structures, by artfully enhancing the deformability of the configuration. By skillfully augmenting the capacity for deformation, the engineered structure stands empowered to exhibit superior energy absorption capabilities, thus fortifying its resilience and performance under varying loads respectively.

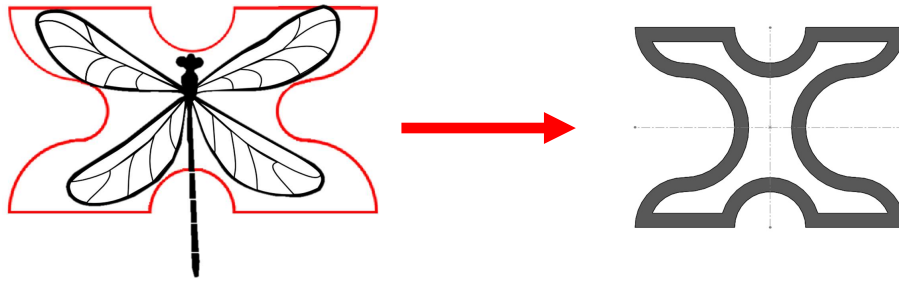


Figure 4.1 – Dragonfly-wing-shape pattern [149].

Where the shape of the dragonfly wings were the source of inspiration as a basis for developing a novel unit cell which was subsequently validated by applying in a tubular structure. The detailed parametrization of this unit cell is illustrated in Figure 4.2. The unit cell exhibits a symmetrical form, allowing for a focused study on one-quarter of the cell and its corresponding geometric parameters.

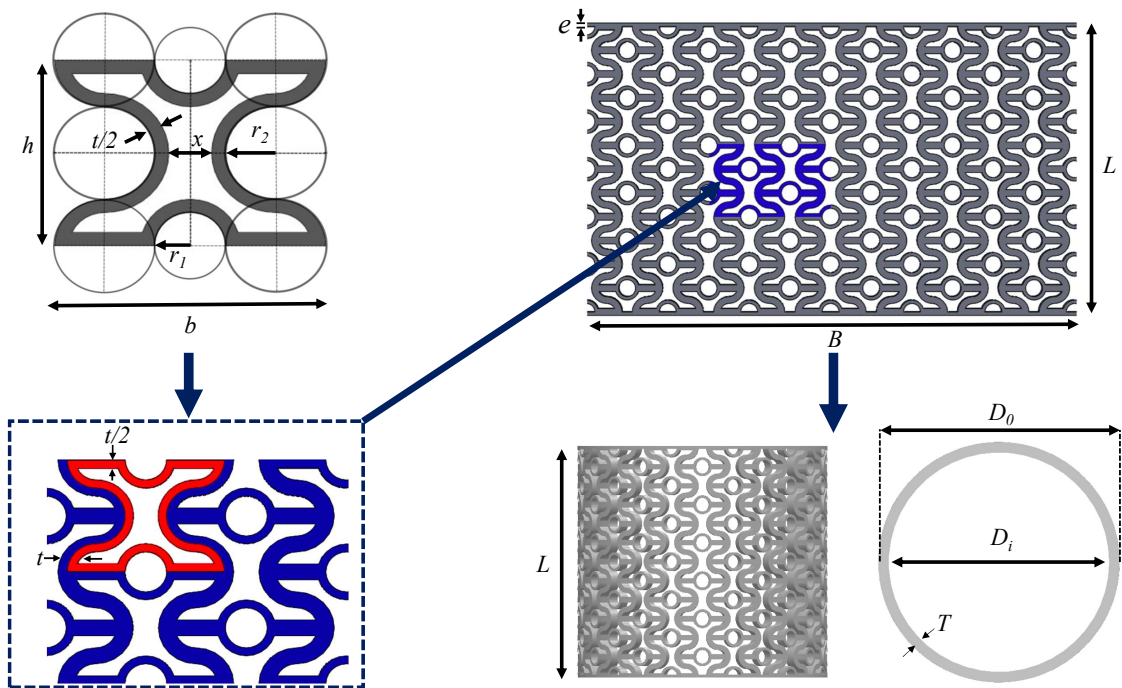


Figure 4.2 – Flowchart of dragonfly-wing-shape unit cell geometric parametrization.

With the unit cell configuration presented in Figure 4.2 it is possible to determine the geometric parameters structure consisting of two radiuses with lengths of  $r_1$ ,  $r_2$ , and the thickness represented by  $t$ . The  $h$  is represented by the Equation 4.1, and the  $b$  is represented by the Equation 4.2:

$$h = 4r_2 \quad [mm] \quad (4.1)$$

$$b = 2(2r_2 + r_1) \quad [mm] \quad (4.2)$$

From the sizes of  $r_1$ ,  $r_2$ , and  $t$ , it is also possible to determine the unit cell center distance represented by  $x$  in Equation 4.4:

$$x = 2r_1 - t \quad [mm] \quad (4.3)$$

Based in a 2D model is conceivable define important parameters such the length of the structure and the Perimeter, in the following Equations 4.4 and 4.5 respectively represented by  $L$  and  $B$ .

$$L = N_v \times h + 2e \quad [mm] \quad (4.4)$$

$$B = \frac{N_h}{2} \times (x + b + t) \quad [mm] \quad (4.5)$$

where  $N_h$  is the number of the unit cell composed in the horizontal direction and  $N_v$  is the number of the unit cell composed in the vertical direction; also, the edge thickness is determined by ( $e$ ). Finally, generating the 3D tubular structure, where  $T$ , and  $D_i$  and  $D_o$  are respectively determined in the longitudinal and circumferential directions by the Equations 4.6 and 4.7:

$$D_i = \frac{B}{\pi} - (2T) \quad [mm] \quad (4.6)$$

$$D_o = \frac{B}{\pi} \quad [mm] \quad (4.7)$$

Finally, from the unit cell parametrization, the equation 4.8 present the relative density  $\bar{\rho}$  of the structure being determined by  $(\rho/\rho_s)$ , which is the ratio of the apparent density of the cellular structure ( $\rho$ ) to the density of the cellular structure's material ( $\rho_s$ ), which determines how the mechanical properties of lattice structures are typically expressed as a fraction of the mechanical properties of their parent material.

$$\bar{\rho} = \frac{t(\pi r_1 + (2\pi + 4)r_2)}{16r_2^2 + 8r_1r_2} \quad (4.8)$$

To simplify the equation 4.9, can be described as the relationship between  $r_1$  and  $r_2$  as  $\lambda = r_1/r_2$ . This substitution allows us to rewrite the equation in terms of  $\lambda$ , making it easier to manage and simplify.

$$\bar{\rho} = \frac{t(\pi\lambda + 2\pi + 4)}{r_2(16 + 8\lambda)} \quad (4.9)$$

Figures 4.3(a) and 4.3(b) show the effects of the parameters  $r_1$  and  $r_2$  on the relative density ( $\bar{\rho}$ ). It is evident that the thickness ( $t$ ) has the most significant impact on increasing the relative density, as expected. Additionally, the influence of the parameters  $r_1$  and  $r_2$  is also noticeable. The combination of these two parameters shows that smaller values of  $r_1$  and  $r_2$  result in higher relative densities. This proportional relationship highlights the importance of carefully selecting  $r_1$  and  $r_2$  to achieve the desired relative density in the auxetic structure.

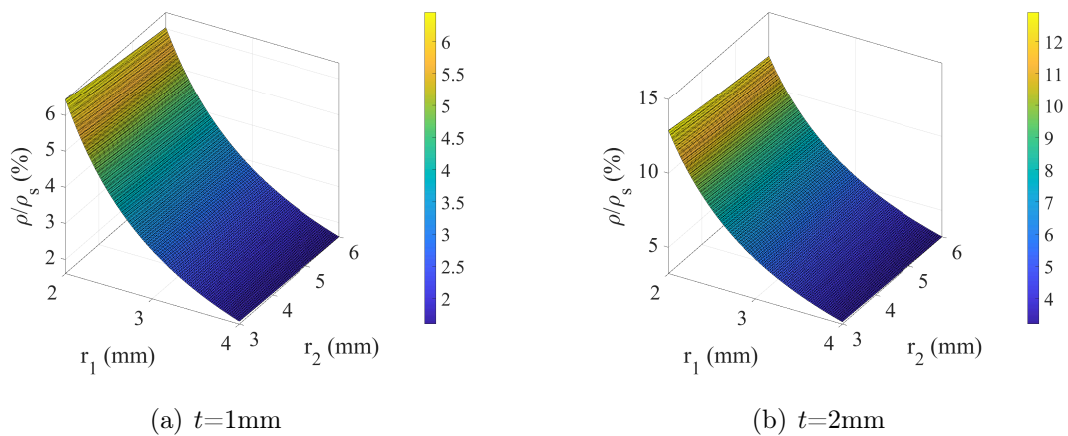


Figure 4.3 – The influence of  $r_1$  and  $r_2$  in the relative density of the DFW unit cell.

Henceforth, in order to substantiate the manifestation of negative Poisson's ratio behavior, a numerical simulation is delineated in Figure 5.19. In this context, the DFW auxetic unit cell is implemented within a tubular configuration. Evidently discernible in Figure 5.19 (b) and (c), the application of compression force results in transverse contraction of the structure, while traction force induces transverse expansion, respectively.

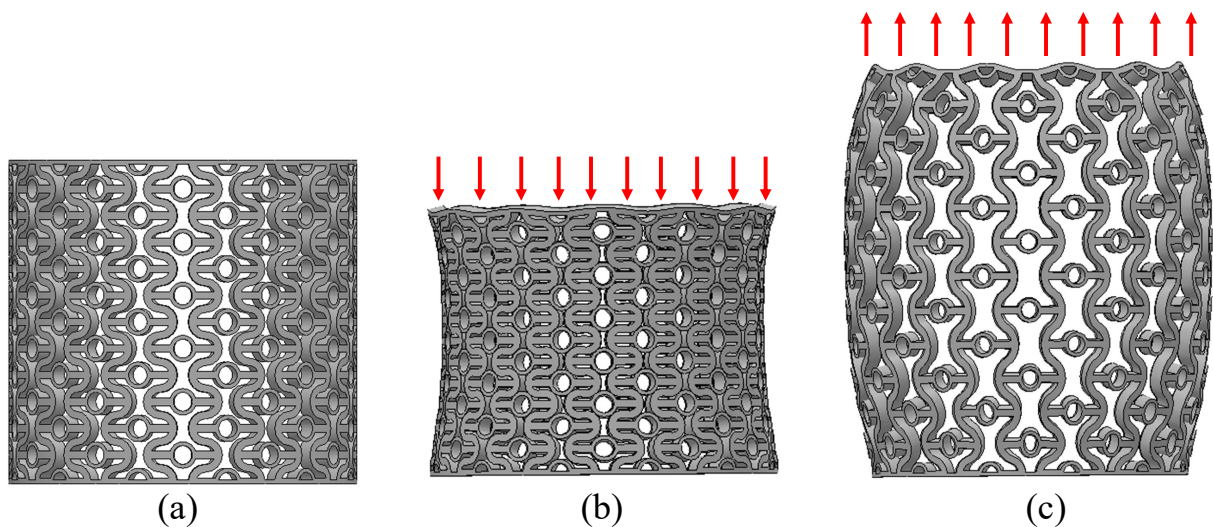


Figure 4.4 – Negative Poisson's behavior of the DFW unit cell applied in the tubular structure: (a) undeformed, (b) under compression, and (c) under traction.

### 4.2.1 TUBULAR STRUCTURE DESIGN

In the current investigation, we have developed two distinct types of auxetic tubular structures utilizing commercial CAD software. These structures include the newly introduced dragonfly-wing-shaped design, which was introduced in Section 2. The dragonfly-wing-shaped tubular structure designed into it comprises two models, namely DFW-A and DFW-B, each characterized by different geometry parameters, as illustrated in Figure 4.5. Additionally, a classical reentrant tubular structure was designed to facilitate a comparative analysis and validation of the mechanical properties. The design of this classical reentrant structure was inspired by the work proposed by Francisco *et al.* [32] and shares similar tubular geometry parameters such as diameter, length, and thickness.

The primary objective behind the proposed innovative design, which incorporates the inspiration by dragonfly wings, is to achieve a flexible stress-strain curve and enhance the energy absorption capacity through slight adjustments in the wings parameters, namely  $r_1$ ,  $r_2$ , and  $t$ . To substantiate the effectiveness of this novel tubular structure, two distinct sets of parameters were employed for comparison to the reentrant tubular design, where the first configuration, denoted as DFW-A, was determined based on the reentrant quantity of vertical unit cells ( $N_v$ ) and horizontal unit cells ( $N_h$ ). Meanwhile, the second configuration, labeled DFW-B, was developed with an emphasis on reentrant weight considerations.

#### 4.2.1.1 TUBULAR DRAGONFLY-WINGS-SHAPE (DFW)

Figure 4.5 shows the novel unit cell model applied in the tubular structures, where two fundamental unit cells are indicated by DFW-A and DFW-B, respectively. For the geometry of the DFW unit cell, distinct parameters were considered, deviating from those specified in Figure 4.2. The parameters of the radius  $r_1$  and  $r_2$  were modified to meet the desired specifications. The pertinent parameters utilized in the construction of the auxetic tubular structure with the DFW design are presented comprehensively in Table 4.1.

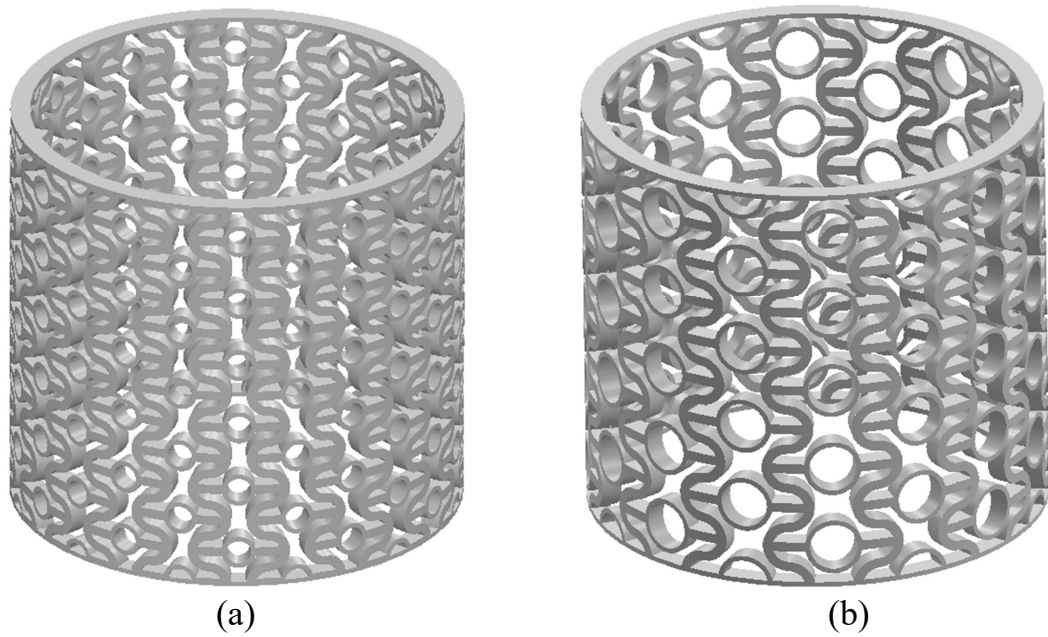


Figure 4.5 – Auxetic tubular structure: (a) DFW-A auxetic tubular structure and (b) DFW-B auxetic tubular structure.

Table 4.1 – Parameters of the auxetic dragonfly-wings-shape unit cell used in the tube construction.

Variable	Symbol	Unit	DFW-A Parameters	DFW-B Parameters
Radius length 1	$r_1$	mm	2.50	4.75
Radius length 2	$r_2$	mm	3.50	4.25
Center distance	x	mm	3	8.50
Horizontal length	b	mm	19	26.50
Thickness	t	mm	2	2
Height of unit cell	h	mm	14	17
Length of tube	L	mm	85.20	85.20
Perimeter of the tube	B	mm	288	288
Outer diameter of the tube	$D_o$	mm	91.68	91.68
Thickness of tube	T	mm	4	4
Edge thickness of tube	e	mm	0.60	0.60
Number of horizontal cell	$N_h$	-	24	16
Number of vertical cell	$N_v$	-	6	5
3D model mass	m	g	54.60	41.10

#### 4.2.1.2 REENTRANT (RE)

The reentrant (RE) unit cell was the first structure developed that presented an auxetic behavior, and it is one of the most studied unit cells by researchers around the world [28]. The reentrant unit cell is composed of a hexagonal model, where the Figure 4.6 (a) presents the geometric parameters of the reentrant unit cell [4, 32]. These unit cells have been used over time as a base to develop and compare the novel auxetic structure with



the goal of evaluating and comparing its mechanical proprieties. Therefore, Figure 4.6 (b) presents the reentrant auxetic tubular structure designed and optimized by Francisco *et al.* [32] which was used to validate the mechanical proprieties of the novel DFW auxetic unit cell. The pertinent parameters utilized in the construction of the auxetic tubular structure with the reentrant design are presented comprehensively in Table 4.2.

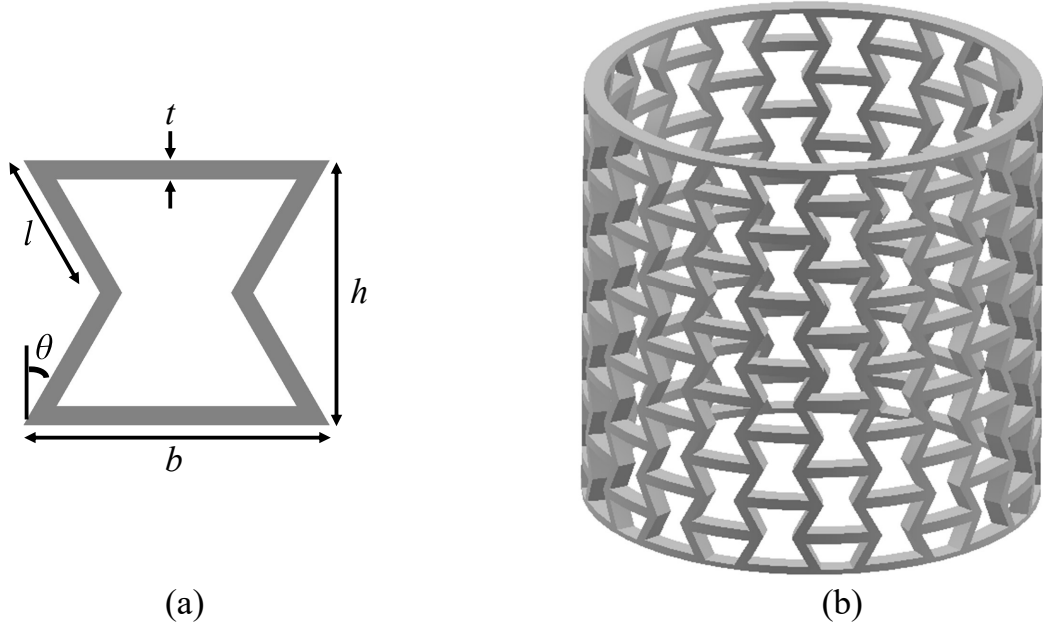


Figure 4.6 – Auxetic tubular structure: (a) Reentrant unit cell parametrization and (b) Reentrant auxetic tubular structure (adapted from [32]).

Table 4.2 – Parameters of the auxetic reentrant cell used in the tube construction.

Variable	Symbol	Unit	Value
Angle	$\theta$	degrees	60
Oblique length	$l_o$	mm	8
Horizontal length	$b$	mm	16
Thickness	$t$	mm	2
Height of unit cell	$h$	mm	13.85
Length of tube	$L$	mm	85.20
Perimeter of the tube	$B$	mm	288
Outer diameter of the tube	$D_o$	mm	91.68
Thickness of tube	$T$	mm	4
Edge thickness of tube	$e$	mm	0.60
Number of horizontal cell	$N_h$	-	24
Number of vertical cell	$N_v$	-	6
3D model mass	$m$	g	40

## 4.2.2 MATERIAL PROPERTIES

The properties of the original material are altered during the 3D printing manufacturing process, together with the build orientation chosen for creation and the anisotropic

nature of the fused deposition modeling (FDM) procedure. In this way, to find the properties of the material used, five specimens were built Figure 4.7(a) also according to the Standard Test Method for Compressive Properties of Rigid Plastics (ASTM D695), is required to perform the test in five sample, where the samples are presented in the Figure 4.7(b), and finally the test of the samples is showed in Figure 4.7(c). To manufacture the samples, printer using PLA filament with a diameter of 1.75 mm. The printing temperature and the build plate temperature are equal to 210 °C and 60 °C, respectively. The print speed, the layer height, and the infill density are equal to 30 mm/s, 0.2 mm, and 100%, respectively, where the property data found will be used to feed the numerical model. Resultant material properties are listed in Table 5.2 and the values are used to perform the finite element analysis.

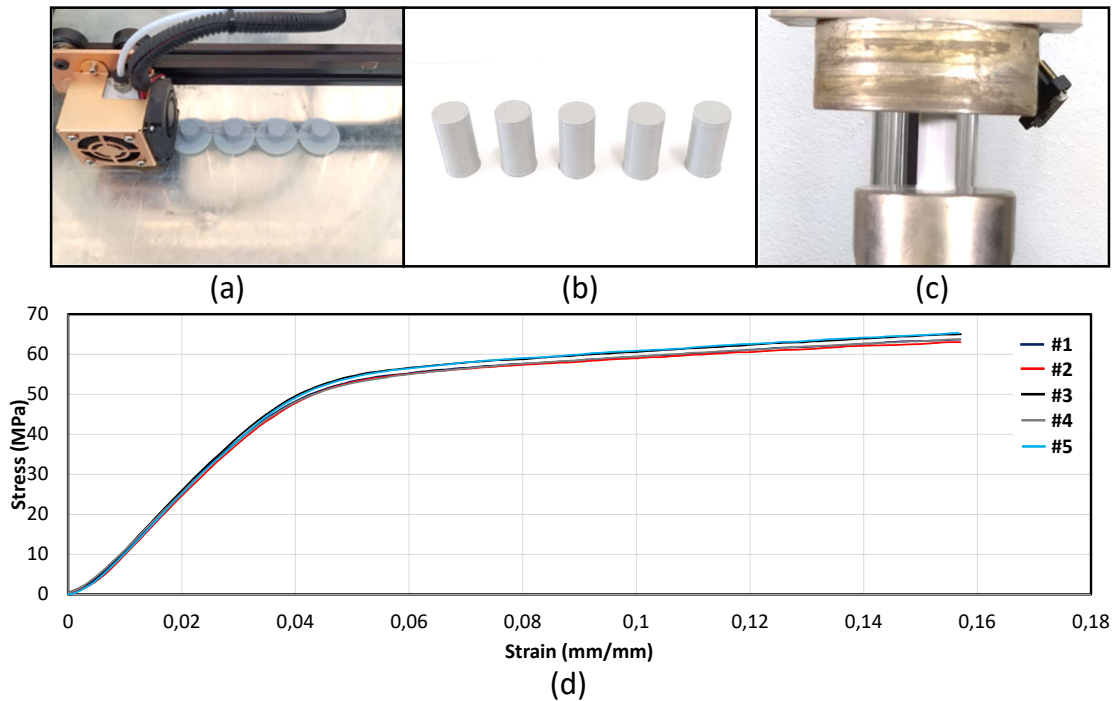


Figure 4.7 – Material proprieties: (a) printing process, (b) compression sample test, (c) compression test, (d) stress vs strain curve.

Table 4.3 – Properties of PLA (ASTM D695 ).

Property	Acronyms	Mean Value	Unit
Elastic Modulus	E	1.408	GPa
Tangent modulus	$E_t$	113.000	MPa
Yield Stress	$\sigma_s$	48.300	MPa
Max. Stress	$\sigma_u$	65.000	MPa
Density	$\rho$	1157.010	kg/m <sup>3</sup>
Poisson's ratio	$\nu$	0.330	-

## 4.2.3 FINITE ELEMENT MODELING SIMULATIONS

The process of conducting numerical simulations to investigate the mechanical behavior of Dragonfly Wings Shape DFW and Reentrant RE auxetic unit cells incorporated within a tubular structure was undertaken using the dynamic explicit module offered by ANSYS Workbench. For the purpose of performing comprehensive structural analyses, the solid tetrahedral element was deliberately chosen (SOLID 187). This particular element exhibits linear behavior characteristics, affording three degrees of freedom at each node, thereby imparting it with the capability to deliver enhanced precision in the assessment of deformation phenomena, especially when confronting complex geometrical configurations. Finally an analysis was conducted on the convergence of element sizes across all models, the relative error between adjacent element size was computed as the percentage difference for each individual output variables, and when the further increase in mesh density does not change the output variables by more than 5%.

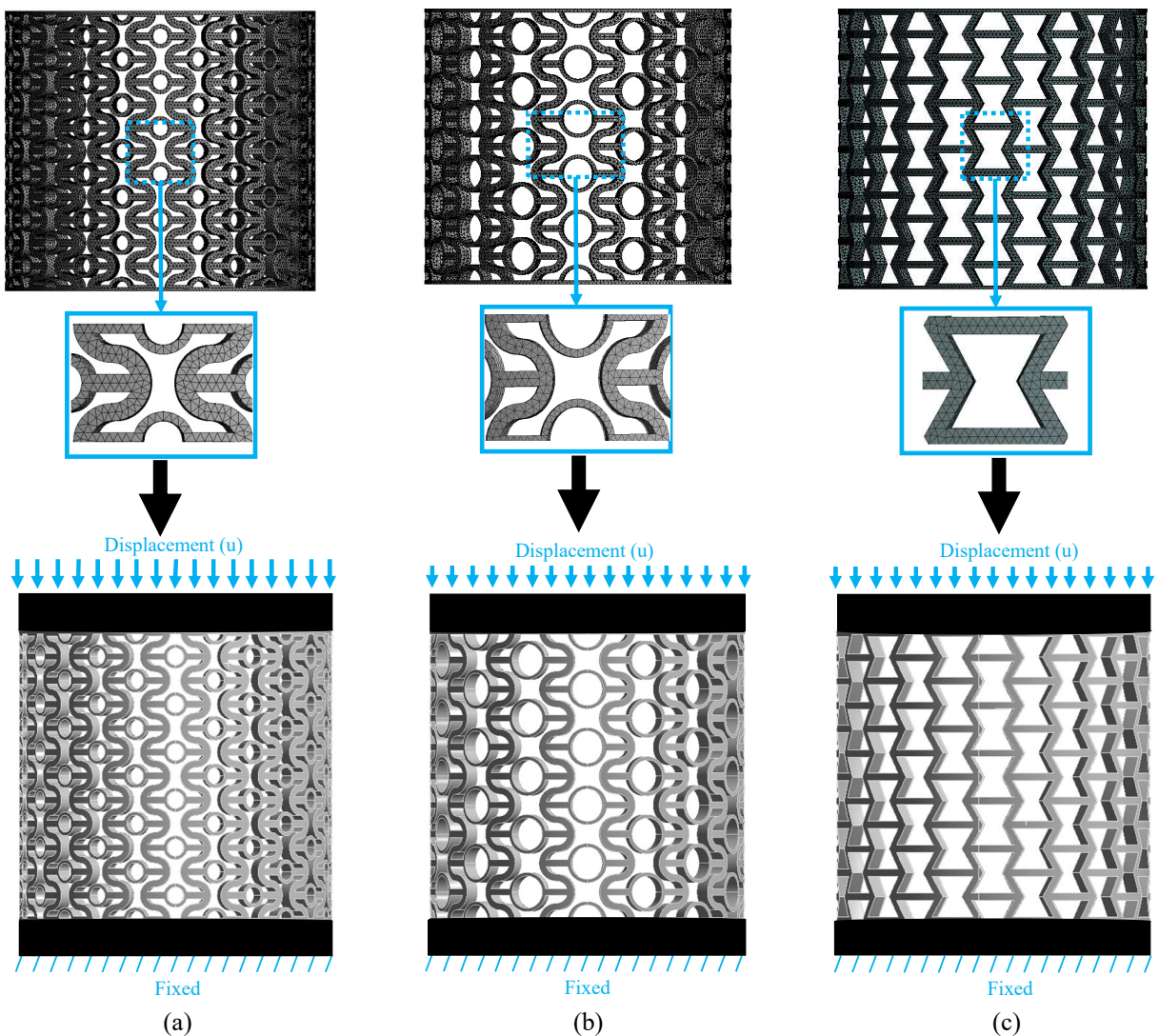


Figure 4.8 – Finite element methodology process: (a) DFW-A, (b) DFW-B, and (c) RE.

## 4.3 EXPERIMENTAL STUDY

### 4.3.1 SAMPLES MANUFACTURING

The auxetic tubular structures were manufactured via additive manufacturing on the Trevo Tornado printer using PLA filament with a diameter of 1.75 mm. The printing temperature and the build plate temperature are equal to 210 °C and 60 °C, respectively. The print speed, the layer height, and the infill density are equal to 30 mm/s, 0.2 mm, and 100%, respectively. The structures were designed in CAD software and posteriorly imported into the Ultimaker CURA<sup>®</sup> software, where all the configurations for printing were done.

The PLA material was chosen due to the studies carried out by Vyavahare and Kumar [150] and Yang *et al.* [151]. Where both authors performed a comparison of the properties of PLA with other materials using additive manufacturing (3D printing). PLA has a greater compressive strength than ABS, according to research by Vyavahare and Kumar [150]. Furthermore, Yang *et al.* [151] came to the conclusion that the PLA's performance in their laboratory testing outperformed that of other materials. Also, PLA is a material that has the possibility of being recycled, which is a promising solution for reducing the cost and environmental impact [152].

The Figure 4.9, present a part of the manufacturing process of the auxetic tubular structures and the finish structure of the DFW-A, DFW-B, and RE, respectively.

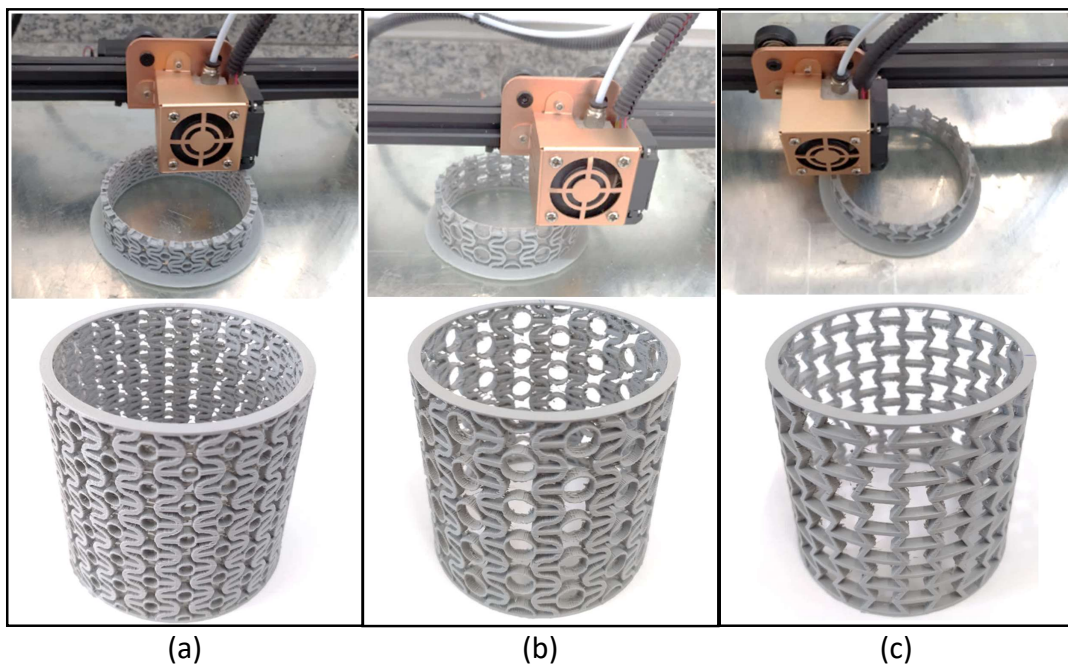


Figure 4.9 – Printing process of the structure using PLA and final auxetic structure: (a) DFW-A, (b) DFW-B, and (c) RE.

### 4.3.2 COMPRESSIVE TEST

The Figure 4.10, presents the compressive test performed on all the specimens (DFW-A, DFW-B, and RE structures) to study the deformation mode, load displacement curves, and energy absorption capacity of the auxetic tubular structures. The compressive axial load was applied to the upper extremities at a constant speed of 2 mm/min, the tests were carried out using a universal testing machine, the EMIC DL-30000, equipped with a 50 kN load cell and controlled by the Tesc software program, and a Canon T5 camera was also used to register the experimental test. All the experiments and specimen manufacturing were realized the Smart Structures Laboratory at Universidade Federal de Itajubá.

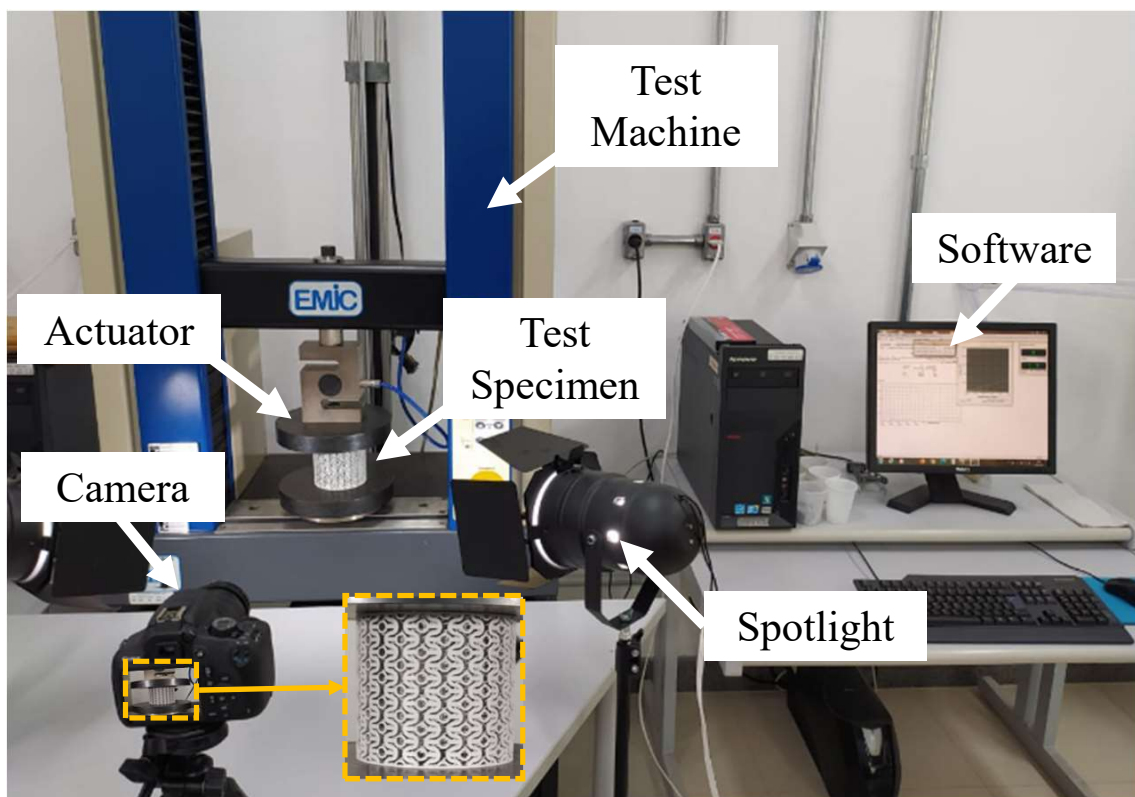


Figure 4.10 – Experimental test setup.

#### 4.3.2.1 DIGITAL IMAGE CORRELATION (DIC)

To evaluate experimentally the Poisson's ratio, and to analyze the NPR behavior of the novel structure proposed in tubular structure were used the DIC methodology. Where the samples were prepared according to Figure 4.11, to perform the experimental test, a Canon T5 camera was used to register the test, and open source software was used to evaluate the displacement in  $x$  axis and also in the  $y$  axis, making it possible to calculate and evaluate the structure's Poisson's ratio per engineering strain. Due the tubular geometry the analyses were made using the central unit cell as a reference to the measure.

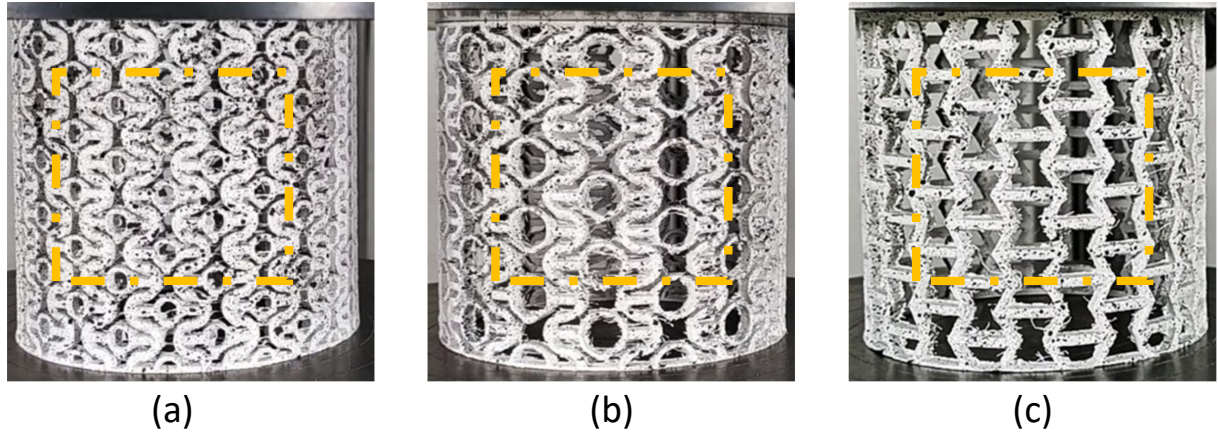


Figure 4.11 – Auxetic structure from DIC: (a) DFW-A, (b) DFW-B, and (c) Reentrant.

## 4.4 NUMERICAL-EXPERIMENTAL RESULTS

### 4.4.1 COMPARATIVE ANALYSIS: EXPERIMENTAL FINDINGS AND NUMERICAL SIMULATIONS

In this section, we present the validation of the numerical analysis through experimental tests. One of the significant advantages of the novel DFW structures compared to the conventional re-entrant honeycomb structure is the elimination of stress concentrators due to the curved geometry. This unique design feature results in improved stress distribution, which enhances the structural performance under compressive loading.

Figure 4.12 illustrates the comparison of the von Mises stress (MPa) in the structures during compression. When the structures were deformed by 12 mm along the  $y$ -axis, the following observations, where the DFW-A structure exhibited 65% lower stress in the maximum stress compared to the conventional RE structure, the DFW-B structure demonstrated an impressive 118% reduction in stress in the maximum compared to the conventional re-entrant structure.

These results highlight the superior performance of the DFW structures under compressive loads. The reduction in stress concentrations suggests that the DFW unit cells can better distribute the applied forces, improving their overall resistance to deformation. Consequently, this leads to enhanced EA capabilities.

The improved resistance to compressive loads and the ability to absorb more energy make the DFW structures highly advantageous for applications requiring efficient energy dissipation and structural integrity. These findings corroborate the experimental results and validate the effectiveness of the dragonfly wing-inspired design in enhancing the mechanical performance of auxetic structures.

The numerical analysis, therefore, confirms that the bio-inspired geometry not only mitigates stress concentrations but also provides a robust and efficient alternative to traditional re-entrant honeycomb structures.

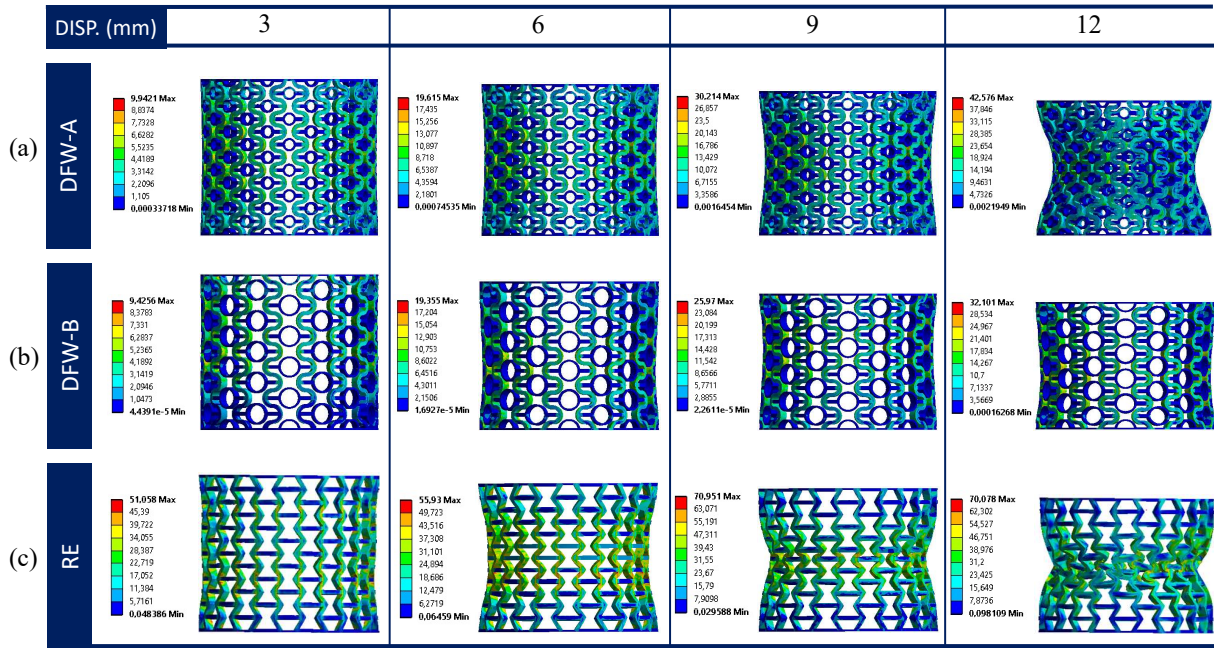


Figure 4.12 – Numerical Von-Mises stress ratio: (a) DFW-A, (b) DFW-B, and (c) RE.

Figure 4.13 illustrates the deformation characteristics of the DFW-A, DFW-B, and conventional re-entrant RE structures, facilitating a comparative analysis between experimental findings and finite element deformation models. This comparison is crucial for validating the accuracy and reliability of our numerical simulations.

In the figure 4.13, the alignment of results between the experimental tests and the numerical analyses is clearly visible, demonstrating the precision of our finite element models. The close match between the experimental deformations and the simulated ones indicates that our numerical models accurately capture the mechanical behavior of the structures under compressive loading. Also is possible to analyze the behavior of the unit cell applied in the tubular structure, where the unit cell behavior in the tubular structure exhibits NPR characteristics due to its geometry, which consists of circumferences parameterized by  $r_1$  and  $r_2$ , these parameters facilitate an auxetic behavior, allowing the cell to expand when the structure is stretched, also the interconnected network design supports lateral expansion in response to longitudinal stretching.

The consistency between the experimental and numerical results not only attests to the accuracy of the simulations but also validates the finite element model used in this study. This validation is essential as it provides confidence in the overall reliability of our findings and supports the use of our numerical approach for predicting the performance of similar auxetic structures.

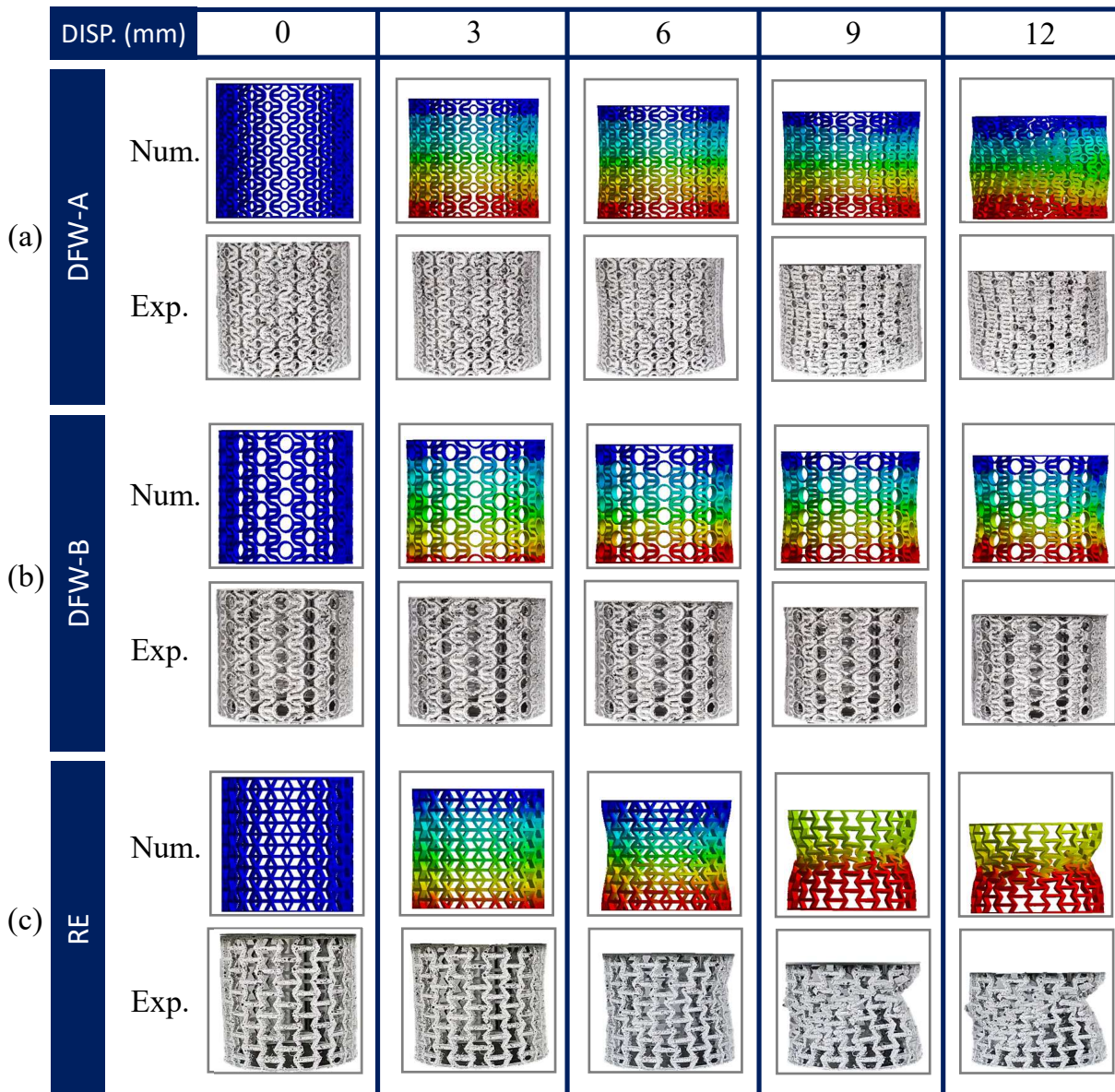


Figure 4.13 – The comparison of deformation model between EXP and FEM: (a) DFW-A, (b) DFW-B, and (c) RE.

Figure 4.14 present the experimental outcomes of Poisson's ratio, experimentally acquired through the DIC methodology, compared with the corresponding numerical model, where as findings align, it is clear how precise the numerical assessments were, confirming the accuracy of the models. It is noteworthy that, up to the  $y$  axis deformation, the stability of DFW unit cells surpasses that of the Reentrant, however it exhibit a higher Poisson's ratio. Specifically, at a 6 mm deformation which were used as base until the fracture of the structures, DFW-A and DFW-B demonstrated Poisson's ratios of -0.5 and -0.3, respectively, while the reentrant exhibited a Poisson's ratio of -1.3.



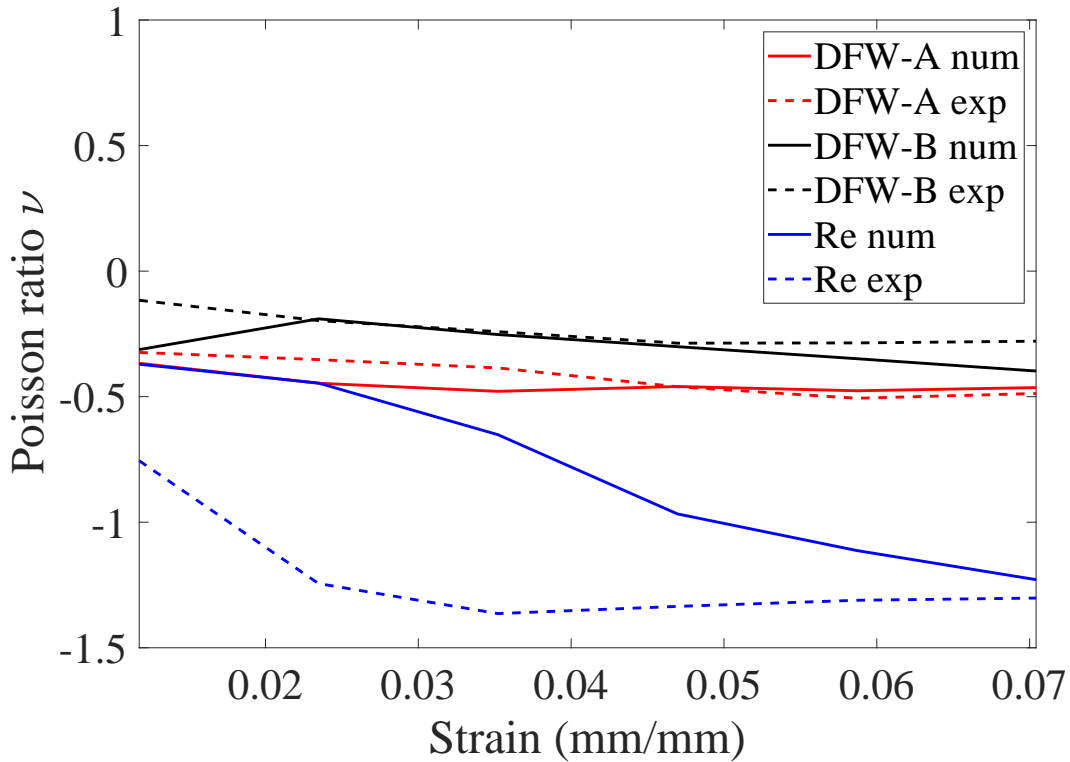


Figure 4.14 – Numerical *vs.* Experimental Poisson's ratio results.

Figure 5.2 presents the ANOVA main effect plot analysis conducted to evaluate the impact of each unit cell parameter on the auxetic structure's performance. To achieve this, a DOE composed of a full factorial design was created using the following parameter ranges:  $2 \leq r_1 \leq 4$ ,  $3 \leq r_2 \leq 6$ , and  $1 \leq t \leq 2$ . By employing these ranges and utilizing FEM tools, it was analyzed how each parameter influences the key characteristics of the unit cell, such as the Poisson's ratio and stress distribution.

The ANOVA analysis helped systematically assess the significance of each parameter, providing insights into their individual and combined effects on the mechanical behavior of the auxetic structure. This approach enables a comprehensive understanding of how variations in  $r_1$ ,  $r_2$ , and  $t$  contribute to the overall performance, allowing us to identify the most critical factors that enhance the desired properties. Therefore, integrating DOE with FEA analysis, we can effectively explore the parameter space and gain valuable insights into the mechanical behavior of the unit cell design. The findings from this analysis demonstrate the robustness of our design methodology and highlight the importance of precise parameter tuning.

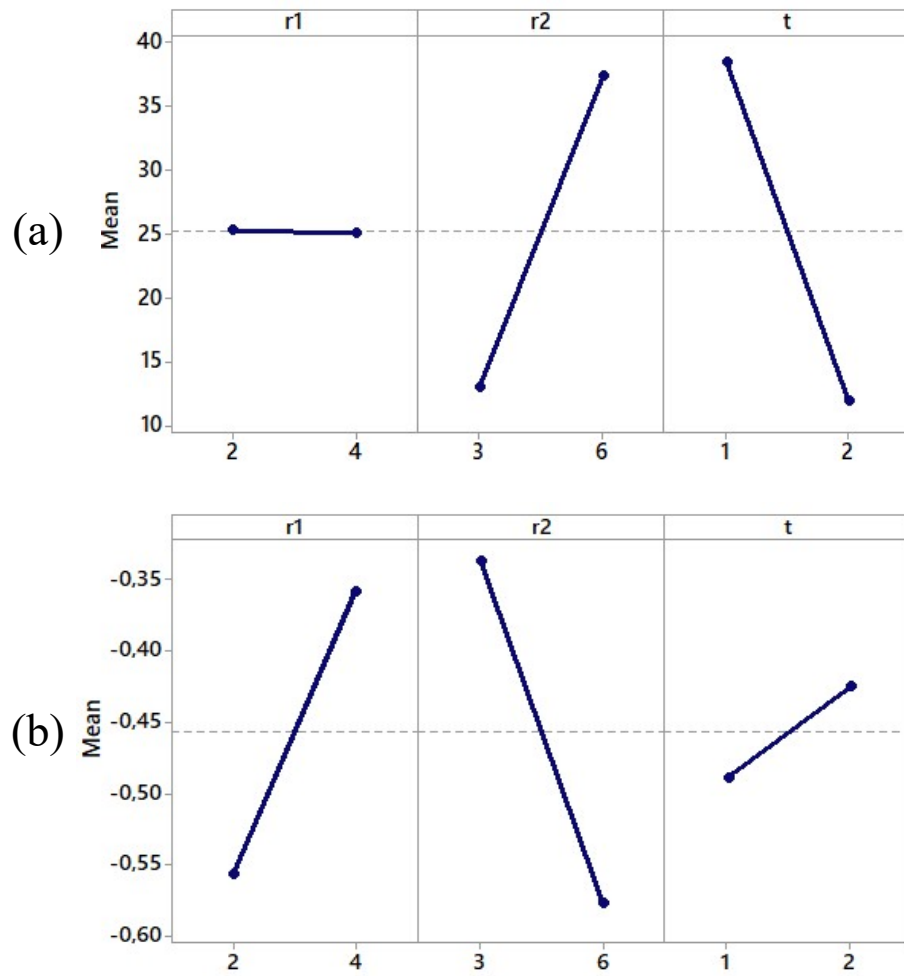


Figure 4.15 – Main Effect Chart: (a) Stress, (b) Poisson.

Finally, analyzing the results presented in Figure 4.15, it is possible to observe the main effects on both Poisson's ratio and stress. In the stress analysis shown in Figure 4.15(a), it is evident that the radius  $r_1$  is not statistically significant for compression analysis. However,  $r_1$  become significant in other analyses such as bending, torsion, or shear. Conversely, the radius  $r_2$  has a significant impact on stress, with smaller  $r_2$  values correlating with lower stress levels. Additionally, as expected, increasing the thickness  $t$  results in reduced stress levels within the structure.. From the Poisson's ratio analysis illustrated in Figure 4.15(b), the radius sizes ( $r_1$  and  $r_2$ ) exhibit the most significant impact. Notably, the most negative Poisson's ratio occurs when  $r_1$  is minimized and  $r_2$  is maximized. Additionally, the thickness ( $t$ ) also influences the Poisson's ratio, with thinner structures resulting in more negative Poisson's ratio values.

These insights provide a strong foundation for future work aimed at optimizing the unit cell design. By leveraging the data obtained from this analysis, we can perform a more detailed optimization study to fine-tune the geometrical parameters ( $r_1$ ,  $r_2$ , and  $t$ ) and achieve improved mechanical performance of auxetic structures. Future research will focus on systematically varying these parameters to identify the optimal configuration

that minimizes the Poisson ratio, minimizes stress concentrations and increase the ability to absorb energy.

#### 4.4.2 MECHANICAL PROPRIETIES

The energy absorption and dissipation characteristics exhibited by mechanical systems find extensive applications in various facets of daily life, spanning from mitigating the effects of shock impacts to addressing mechanical vibrations. Within the scope of the present investigation, we evaluated the energy absorption capabilities of the novel auxetic dragonfly wings-shaped unit cell applied in a tubular structure and the reentrant auxetic tubular structure. The assessment was conducted through experimental compression tests, and to validate the accuracy of the analysis, numerical analyses employing the FEA were performed. The results obtained from both analyses will be discussed and presented in this section.

The EA capabilities of the tube in a compression test can be mathematically calculated using the Equation 3.1. In order to compute the SEA, a proposition is made to express the EA relative to mass ( $M$ ), as elucidated in Equation 3.2. Moreover, the characterization of energy absorption per loading displacement ( $d$ ) is introduced to enable the computation of the MCF for the NPR structure, as articulated in Equation 3.3. Finally, one of the most important characteristics and behaviors of auxetic structures is the Poisson's ratio, which provides the link between longitudinal and transverse strain which is represented by the Equation 3.4.

After performing the experimental compression tests, the force-displacement findings and the properties of absorbed energy EA, specific absorbed energy SEA, and main crushing force MCF were directly acquired from the respective Eqs 3.1, 3.2, and 3.3. Figure 4.16 present the results of the force per displacement obtained by the compression test for the auxetic tubular structures manufactured with PLA filament. It is possible to observe that the results demonstrate good reproducibility with a small standard variation across repetitions, which is a sign of an effective additive manufacturing method. It is also possible to note that the samples composed of the DFW unit cell presented more resistance when compared to the conventional Reentrant unit cell. When comparing the different unit cells developed (DFW-A, DFW-B, and RE), it is possible to note that the structures present different behaviors during the compression test, where the DFW-A resisted the highest load and also the DFW-B demonstrated greater resistance to displacement.

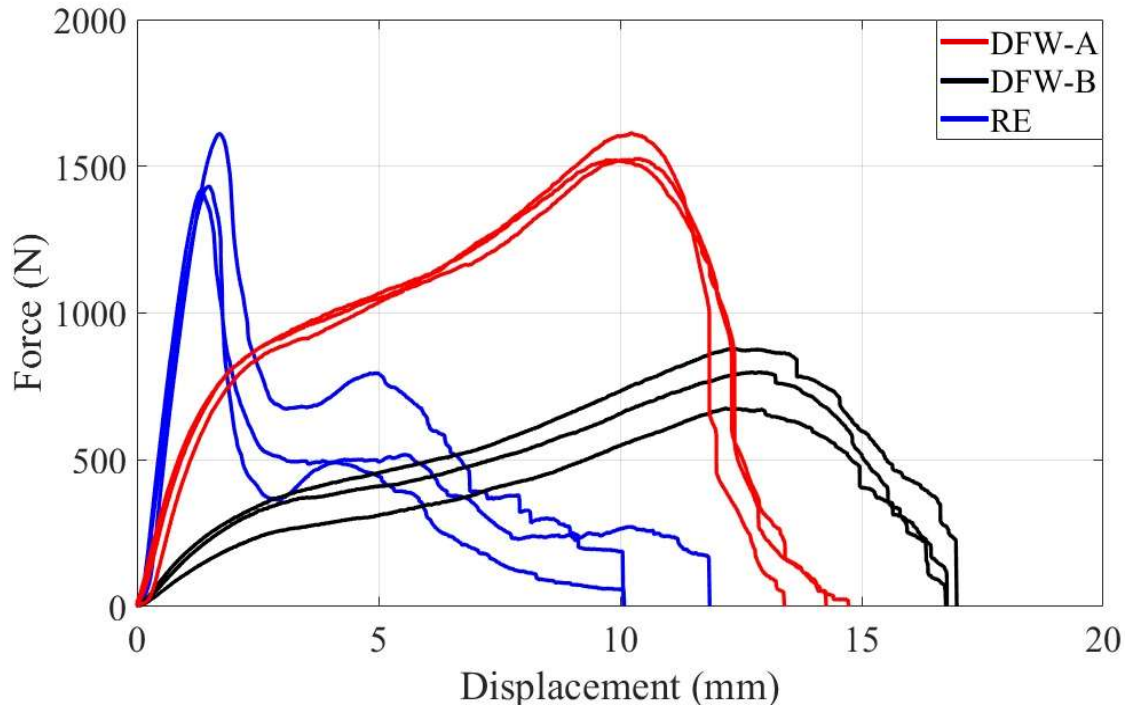


Figure 4.16 – Compression results for the auxetic tubular structures: (a) DFW-A, (b) DFW-B, and (c) RE.

Of significant importance as well, Figures 4.17, 4.18, and 4.19 depict the response exhibited by each individual respective structure DFW-A, DFW-B, and RE throughout the course of the compressive experimental assessment. This depiction facilitates the observation of alterations in structural configuration during the testing procedure, thereby showcasing the distinctive NPR.

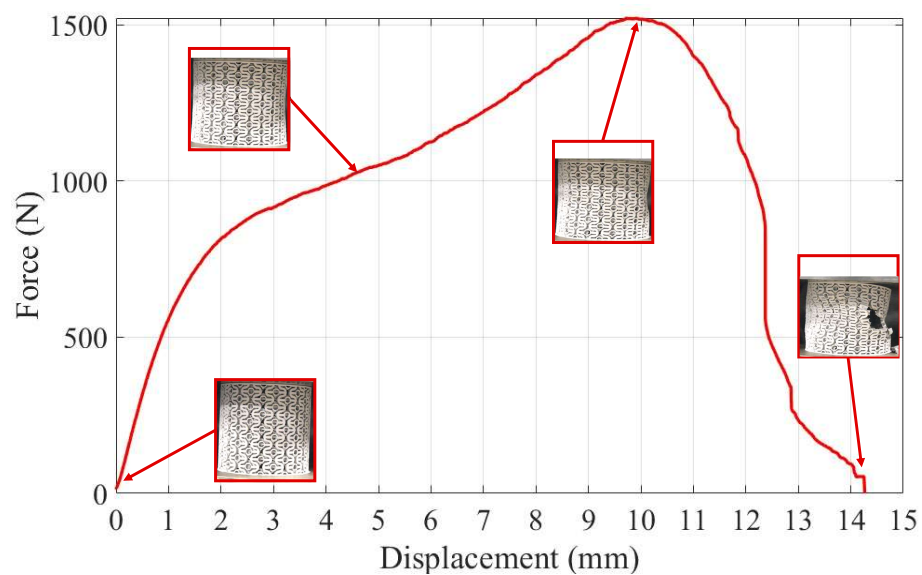


Figure 4.17 – Compression results for the DFW-A auxetic tubular structures.

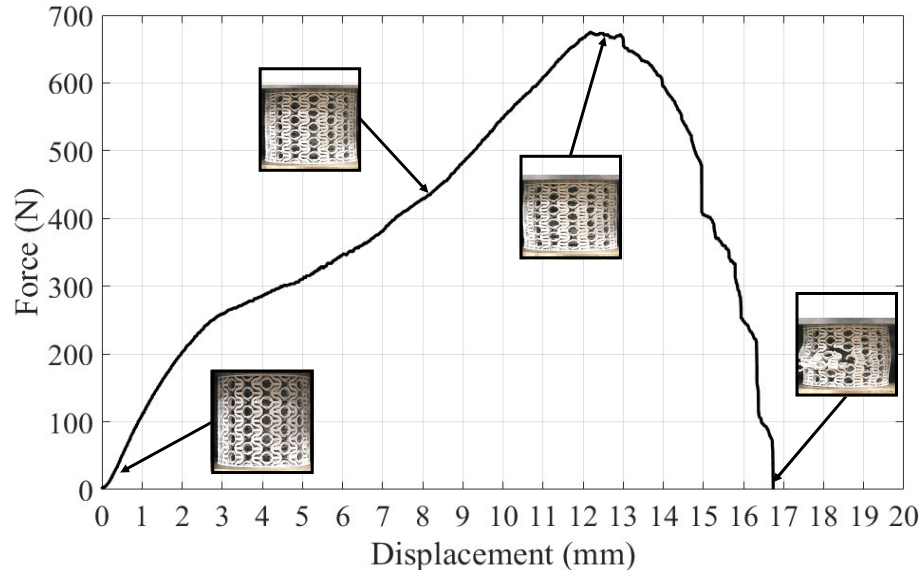


Figure 4.18 – Compression results for the DFW-B auxetic tubular structures.

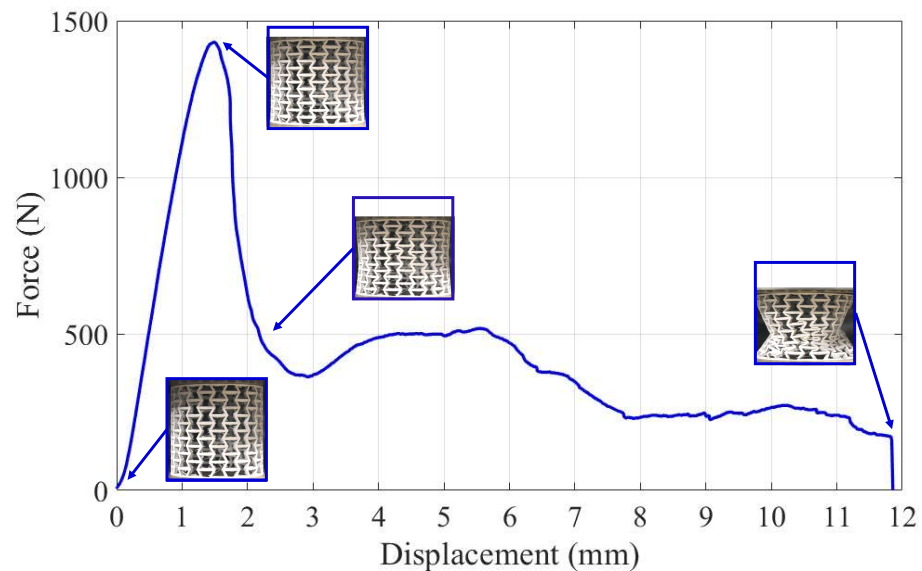


Figure 4.19 – Compression results for the RE auxetic tubular structures.

The outcomes of energy absorption by the manufactured structures are depicted in Figure 5.15, as derived from Equation 3.1. In both configurations, the novel unit cell exhibited superior displacement, resulting in greater energy absorption compared to the conventional reentrant design. Notably, the DFW-A configuration displayed a remarkable 163% increase in energy absorption over the classical reentrant, while the DFW-B configuration exhibited a substantial 79% enhancement. These improvements were facilitated by the enhanced load-bearing capacity and displacement resistance of both novel structures.

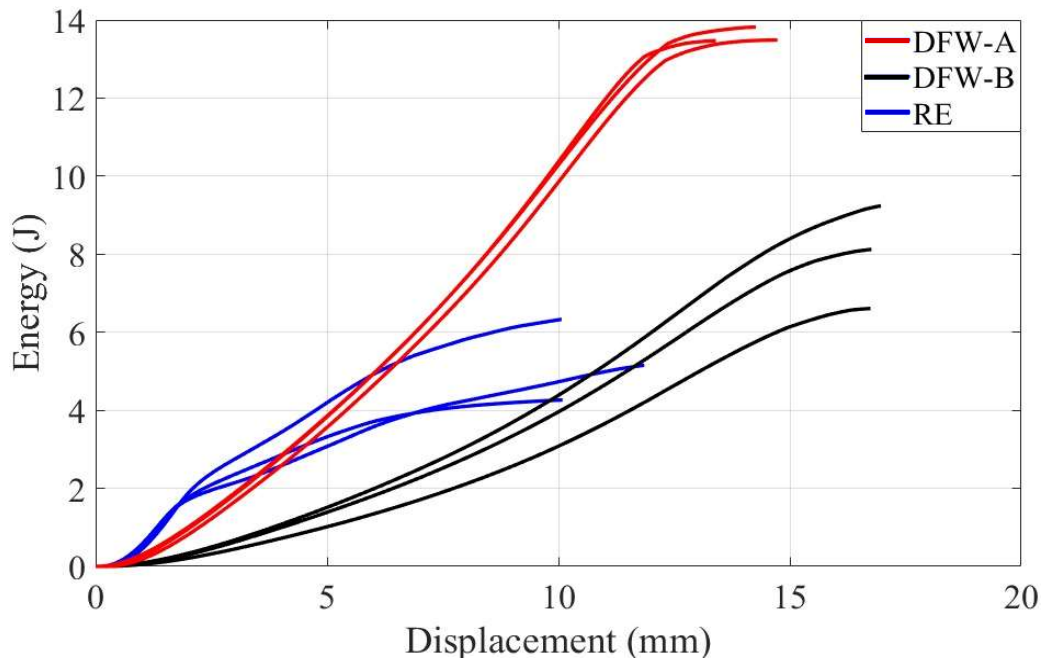


Figure 4.20 – Experimental energy absorption results for the auxetic tubular structures: (a) DFW-A, (b) DFW-B, and (c) Reentrant.

Equally important, the Figure 4.21 exhibits the Specific Energy absorption for all auxetic models with different structures. By analyzing the box plot graph of the auxetic tubular structure composed of Dragonfly wings shape (DFW-A) unit cell data, it is possible to see that even though it had the biggest mass, it presented superiority in terms of SEA and also presented a lower standard deviation. Finally, Tab. 4.4 displays and categorizes the outcomes derived from the force-displacement signal analysis for the structures examined in sets of three replicates.

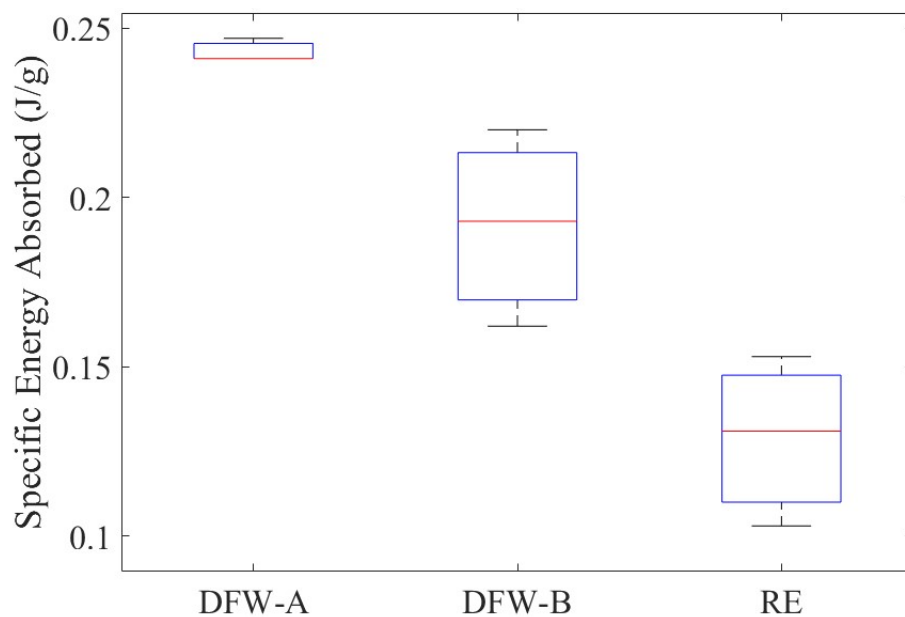


Figure 4.21 – Experimental specific energy absorption results for the auxetic tubular structures: (a) DFW-A, (b) DFW-B, and (c) RE.

Table 4.4 – Experimental results of auxetic tubular structures manufactured with PLA filament

Model	Sample	Mass (g)	Disp. (mm)	Force (N)	EA (J)	SEA (J/g)	MCF (N)	
DFW-A	1	56.08	14.73	1525	13.490	0.241	0.916	
	2	55.94	14.27	1522	13.820	0.247	0.968	
	3	55.89	13.40	1613	13.470	0.241	1.005	
	Mean	-	55.970	14.133	1553	13.593	0.243	0.963
	SD	-	0.080	0.552	42.208	0.160	0.003	0.037
DFW-B	1	42	16.97	878.16	9.238	0.220	0.544	
	2	40.89	16.74	674	6.608	0.162	0.395	
	3	42	16.79	798.17	8.122	0.193	0.484	
	Mean	-	41.63	16.83	783.44	7.99	0.192	0.474
	SD	-	0.523	0.099	83.996	1.078	0.024	0.061
RE	1	39.28	11.86	1431.1	5.155	0.131	0.435	
	2	41.4	10.1	1417.2	6.236	0.153	0.626	
	3	41.56	10.07	1610.3	4.265	0.103	0.424	
	Mean	-	40.75	10.68	1486.2	5.25	0.129	0.495
	SD	-	1.039	0.837	87.935	0.844	0.021	0.093

Figure 4.22 illustrates the mean mechanical properties of the structures as detailed in Table 4.4. It is noteworthy that the structure denoted as DFW-A, inspired by the number of unit cells, demonstrates superior mechanical properties, specifically in terms of energy absorption, specific energy absorption, and main crushing force, in comparison to structures developed with equivalent weight (DFW-B) and the Reentrant structure. Notably, DFW-A outperforms the classical Reentrant in all examined mechanical properties.

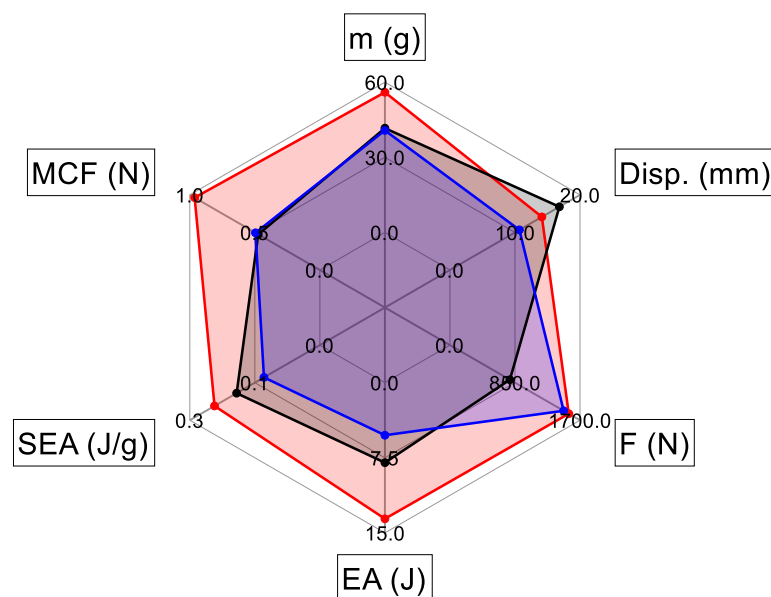


Figure 4.22 – Comparison of the mechanical proprieties (legend: ■ DFW-A, ■ DFW-B, ■ Reentrant).

## 4.5 CHAPTER CONCLUSION

In this work, novel auxetic unit cells inspired by a dragonfly wing shape have been designed, applied in a tubular structure, fabricated using PLA filament, and examined experimentally and numerically. Firstly, the design, using the idea of reducing the stress concentration using curve shapes, was designed and parameterized, and it was also possible to evaluate the relative density of the unit cell. Secondly, three structures were developed: the novel auxetic unit cell was applied in a tubular structure and compared to a classical reentrant unit cell in two ways: the first with the same unit cell quantity and the second with the same weight. Then, we performed an experimental compression test to evaluate the energy absorption of the structures. Finally, it was possible to validate the numerical model using finite element analysis from the experimental test, which evaluated the effect of the Poisson's ratio, the stress concentration, and the deformation on the mechanical properties of the auxetic tubes. The following conclusions can be drawn:

The DFW unit cell was developed with the goal of reducing stress and increasing the ability to absorb energy. The study presented a novel unit cell, and it was also possible to parameterize and evaluate the effects of the relationship between the radius 1 and 2 called  $\lambda$  in the relative density of the structure. It was possible to note that the relationship between  $\lambda$  and relative density is inversely proportional; therefore, the smaller  $\lambda$ , the bigger the relative density.

With the goal of validating the structure, a comparison was proposed with the classical Reentrant unit cells, where the two structures developed (DFW-A and DFW-B) presented pros and cons, where the mechanical proprieties such as the energy absorption of the structure inspired in the number of unit cells (DFW-A) presented better mechanical proprieties results such as the energy absorption, specific energy absorption, and the main crushing force when compared to the structure developed with the same weight (DFW-B), but due to the geometry, the DFW-B presented less stress concentration. For future work, it is recommended to validate only based on the quantity of unit cells.

From the experimental tests, it was possible to note that the novel unit cells presented better mechanical properties, where the DFW-A configuration displayed a remarkable 163% increase in energy absorption over the classical reentrant, while the DFW-B configuration exhibited a substantial 79% enhancement.

The precision of the numerical analyses is evident, as reflected in the alignment of results, attesting to the accuracy of the simulations, which enable the evaluation of Poisson's ratios. DFW-A and DFW-B demonstrated Poisson's ratios of -0.5 and -0.3, respectively, while the RE exhibited a Poisson's ratio of -1.3. Also, it enables us to evaluate



the stress concentration, where when the structures were deformed 12 mm in the y axis, the DFW-A and DFW-B structures performed 65% and 118% lower stress than the conventional Reentrant.

The qualities and the performance of the innovative auxetic unit cell (DFW) enable to be applied in a variety of fields, including mechanical engineering and protective equipment. Nevertheless, the mechanical characteristics of the novel auxetic tube under quasi-static compression have been the exclusive focus of our work. The mechanical characteristics of the metallic or composite auxetic tubular materials under impact and other loading scenarios need to be further investigated. The suggested DFW improves the auxetic tube's energy absorption and serves as a guide for the development of safety equipment and applications in the aerospace sector.

# 5 OPTIMIZATION OF AUXETIC TUBULAR STRUCTURES WITH DRAGONFLY-WING-SHAPE CELLS THROUGH ADVANCED MULTIOBJECTIVE OPTIMIZATION TECHNIQUES

## 5.1 CHAPTER INTRODUCTION

Structures composed with Negative Poisson Ratio (NPR), called by Evans *et al.* [146] as auxetic structures, have an unusual behavior. Where it is very common to expect that when traction, the material will become longer in the direction of stretching and thinner in cross-section, but in the case of auxetic structures under compression, they contract transversely and, under traction, they expand transversely. These behaviors can be achieved from the material, and the structure's geometric parameters may not be necessary if it is composed of auxetic material. The auxetic effect, the structure is able to distribute stress more uniformly, which reduces the likelihood of fatigue, mechanical failure, and permanent deformations. Furthermore, these structures can serve as effective vibration absorbers in a variety of applications because of their flexibility in responding to varying stresses.

The application of auxetic unit cells in tubular structures has attracted a lot of attention due to their mechanical properties. Recently, Gomes *et al.* [28] performed a review of the auxetic tubular structures, presenting the benefits of the auxetic tubular structures, also in agreement Ramezani *et al.* [153] performed a review of the potential and applications of auxetic tubular structures in diverse sectors such as automobile manufacturing, aerospace, medicine, and textiles. Francisco *et al.* [4] performed a compressive review of the ability to absorb energy of the auxetic structures and presented the benefits and importance of their applications in the modern world.

Since the first auxetic unit cell the reentrant proposed in the literature by Lakes *et al.* [1] in 1987, and posteriorly in 1999 the application in tubular structure of the reentrant unit cell was proposed by Xu *et al.* [42], many authors have been studying, proposing application and solutions using auxetic tubular structures. Zhang *et al.* [69] developed an auxetic tubular structure composed of a novel unit cell based on a peanut shape. The authors found that it exhibited great and unique deformation characteristics under uniaxial compression. An auxetic tubular structure was constructed by Zolfagharian *et*

*al.* [75] employing “soft and stiff unit cells” which are multi-stiffness unit cells made up of two multi-stiffness re-entrant unit cells. The authors conclude that the multi-stiffness reentrant unit cells provided long cylindrical tubes with global buckling control.

A novel class of bioinspired materials inspired by the beak of a parrot was recently presented by Hamzehei *et al.* [10]. These materials are applied to a cylindrical meta-material and introduce contact friction, bi-stability, and interlock mechanisms at both micro- and macro-scales. As a result, the design is presented as very robust, despite the constituent materials having an elastic-plastic property. A lightweight auxetic tube was proposed by Han *et al.* [76], who optimized the original auxetic tube made of elliptical unit cells. The original auxetic tube and the novel auxetic tube were compared, and the results showed that the novel auxetic tubes had better mechanical properties than the original auxetic tubes, including higher specific energy absorption (SEA).

In addition as describe by Gomes *et al.* [28] to obtain the best performance of the auxetic tubular structures, the best way is to perform an optimization. Optimization can be described as the act of obtaining the best result under given circumstances, with the goal of optimizing the material layout inside a determined space in the project for a specific set of forces, boundary conditions, and restrictions with the goal of maximizing or minimizing the structure’s performance ([29]).

To optimize tubular auxetic structures, a great deal of research has been done on them. Where a cylindrical double-V tubular structure with auxetic behavior was designed by Gao *et al.* [30]. The authors optimized the structure’s geometry with a focus on peak crushing force and specific energy absorption. The authors observed a drop in peak crushing force of 10.3% and an increase in specific energy absorption of 39.3% as a result. It demonstrates the efficacy of the optimization process. In order to ascertain the ideal geometrical configuration, Novak *et al.* [31] developed a three-dimensional graded axisymmetric chiral auxetic structure and carried out structural optimization on one unit cell of the verified computational model. The optimized axisymmetric chiral auxetic structure offers a much stiffer mass and a more normalized mechanical response when the goal strain energy density is taken into account as the optimization objective function. This is reflected in an increased specific energy absorption of 4.25 times.

In the same way, using the multi-objective Lichtenberg algorithm based on meta modeling, Francisco *et al.* [32] constructed and optimized a sandwich composite tube with an auxetic model made of a reentrant unit cell. In two scenarios, modal performance and static performance, the writers carried out the multi-objective optimization of the model. The Poisson’s ratio, mass, and natural frequency in comparison to the original structure could all be improved by more than 56%, according to the authors’ conclusions. In terms of the static performance, the failure load, buckling load, Poisson’s ratio, and mass could all be improved. Using the cylindrical Double-v, Gao *et al.* [68] performed an optimization using the multi-objective particle swarm optimization algorithm. The authors found that

after the optimization, the energy absorption increased by nearly 2.5 times. This was the optimization's goal as well.

Recently, Francisco *et al.* [32] performed the optimizations of an auxetic tube considering different structural responses: mass, critical buckling load, natural frequency, Poisson's ratio, and maximum compression load compression. The authors used the Response Surface Methodology (RSM) to generate a metamodel with a set of non-linear equations, and the Lichtenberg algorithm proposed by Pereira *et al.* [33] was used to find the best possible configurations. The results obtained showed an improvement of up to 43% compared to the initial model. Also using RSM, Behinfar *et al.* [34] investigated the mechanical properties of auxetic stents with a tetra-star-chiral structure. They optimized the stent's elasticity parameters using both RSM and Non-dominated Sorting Genetic Algorithm (NSGA-II) methods.

The objective of this study is to conduct a comprehensive parametric analysis of a novel auxetic unit cell inspired by the intricate structures of dragonfly wings, applied within a tubular structure. By exploring variations in the design parameters of these nature-inspired auxetic unit cells, we aim to assess their influence on critical properties such as Poisson's ratio, mass, and strength. To achieve optimal structural performance, we employed response surface methodology RSM to develop a metamodel consisting of non-linear equations. This was followed by a multi-objective optimization using the NSGA-II to identify the best configurations under diverse conditions. Prototypes were then fabricated using advanced additive manufacturing techniques. To validate our findings, we conducted a combination of finite element analysis and experimental compression tests. This holistic approach ensures the robustness of our optimization process and underscores the practical feasibility and potential of our proposed designs.

### 5.1.1 RESPONSE SURFACE METHOD (RSM)

Response Surface Methodology is a common mathematical and statistical approach that investigates the responses of certain experimental configurations to identify equations that describe a process as it occurs. Equations 5.1 (first order) and 5.2 (second order) show how to identify models that represent the interest response as a function of control variables.

$$y = \beta_0 + \sum_{i=1}^k \beta_i x_i + \varepsilon \quad (5.1)$$

$$y = \beta_0 + \sum_{i=1}^k \beta_i x_i + \sum \sum \beta_{ij} x_i x_j + \sum_{i=1}^k \beta_{ij} x_i^2 + \varepsilon \quad (5.2)$$

where's the model error  $\beta$  represents the equation coefficients, while  $x = (x_1, x_2, \dots, x_k)$  is the vector of control variables. The  $\beta$  coefficients can be determined using a variety of

designs, such as the three-level factorial, box-Behnken, central composite, and Doehlert designs [154]. In this study, we will apply the central composite design (CCD). Given  $k$  as the number of controllable factors, the CCD has  $2k$  factorial points,  $2k$  axial points, and one central point. The current work comprises of  $2^3$  factorial points, 6 axial points, and 1 central point with 5 replicates. Additionally, an analysis of variance (ANOVA) will be performed to determine which components are crucial to the process and which can be deleted.

### 5.1.2 MULTI-OBJECTIVE NON-DOMINATED SORTING GA (NSGA-II)

Classical optimization approaches rely on the objective function gradient and are often solved using analytical or numerical methods. However, nonlinear and multimodal functions are frequently encountered, making the usage of these methods exceedingly complicated [29]. In this way, more sophisticated optimization techniques can serve as a viable alternative to the classical model.

Proposed by Deb [155] *et al.* in 2002, the Non-dominated Sorting GA (NSGA-II) is considered one of the most popular multi-objective algorithm. According to Ma *et al.* [156], NSGA-II computes the cost of a solution  $x$  by considering both the solutions that dominate it and the solutions that it dominates. A crowding distance is computed for each solution by calculating the distance to the nearest solutions along each objective function, and the crowding distance is then utilized to adjust each solution's fit. NSGA-II implements elitism through the  $(\lambda + \mu)$  evolution technique rather than an archive. One of the most popular Pareto-based techniques, NSGA-II's main goal is to identify a group of non-dominated people in the population. We employ a conventional NSGA-II in this study, whose overall structure is shown in Figure 5.1.

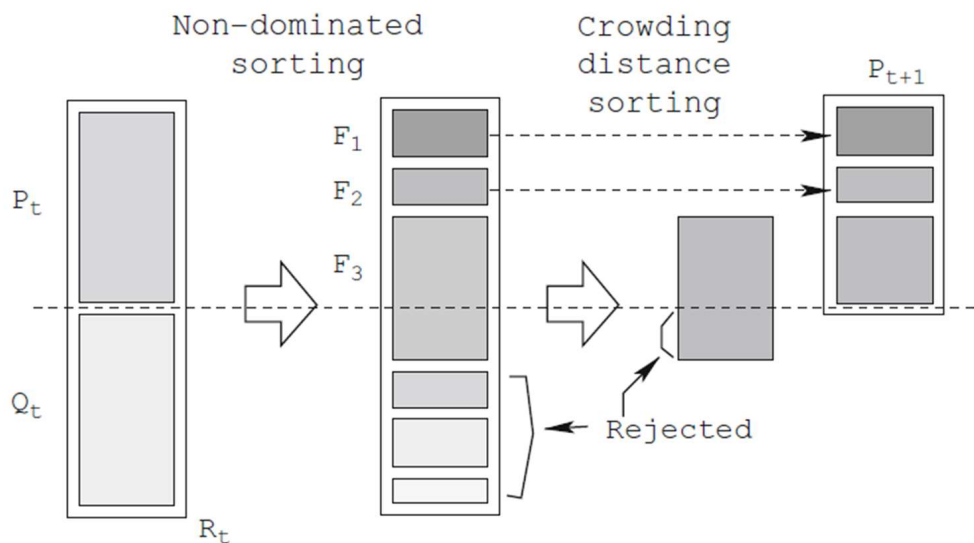


Figure 5.1 – NSGA-II algorithm structure (adapted from [155]).

Based on the comprehensive review presented by [157], the NSGA-II methodology a rigorously defined sequence of 6 procedural steps:

- Step 1: Initialize the population based on the problem range and constraint.
- Step 2: Sorting process based on non domination criteria of the population that has been initialized.
- Step 3: Once the sorting is complete, the crowding distance value is assign front wise. The individuals in population are selected based on rank and crowding distance.
- Step 4: The selection of individuals is carried out using a binary tournament selection with crowded-comparison operator .
- Step 5: Real coded GA using simulated binary crossover and polynomial mutation.
- Step 6: Offspring population and current generation population are combined and the individuals of the next generation are set by selection. The new generation is filled by each front subsequently until the population size exceeds the current population size.

In a review by Pereira *et al.* [29], where the authors compares the most useful algorithm, they found that the NSGA-II was one of the most used among others, such as MOPSO, MOGO, Jaya, and others. Being that many researchers around the world have been achieving good results where, Deng *et al.* [158] performed a multiobjective optimization for the crashworthiness design of bioinspired sinusoidal honeycombs, where the authors used the Non-dominated sorting genetic algorithm II is used to carry out the multi-objective optimization, from the optimal solution of the structure the authors found decreases by 15.52%, and the SEA increases by 6.77%. Jiang *et al.* [159], studying sandwiches structures, introduced a novel sandwich protection system aimed at mitigating close-range blast loads. The system incorporates a graded re-entrant circular auxetic core. Through multi-objective optimizations using NSGA-II, the authors sought to enhance the system's performance by comparing uniform and graded cores. The results indicate a significant improvement with the graded core sandwich panels, reducing weight by 20.0% and 33.0%, while simultaneously increasing areal specific energy absorption SEA by 21.2% and 23.1%.

From auxetic tubular structures, Behinfar *et al.* [34] investigated the mechanical properties of auxetic stents with a tetra-star-chiral structure, where the structures were optimized focused in the stent's elasticity parameters using both RSM and NSGA-II methods. The study resulted in the identification of optimal parameters for the stent, including flexural stiffness, axial elasticity modulus, radial elasticity modulus, and Poisson's ratio, which were determined as 10.66 MPa, 5.37 MPa, 33.2 MPa, and -0.41, respectively.

The multi-objective optimization algorithm NSGA-II has consistently proven its effectiveness in achieving superior results across numerous studies conducted worldwide.

In this particular study, the NSGA-II algorithm was chosen for multi-objective optimization due to its well-documented efficacy and versatility in tackling complex and diverse problems.

## 5.2 Numerical-Experimental Methodology

### 5.2.1 DFW STRUCTURE META-MODELLING THROUGH RSM

The response surface methodology was used to generate equations that reflect the two auxetic models investigated in this study. Three responses were taken into consideration.

Referring to Figure 4.2, the optimization targets three key parameters: the radius of the second circumference ( $r_2$ ), the radius of the first circumference ( $r_1$ ), and the thickness ( $t$ ) of the unit cells. However, it's imperative to note that these parameters are not entirely unconstrained. Their values must be selected carefully, as the formation of the tube depends on them, with the diameter of the tube remaining constant throughout.

To address this challenge, the current study proposes an indirect optimization approach for the parameters of the dragonfly structure. In essence, three parameters will undergo optimization, allowing for a wide range of values, from which the desired values will be determined. These parameters include the unit cell height ( $h$ ), as detailed in Equation 4.1, and the unit cell length ( $b$ ), as described in Equation 4.2. The combination of these two parameters must yield a whole number for the vertical count ( $N_v$ ), as outlined in Equation 4.4, and an even number for the horizontal count ( $N_h$ ) of unit cells, as indicated in Equation 4.5. Consequently, by employing values for the length ( $L$ ), calculated using Equation 4.4, and the diameter ( $(D_o)$ ) of the tube derived from Equation 4.7, it becomes feasible to determine the parameters listed in Table 5.1.

Table 5.1 – Lower and upper bounds for the design variables.

Variable	Lower Bound	Upper Bound	Unit
$r_1$	2	4	mm
$r_2$	3	6	mm
$t$	1	2	mm

### 5.2.2 TUBULAR META-STRUCTURE DESIGN

In this study, we have developed two different types of auxetic tubular structures using commercial CAD software. Our aim was to create a metamodel and derive non-linear equations from the response surface methodology RSM generated data. To achieve this, we designed 20 CAD models within the specified lower and upper bounds outlined in Table 5.1.

Figure 5.2 illustrates the CAD models of auxetic tubular structures constructed using the DFW unit cell model. The geometry of the DFW unit cell was customized by adjusting parameters such as radius ( $r_1$ ,  $r_2$ ) and thickness ( $t$ ), deviating from the standard specifications depicted in Figure 4.2. These adjustments were made to align with the requirements generated by the RSM. A comprehensive overview of the parameters employed in constructing the auxetic tubular structure with the DFW design is presented in Table 5.3. The tubular structure parameters were defined from a previous work, where the out diameter, the length, and the wall thickness are respectively given by 91.68 mm, 85.2 mm, and 4 mm.

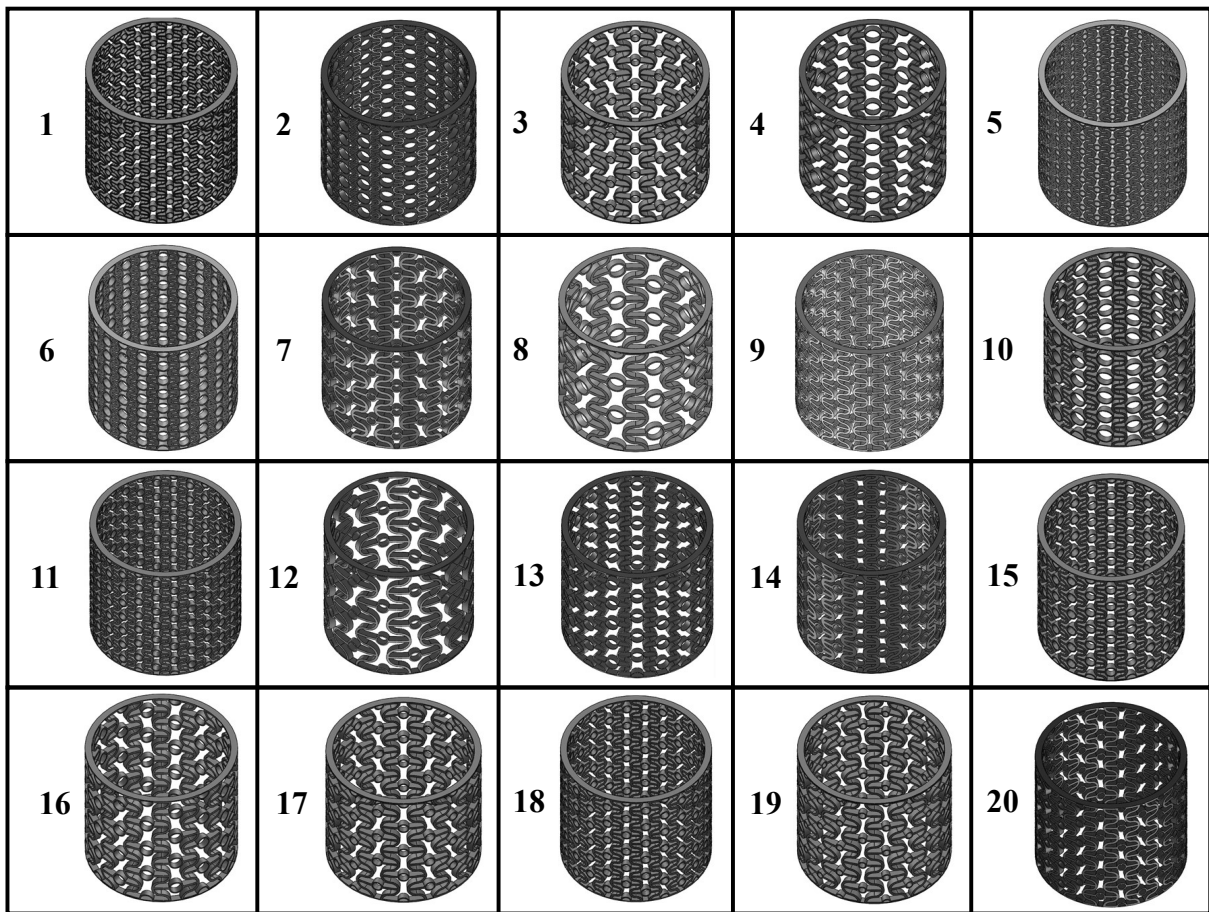


Figure 5.2 – Metal models CAD generated from the RSM data.

## 5.2.3 NUMERICAL MODEL

### 5.2.3.1 MATERIAL PROPERTIES

The chosen manufacturing process for the structure was Stereolithography (SLA), where Kafle *et al.* [160] state that photosensitive thermoset polymers are employed in SLA. Thermoset, commonly known as a thermosetting polymer, is a polymer formed by permanently polymerizing or curing a soft solid or viscous liquid prepolymer (resin). For this project, we selected a high-performance resin provided by 3D Lab, primarily for its



exceptional mechanical strength, as stated by the manufacturer. To characterize the material properties accurately, we followed the guidelines outlined in the Standard Test Method for Tensile Properties of Plastics (ASTM D638). Five specimens were manufactured under identical parameters from type I to ensure consistency, as depicted in Figure 5.3(a). These specimens, showcased in Figure 5.3(b), underwent rigorous testing, the results of which are illustrated in Figure 5.3(c). Finally, the mechanical properties are presented in the Table 5.2. By employing the same manufacturing process and parameters used for the final structure, we obtained crucial data on material behavior. These findings not only informed our numerical model but also served as inputs for the Finite Element Analysis.

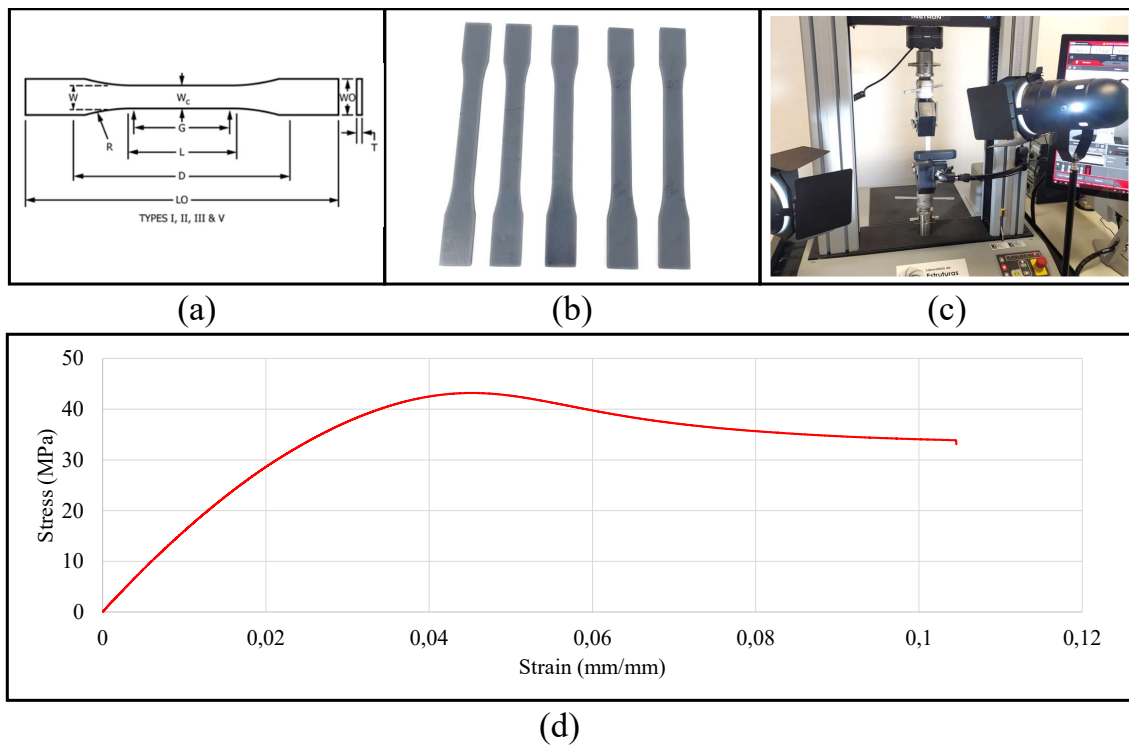


Figure 5.3 – Material Properties: (a) ASTM D638 parameters, (b) Samples, (c) Traction test, (d) Stress vs Strain curve.

Table 5.2 – Properties of high performance resin (ASTM D638).

Property	Acronyms	Mean Value	Unit
Elastic Modulus	E	1.671	GPa
Yield Stress	$\sigma_s$	37.261	MPa
Max. Stress	$\sigma_u$	44.255	MPa
Failure Stress	$\sigma_f$	34.755	MPa
Density	$\rho$	1284.229	kg/m <sup>3</sup>
Poisson's ratio	$\nu$	0.300	-

### 5.2.3.2 NUMERICAL ANALYSIS

Numerical simulations were conducted to explore the mechanical behavior of DFW unit cells within a tubular structure, where it was used to perform the analysis of the

20 models generated by the DOE and to evaluate the optimized structures. The static module provided by ANSYS Workbench was utilized to analyze the models and generate nonlinear equations. Additionally, the explicitly dynamic module was employed to assess energy absorption capabilities. To ensure thorough structural analyses, the solid tetrahedral element with second order (SOLID187) was intentionally selected as presented in the Figure 5.4(a). This element, known for its linear behavior characteristics, offers three degrees of freedom at each node, enhancing precision in evaluating deformation phenomena, particularly in complex geometrical configurations.

Finally, an analysis was conducted on the convergence of element sizes across all models, the relative error between adjacent element size was computed as the percentage difference for each individual output variables, and when the further increase in mesh density does not change the output variables by more than 5%. The meshing process commenced with an element size of 1.5 mm for all models, as depicted in Figure 5.4(b). Subsequently, mesh convergence was achieved for all models by using the number of elements as a reference, as illustrated in Figure 5.4(c).

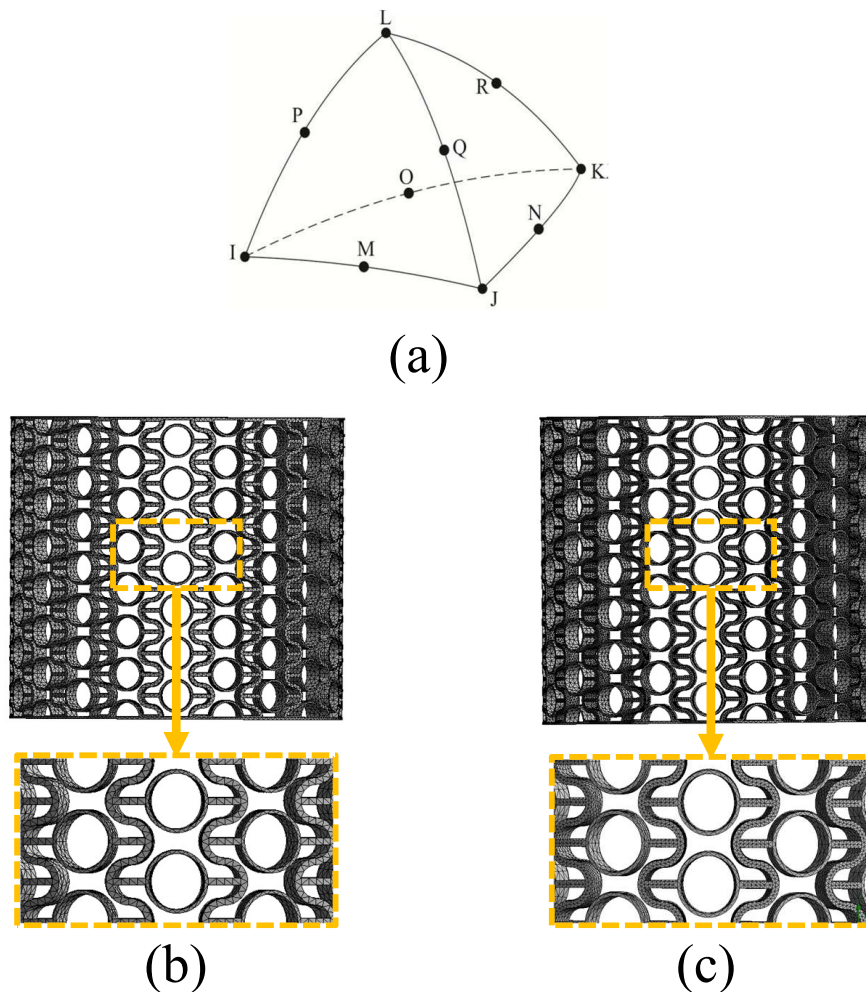


Figure 5.4 – Finite Element Method: (a) SOLID 187, (b) Auxetic tubular structure meshes without convergence, (c) Auxetic tubular structure meshes with convergence.

## 5.2.4 MULTI-OBJECTIVE PROBLEM STATEMENT

It is necessary to optimize two or more different goals in the multi-objective optimization problem. Stated differently, achieving one goal might lead to the decrease of other goals. As a result, it is typically not possible to simultaneously attain the ideal value of every sub-objective. Designers must compromise between many sub-objectives and perform multi-objective comparisons.

Evaluating Poisson's ratio as one of the pivotal parameters in auxetic structures, it serves as a parameter for achieving their characteristic NPR. Additionally, stress management within the structure is paramount. A key attribute of the innovative design proposed the DFW is its proactive approach to addressing stress concentration an inherent vulnerability in traditional structures by skillfully enhancing the configuration's deformability. Ultimately, the importance of optimizing structures lies in attaining the best mechanical properties while minimizing mass. For that reason from the Equation 5.3, present the objectives of this work, where is to minimize three key parameters Poisson's ratio  $\nu$ ,  $\sigma$ , and  $m$ , respectively in order to achieve optimal performance.

$$\text{Find } \mathbf{X} = \{r_1; r_2; t\}$$

That minimizes:

$$\begin{cases} \mathcal{F}_1(\mathbf{X}) = \text{mass (g)}, \\ \mathcal{F}_2(\mathbf{X}) = \text{Poisson (-)}, \\ \mathcal{F}_3(\mathbf{X}) = \text{stress (MPa)}, \end{cases}$$

subject to:

$$\begin{aligned} g_1(\mathbf{X}) : N_v &= \frac{L - 2e}{h} \equiv 0 \\ g_2(\mathbf{X}) : N_h &= \frac{2B}{b + x + t} \equiv 0 \pmod{2} \end{aligned}$$

$$\{2.0; 3.0; 1.0\} \leq \mathbf{X} \leq \{4.0; 6.0; 2.0\}$$

(5.3)

## 5.2.5 EXPERIMENTAL VALIDATION

### 5.2.5.1 SAMPLES MANUFACTURING

To achieve the best quality in the final structure, the auxetic tubular structures were manufactured via SLA additive manufacturing using a resin printer CREALITY LD-006, where the material used was the high performance resin from 3D lab. The structures were designed in CAD software and posteriorly imported into the CHITUBOX<sup>®</sup> software, where all the configurations for printing were done.

Figure 5.5 (a) presents the manufacturing process of the auxetic tubular structures, and the finished structure of the baseline represented by Figure 5.5 (b) while the optimized structure, distinguished by black paint, is shown in Figures 5.5 (c) and (d).

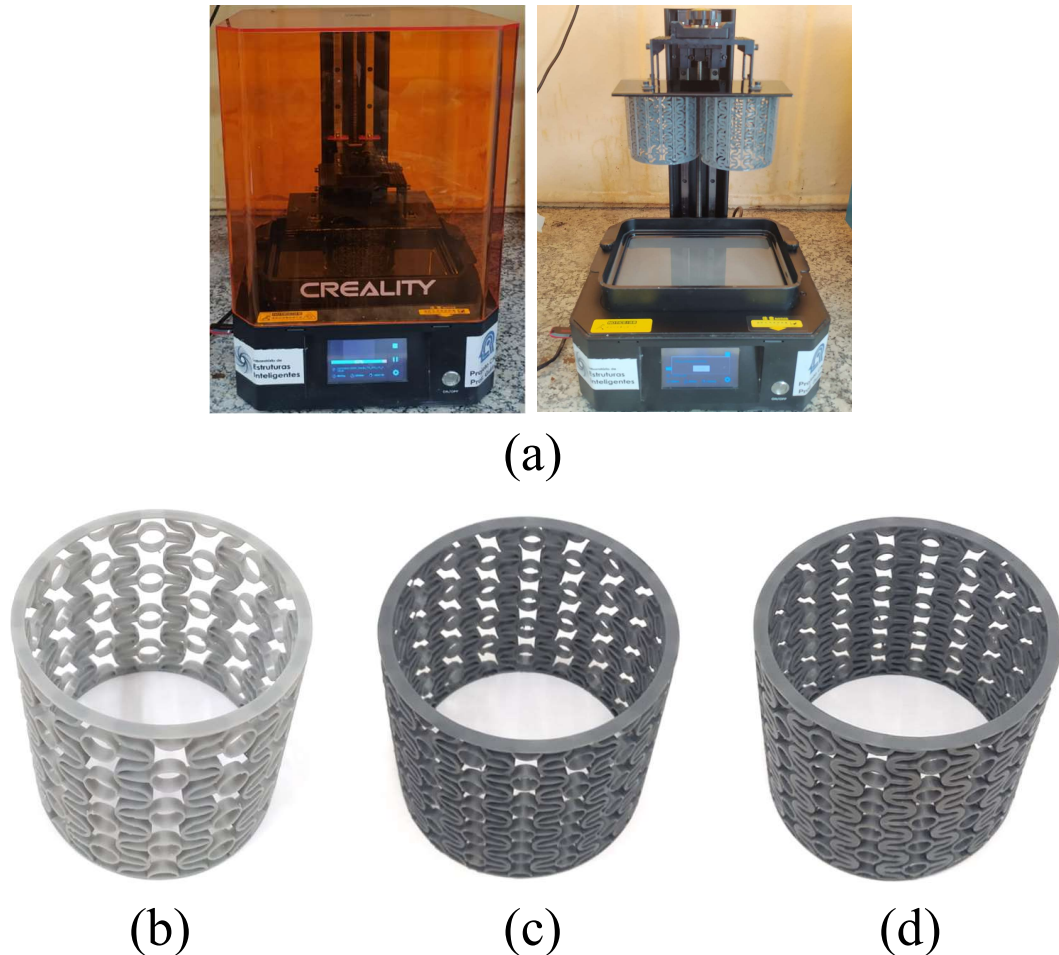


Figure 5.5 – Manufacture Process: (a) Printing process, (b) BaseLine, (c) TOPSIS 1 and (d) TOPSIS 2.

#### 5.2.5.2 QUASI-STATIC COMPRESSIVE TEST

The Figure 5.6 (a), presents the compressive test performed on all the specimens being the baseline and the Optimized structure to study the deformation mode, load displacement curves, and energy absorption capacity of the auxetic tubular structures. The compressive axial load was applied to the upper extremities at a constant speed of 2 mm/min, the tests were carried out using a universal testing machine, the Instron 34TM-10 equipped with a 10 kN load cell and controlled by Instron's own software, and a Longitech camera integrated into the machine itself was also used to record the experimental test. Finally, Figure 5.6 (b), (c) and (d) shows respectively the manufactured auxetic tubular structures samples obtained for each configuration during the compression test. All the experimental steps were conducted in the Smart Structures Laboratory at Universidade Federal de Itajubá.

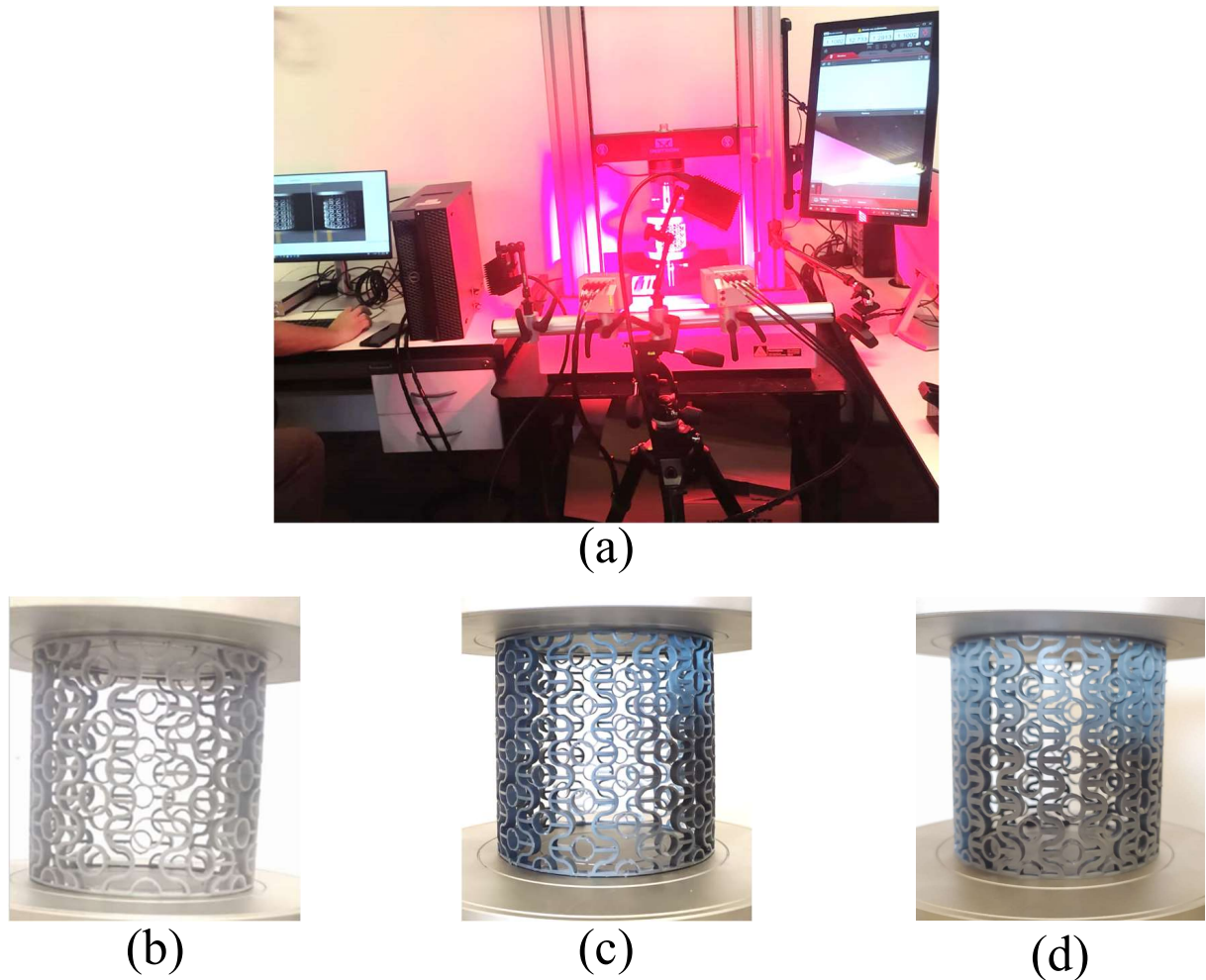


Figure 5.6 – Quasi-static compression test setup: (b) BaseLine, (c) TOPSIS 1 and (d) TOPSIS 2.

## 5.3 RESULTS AND DISCUSSION

### 5.3.1 RSM ANALYSIS

To obtain the three desired responses, a set of experiments were designed using a response surface methodology. All replies will be collected via numerical simulation. It will be possible to identify three metamodels that will be used as an objective function in structural optimization. Table 5.3 displays the experimental design and results. Figure 5.7 displays the Pareto's chart for each response, indicating which factors are statistically significant and which are not for each studied response.

Table 5.3 – Design of experiments and responses of a DFW auxetic tubular structure.

Exp.	Design variables			Responses		
	$r_1$ (mm)	$r_2$ (mm)	$t$ (mm)	$\mathcal{F}_1 = \text{Mass (g)}$	$\mathcal{F}_2 = \nu (-)$	$\mathcal{F}_3 = \text{Stress (MPa)}$
1	2.143	3.000	1.000	36.940	-0.436	17.691
2	4.200	3.000	1.000	31.210	-0.294	24.235
3	2.750	5.250	1.000	23.500	-0.570	50.395
4	5.036	5.250	1.000	20.630	-0.383	61.840
5	1.800	3.000	2.000	72.070	-0.412	4.724
6	3.545	3.000	2.000	61.550	-0.277	6.205
7	2.750	5.250	2.000	44.410	-0.504	13.956
8	5.000	7.000	2.000	31.950	-0.422	29.441
9	1.339	4.200	1.500	45.460	-0.625	13.852
10	4.800	4.200	1.500	35.060	-0.318	21.262
11	2.539	3.000	1.500	51.410	-0.373	8.983
12	3.286	7.000	1.500	26.690	-0.577	40.657
13	3.800	4.200	0.659	17.610	-0.419	87.629
14	3.000	4.200	2.341	59.020	-0.392	7.594
15	3.045	3.500	1.500	44.330	-0.363	12.785
16	3.750	5.250	1.500	31.950	-0.446	26.878
17	2.750	5.250	1.500	34.060	-0.534	48.947
18	2.500	3.500	1.500	46.390	-0.421	11.534
19	1.950	5.250	1.500	36.180	-0.622	22.355
20	2.345	4.200	1.500	41.320	-0.497	15.991

Figure 5.7 displays the Pareto chart, facilitating the analysis of statistically significant factors for each response studied. Notably, in compression analysis, all factors are significant for mass and Poisson ratio, while radius  $r_1$  shows insignificance for stress.

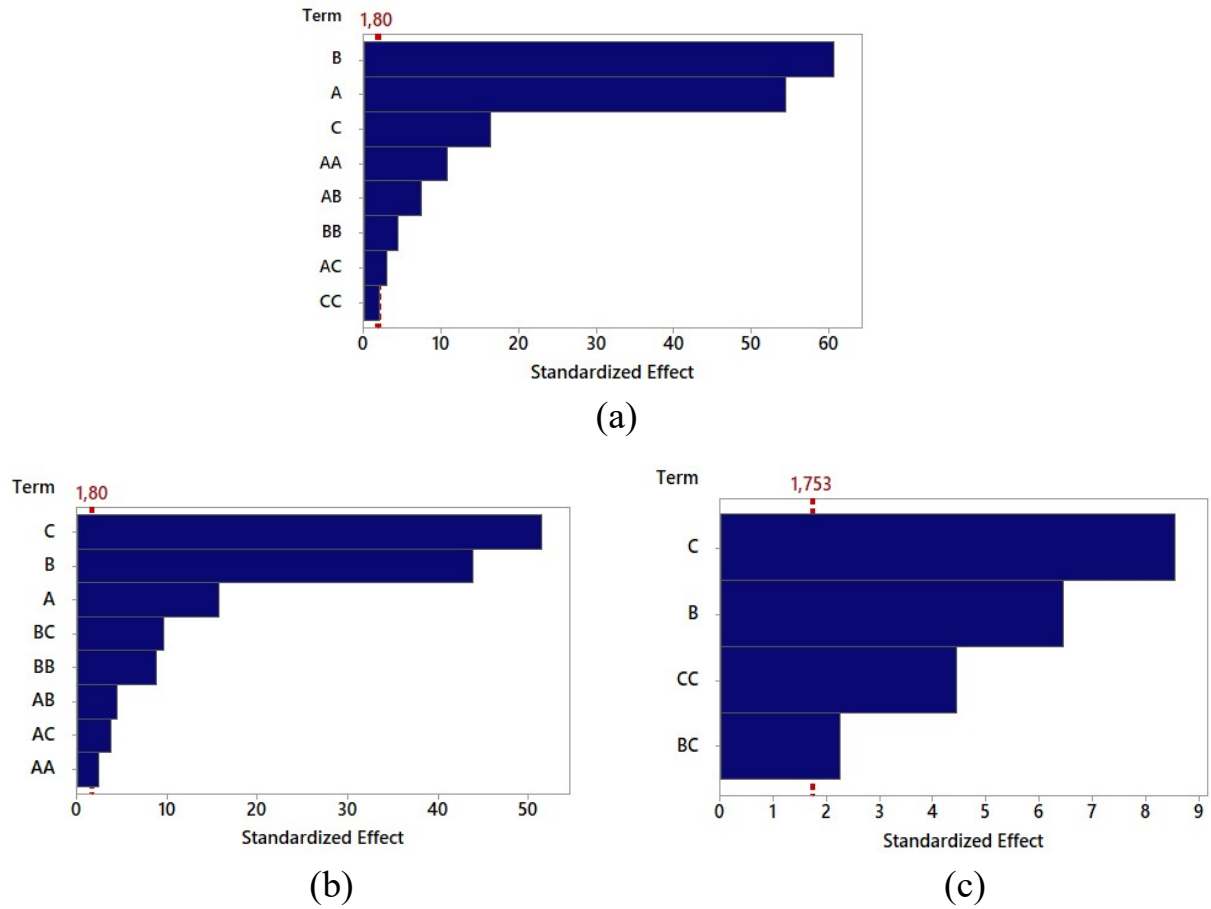


Figure 5.7 – Pareto Chart: (a) Poisson, (b) Mass, (c) Stress. (Legend: A:  $r_1$ , B:  $r_2$  and C:  $t$ ).

Table 5.4 – Regression coefficients with corresponding P-Values.

Response	$r_1$	$r_2$	$t$	$r_1^2$	$r_2^2$	$t^2$	$r_1 \times r_2$	$r_1 \times t$	$r_2 \times t$
Mass (g)	0.000	0.000	0.000	0.033	0.000	-	0.001	0.003	0.000
Poisson (-)	0.000	0.000	0.000	0.000	0.001	0.074	0.000	0.000	-
Stress (MPa)	-	0.000	0.000	-	-	0.000	-	-	0.039

Figure 5.8 presents the main effects of parameters in the RSM analysis. In the Poisson analysis depicted in Figure 5.8 (a), the radius sizes ( $r_1$  and  $r_2$ ) exhibit the most significance. Notably, the minimum NPR occurs when  $r_1$  is minimized and  $r_2$  is maximized; thickness  $t$  has a lesser impact on the Poisson analysis. In Figure 5.8 (b), analyzing mass, all parameters are significant. The lowest mass is achieved with maximum  $r_1$  and minimum  $r_2$ , while thickness plays a crucial role, with greater thickness leading to increased structure weight.

From the stress analysis illustrated in Figure 5.8 (c), aligned with the Pareto chart in Figure 5.7 (c), it's evident that radius  $r_1$  isn't statistically significant for compression analysis. Conversely, radius  $r_2$  demonstrates significant impact on stress, with smaller  $r_2$  sizes correlating with lower stress levels. Moreover, as expected, increasing thickness leads to reduced stress levels in the structure.

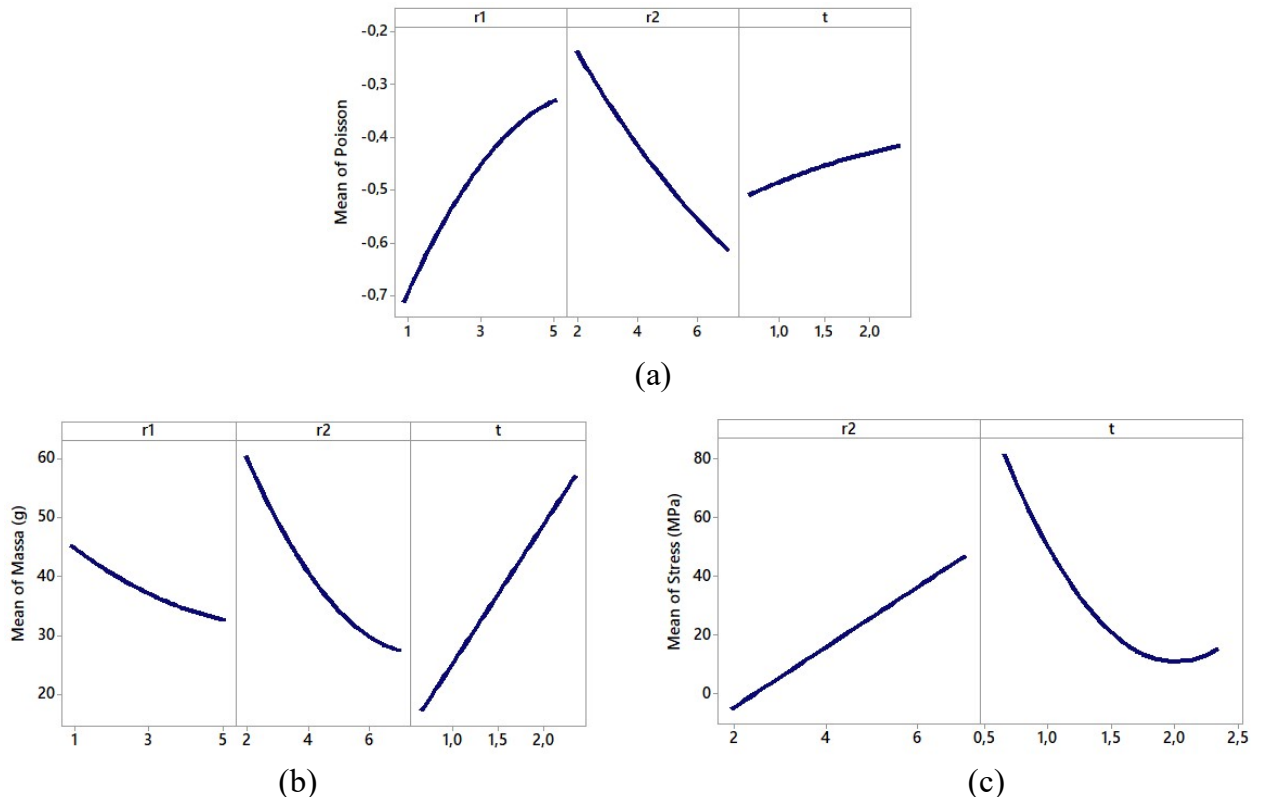


Figure 5.8 – Main Effect Chart: (a) Poisson, (b) Mass, (c) Stress.

Additionally, Figure 5.9 illustrates the surface plot of the analyzed responses, revealing intricate non-linear patterns. The robustness of the RSM methodology is evident in its successful quantification and understanding of these complex physical-structural relationships.



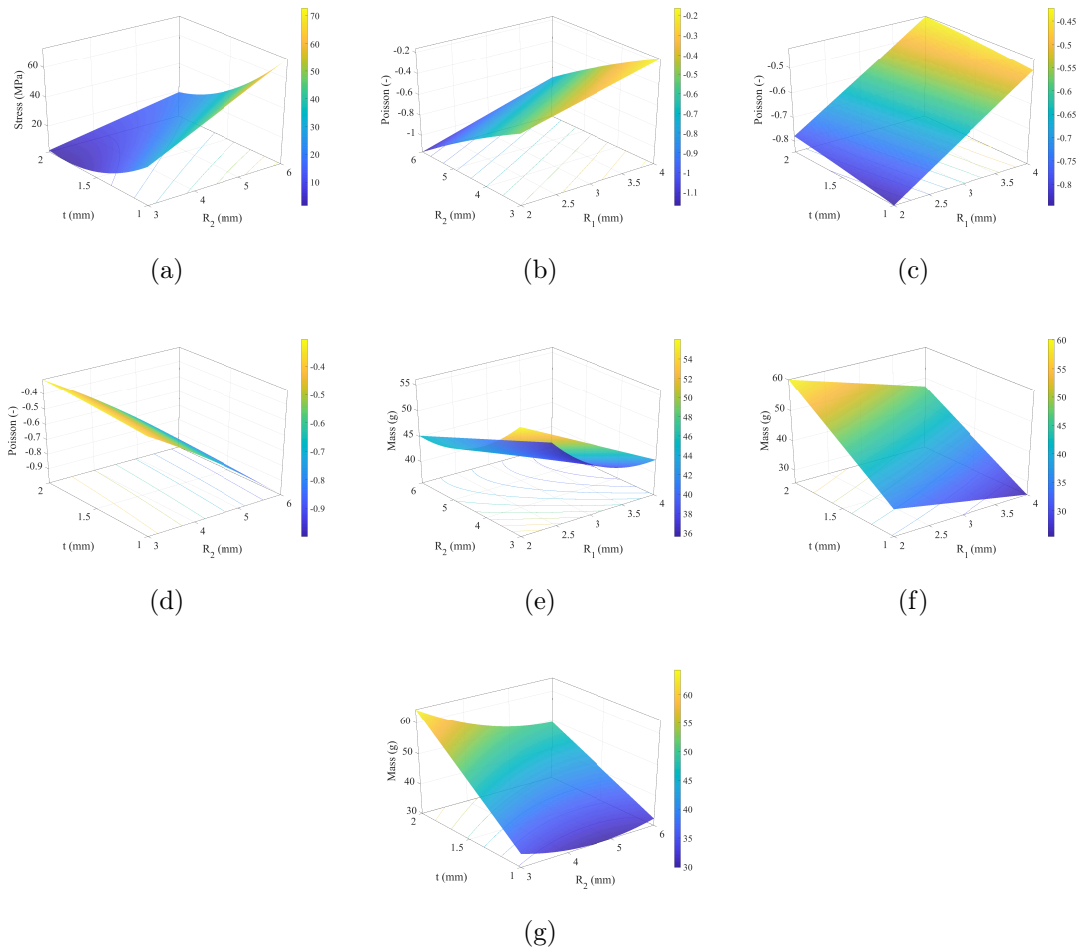


Figure 5.9 – Experimental responses plotted by pairs around the center point in one variable.

Following thorough analysis, the adequacy of the models to the data was assessed, as depicted in Table 5.5. In accordance with Montgomery’s established criterion, adjustments surpassing 80% are regarded as satisfactory, indicating the reliability of the models for practical use. It’s worth noting that Standart Deviation  $Sd$ , providing additional context for the evaluation.

Table 5.5 – Model Summary Table for fit regression model.

Response	Sd	$R^2_{adjusted}$
Mass (g)	0.687	99.760%
Poisson ratio (-)	0.006	99.700%
Stress (MPa)	8.176	88.590%

Finally, the objective of utilizing the response surface methodology RSM was to derive equations for the responses  $\mathcal{F}_1$ ,  $\mathcal{F}_2$ , and  $\mathcal{F}_3$  represented by Equations 5.4, 5.6, and 5.5 respectively. These equations were formulated to reflect the auxetic models investigated

in this study, aiming to facilitate optimization. The ensuing results will be expounded upon in the subsequent section.

$$\begin{aligned} \mathcal{F}_1 = \text{Mass (g)} = & 38.50 - 6.12r_1 - 11.95r_2 + 48.32t + 0.408r_1^2 + 1.042r_2^2 \\ & + 0.792r_1r_2 - 1.951r_1t - 4.192r_2t \end{aligned} \quad (5.4)$$

$$\begin{aligned} \mathcal{F}_2 = \text{Poisson (-)} = & -0.4531 + 0.14875r_1 - 0.14758r_2 + 0.1294t - 0.01529r_1^2 \\ & + 0.004312r_2^2 - 0.01313t^2 + 0.01150r_1r_2 - 0.01153r_1t \end{aligned} \quad (5.5)$$

$$\mathcal{F}_3 = \text{Stress (MPa)} = 55.6 + 24.44r_2 - 111.2t + 38.25t^2 - 9.46r_2t \quad (5.6)$$

### 5.3.2 MULTI OBJECTIVE DESIGN OPTIMIZATION

According to the optimization goals, the non-dominated sorting genetic algorithm NSGA-II is used to carry out multi-objective optimization of DFW applied in a tubular structure under quasi-static compression forces. The Pareto front depicted in Figure 5.10 represents the set of non-dominated solutions achievable by the metamodel. Each point along this front signifies an optimal outcome with respect to multiple conflicting objectives. Selection among these points is contingent upon the specific requirements and priorities of the designer.

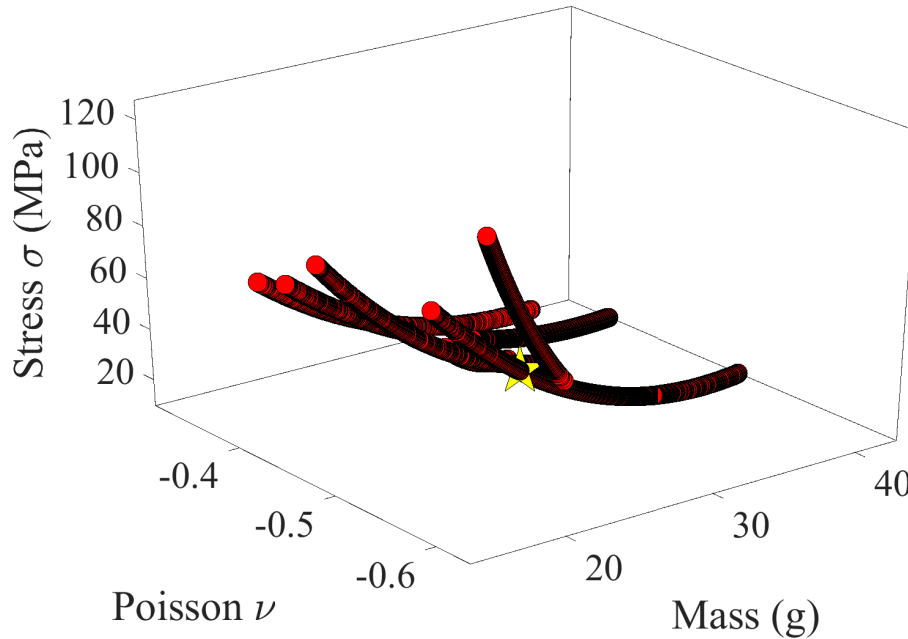


Figure 5.10 – Pareto Surface (◦ non-dominated solutions and ★ Topsis solution).

It is recognized that enhancing all three responses simultaneously is infeasible, given the inherent trade-offs; for instance, reducing stress levels may lead to an increase in mass.

Improving one objective, represented by the Nadir points necessitates a compromise on another. In this study, the TOPSIS decision criterion was employed to select an optimal solution. This criterion identifies the point farthest from the worst outcome while being closest to the best outcome. The selected point is denoted by a star in the Figure 5.10.

Table 5.6 illustrates the Nadir points derived from the analysis, delineating Nadir 1 as the target for minimizing mass, Nadir 2 for minimizing Poisson ratio, and Nadir 3 for minimizing stress. These metrics are compared against a baseline for comparative evaluation. Figure 5.11 present the geometric disparities between the structures at their respective Nadir points and the baseline, providing a visual representation of their comparative parameters.

Table 5.6 – Nadir solutions of the Pareto surface.

Response	Design variables			Objective function		
	$r_1$ (mm)	$r_2$ (mm)	$t$ (mm)	$\mathcal{F}_1 = \text{Mass (g)}$	$\mathcal{F}_2 = \text{Poisson (-)}$	$\mathcal{F}_3 = \text{Stress (MPa)}$
Nadir 1 (min. mass)	3.750	5.250	0.659	26.193	-0.394	42.666
Nadir 2 (min. Poisson)	3.287	7.000	1.193	15.383	-0.489	94.497
Nadir 3 (min. Stress)	3.800	4.200	2.000	47.939	-0.351	9.351

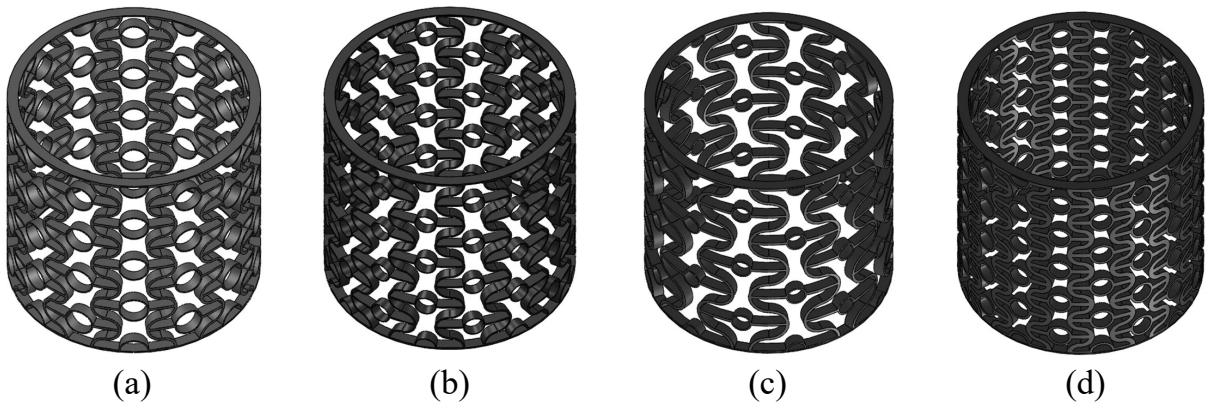


Figure 5.11 – Auxetic tubular structures: (a) Baseline, (b) Nadir 1, (c) Nadir 2, (d) Nadir 3.

The optimal point, designated as TOPSIS 1 and marked with a star in Figure 5.10, was determined using a criterion that evenly distributes a weight of 33.3% across each response variable. Additionally, to explore further insights, a second TOPSIS approach, referred to as TOPSIS 2, was introduced. In TOPSIS 2, the criterion assigns 0% weight to mass and 50% weight to each of the response variables, Poisson ratio and stress. Table 5.7 presents the outcomes obtained from the multi-objective optimization process for both TOPSIS 1 and TOPSIS 2. The optimized structures are presented in the Figure 5.12

Table 5.7 – TOPSIS solutions of the Pareto surface.

Response	Design variables			Objective function		
	$r_1$ (mm)	$r_2$ (mm)	$t$ (mm)	$\mathcal{F}_1 = \text{Mass (g)}$	$\mathcal{F}_2 = \text{Poisson (-)}$	$\mathcal{F}_3 = \text{Stress (MPa)}$
TOPSIS 1 ( $w = [13 \ 13 \ 13]$ )	3.800	4.200	1.040	26.193	-0.394	42.665
TOPSIS 2 ( $w = [0 \ 12 \ 12]$ )	3.800	4.200	1.877	45.712	-0.354	9.703

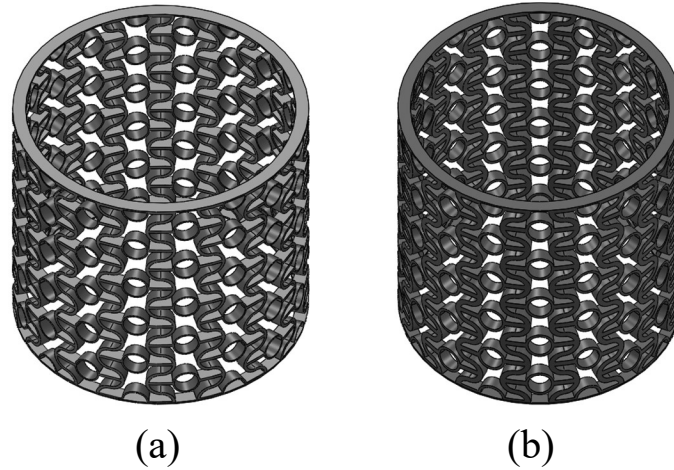


Figure 5.12 – Optimized Structures: (a) TOPSIS 1, (b) TOPSIS 2.

To rigorously validate these findings, a series of finite element simulations were carried out, as depicted in Figure 5.13. These simulations presented a comprehensive comparison between the optimized structural configurations from both TOPSIS 1 and TOPSIS 2 methodologies against the baseline configuration which geometry dimensions are respectively presented in the Table 5.8. The ensuing analysis, detailed in Table 5.7, compare the results obtained through the NSGA-II algorithm with the results acquired via finite element analysis. Notably, the comparison present reduction in variance between the NSGA-II to FEA, affirming the robustness of the optimization process.

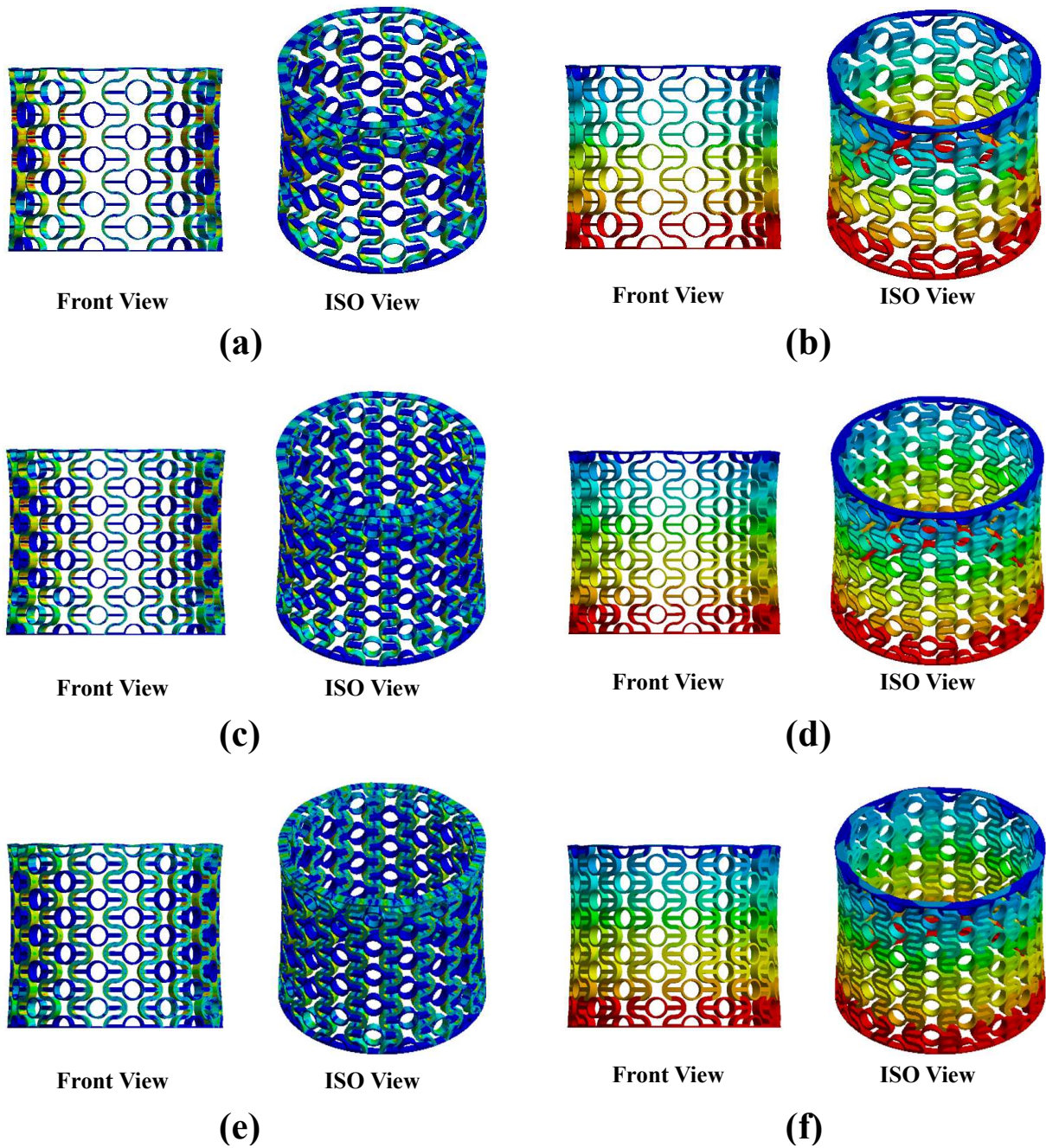


Figure 5.13 – Finite Element Analysis: (a) Stress of the baseline, (b) Displacement of the baseline, (c) Stress of the Topsis 1, (d) Displacement of the Topsis 1, (e) Stress of the Topsis 2, (f) Displacement of the Topsis 2.

Table 5.8 – Parameters of the auxetic DFW tubular structure.

Variable	Symbol	Unit	Baseline	TOPSIS 1 Parameters	TOPSIS 2 Parameters
Radius length 1	$r_1$	mm	5.04	4.20	4.20
Radius length 2	$r_2$	mm	5.25	3.80	3.80
Center distance	x	mm	9.07	6.56	5.72
Horizontal length	b	mm	31.07	24.40	24.40
Thickness	t	mm	1.00	1.04	1.87
Height of unit cell	h	mm	21	16.80	16.80
Length of tube	L	mm	85.20	85.20	85.20
Perimeter of the tube	B	mm	288	288	288
Outer diameter of the tube	$D_o$	mm	91.68	91.68	91.68
Thickness of tube	T	mm	4.00	4.00	4.00
Edge thickness of tube	e	mm	0.60	0.60	0.60
Number of horizontal cell	$N_h$	-	14	18	18
Number of vertical cell	$N_v$	-	4	5	5
3D model mass	m	g	20.63	26.19	45.68

Table 5.9 – Comparing Optimized Model to Finite Element Analysis (FEA).

Response	TOPSIS 1 ( $w = [13 \ 13 \ 13]$ )			TOPSIS 2 ( $w = [0 \ 12 \ 12]$ )		
	NSGA II	FEM	Diff. (%)	NSGA II	FEM	Diff. (%)
Mass (g)	26.193	26.480	1%	45.712	45.590	0%
Poisson	-0.394	-0.396	1%	-0.354	-0.355	0%
Stress (MPa)	42.665	36.970	13%	9.073	10.336	7%

From the finite element analysis performed in the structures optimized also the baseline structure as presented in Figure 5.13, where the difference between of the TOPSIS 1 and TOPSIS 2 compared to the baseline are presented in the Table 5.10.

Table 5.10 – Comparison of Baseline FEM values to TOPSIS 1 and TOPSIS 2.

Response	Analysis 1			Analysis 2		
	BaseLine	TOPSIS 1	Diff. (%)	BaseLine	TOPSIS 2	Diff. (%)
$\mathcal{F}_1 = \text{Mass (g)}$	20.630	26.193	-27%	20.630	45.712	-122%
$\mathcal{F}_2 = \text{Poisson}$	-0.383	-0.394	3%	-0.383	-0.354	-8%
$\mathcal{F}_3 = \text{Stress (MPa)}$	61.840	42.665	45%	61.840	9.703	537%

By examining Table 5.10, it is evident that pursuing mass reduction as an objective inherently increases stress levels, which was anticipated. The initial comparison of TOPSIS 1 shows a 27% increase in mass from the baseline, along with a 3% decrease in the Poisson ratio. Despite the mass increase, the optimized structure achieved a 45% reduction in stress. In the subsequent analysis of TOPSIS 2, mass was disregarded as an objective, resulting in a 122% increase in mass and an 8% increase in the Poisson ratio. Notably, this considerable mass increase led to a significant 537% decrease in stress.

Analyzing the results from TOPSIS 1 further, it is clear that all responses improved after the optimization, except for the mass, which increased by 27%. This increase, although significant, remains acceptable given the overall enhancements observed. For TOPSIS 2, the results are noteworthy, with all responses showing improvement. Specifically, the 122% increase in mass resulted in a remarkable 537% reduction in stress levels. Additionally, the analysis highlights the presence of multiple optimal locations (presented in Figure 5.10), suggesting the potential to identify further ideal points with even lower mass and higher Poisson levels if required.

### 5.3.3 QUASI-STATIC COMPRESSION: TEST RESULTS AND ANALYSIS

To enhance the robustness of the approach, numerical static models laid the foundation for constructing the meta model and initiating the optimization process. Recognizing the inherent complexity and non-linearity of the structure's behavior, dynamic explicit simulations were then strategically introduced within the experimental framework. This integration enabled a comprehensive prediction of the structure's dynamic response, ensuring a more accurate and reliable assessment.

Through compressive analysis, the avenue for experimental validation is widened, allowing for a thorough examination of additional critical parameters within the realm of non-linear behavior. Although this work does not aim to optimize the structure specifically to increase energy absorption capability, from the compression experimental test it is still possible to analyze this highly attractive characteristic of auxetic structures. Furthermore, from the compressive analysis facilitates the exploration of another fundamental characteristic of auxetic structures is possible to analyse the Poisson coefficient.

In the evaluation of the energy absorption (EA) capabilities of the inner tube during axial crushing or compression tests, we utilize Equation 3.1 for mathematical calculation. To determine the Specific Energy Absorption (SEA), we propose expressing the energy absorption (EA) relative to mass ( $M$ ), as demonstrated in Equation 3.2. Additionally, we introduce the characterization of energy absorption per load displacement  $d$ , allowing for the computation of the predominant crushing force (MCF) for the NPR structure, as detailed in Equation 3.3.

After the experimental compression tests were completed, data on force-displacement relationships and properties such as EA, SEA, and MCF were directly obtained using equations 3.1, 3.2, and 3.3. The results of the compression tests for auxetic tubular structures are depicted in Figure 5.14, illustrating the force per displacement. A comparison among different unit cells, including the baseline, TOPSIS 1, and TOPSIS 2, reveals varying behaviors during compression testing. Notably, the TOPSIS 2 structure demonstrates the highest load resistance, while TOPSIS 1 exhibits greater resistance to displacement.

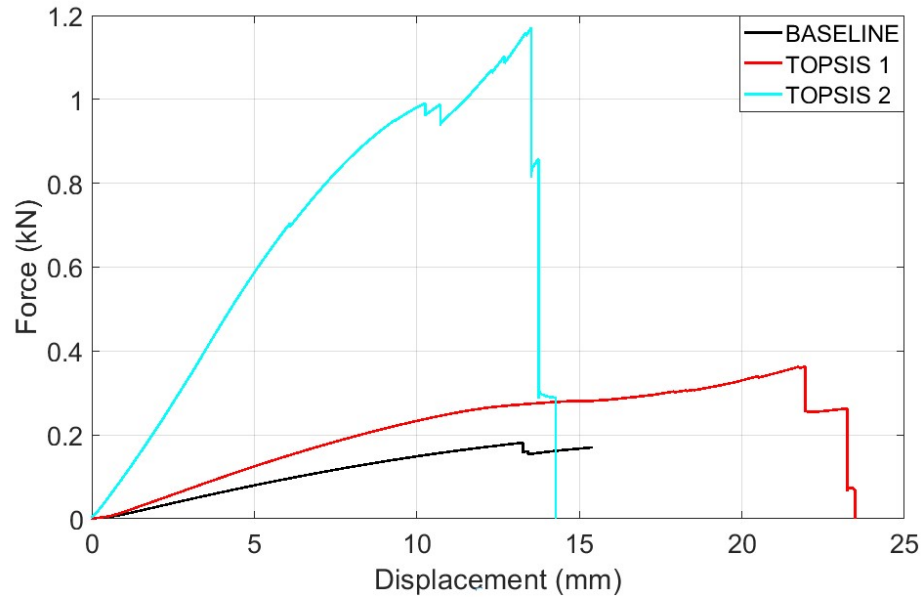


Figure 5.14 – Compression results for the auxetic tubular structures: Baseline, TOPSIS 1 and TOPSIS2.

The results of energy absorption by the manufactured structures, illustrated in Figure 5.15 and calculated using Equation 3.1, reveal a clear trend. Comparing the energy absorption ability of the structures, it is possible to note that the TOPSIS 2 structure demonstrates superior performance compared to both the TOPSIS 1 and baseline structures, as anticipated due to its inherent robustness. This observation highlights that, although the optimization process did not specifically aim to enhance energy absorption capabilities, the optimized structures nonetheless outperformed the baseline structure.

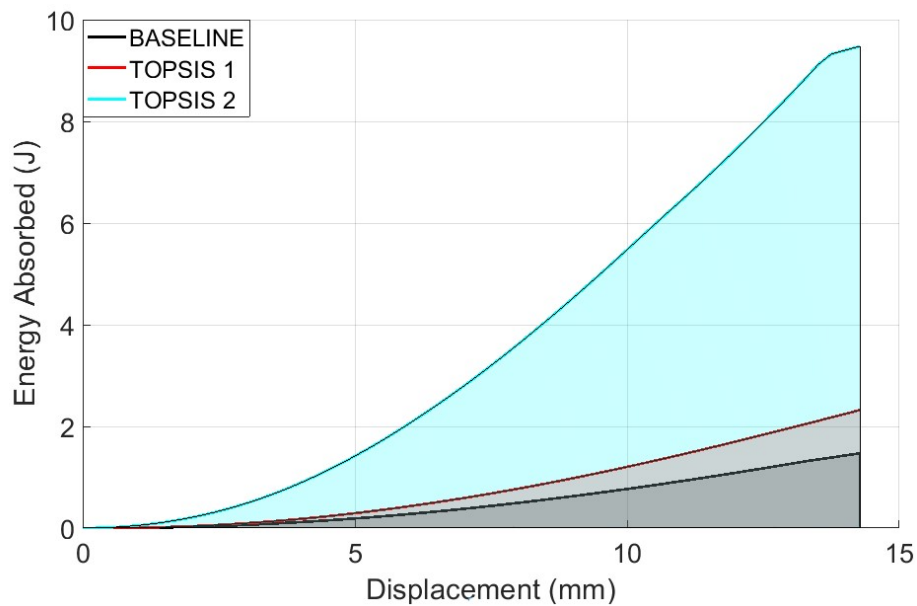


Figure 5.15 – Energy absorption of Baseline, TOPSIS 1 and TOPSIS 2.

Equally significant, Figure 5.16 illustrates the specific energy absorption SEA per unit mass for all auxetic models. Upon scrutiny of the graph, several key observations



emerge. Notably, when comparing TOPSIS 1 to the baseline, a substantial reduction in mass is evident. However, the disparity in specific energy absorption ability achieved between the two configurations is relatively minor.

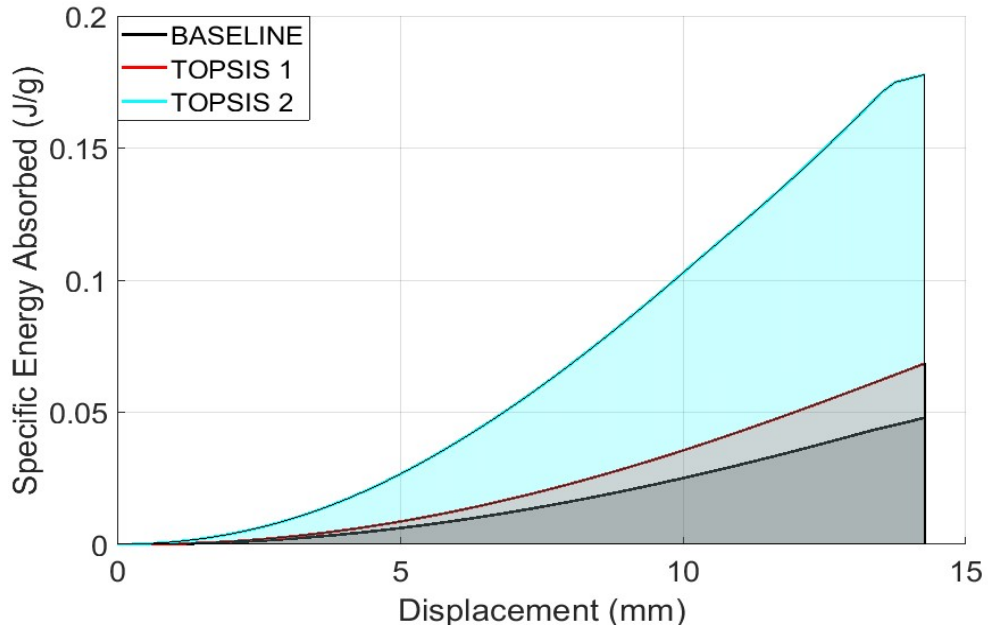


Figure 5.16 – Specific Energy Absorption of Baseline, TOPSIS 1 and TOPSIS 2.

Table 5.11 presents a comprehensive categorization of the results obtained from the analysis of force-displacement signals for the structures under examination, organized into sets of three structures optimized through TOPSIS 1 and TOPSIS 2 methodologies. This categorization allows for a detailed comparison and evaluation of the performance of each optimization approach. Additionally, Figure 5.17 displays the properties visually.

Table 5.11 – Comparison of Baseline FEM values to TOPSIS 1 and TOPSIS 2.

Response	Analysis 1			Analysis 2		
	Baseline	TOPSIS 1	Diff. (%)	Baseline	TOPSIS 2	Diff. (%)
Mass (g)	30.690	33.900	10%	30.690	53.30	74%
Disp. (mm)	18.200	23.460	29%	18.200	14.210	-22%
Force (N)	188.000	363.200	93%	188.000	1170.800	523%
EA (J)	1.470	2.320	58%	1.470	9.480	545%
SEA (J/g)	0.048	0.069	43%	0.048	0.118	146%
MCF (N)	0.081	0.099	22%	0.081	0.667	726%
$\bar{\rho}$ (%)	10.70	13.99	31%	10.70	25.28	136%

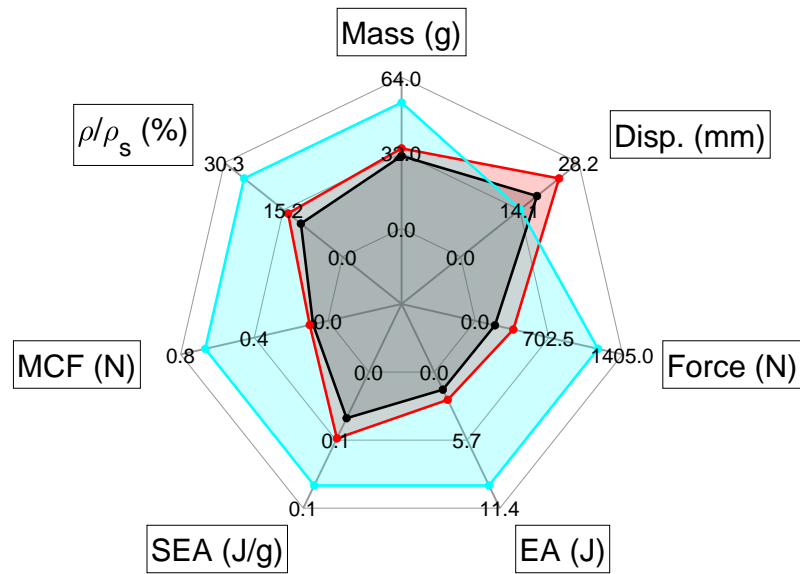


Figure 5.17 – Graphical visualization of structure properties (legend: — Baseline, — Topsis 1, — Topsis 2).

From the analysis of Table 5.11, several significant observations emerge regarding the disparities between the baseline structure and the optimized configurations, underscoring the primary objective of this study, which did not prioritize energy absorption optimization. Notably, the optimization objectives of Topsis 1 and 2 yielded substantial increase in mass compared to the baseline, amounting to 10% and 74%, respectively.

Regarding structural performance, Topsis 1 exhibited superior resistance to displacement, surpassing the baseline and Topsis 2 by 29% and 39%, respectively. Despite its lighter mass, Topsis 2 demonstrated commendable force resistance, achieving levels 523% more than the baseline structure.

Due to the robustness the Topsis 2 structure displayed superior energy absorption capability compared to the optimized configuration Topsis 1 being able to absorb 309% more energy, also compared to the baseline absorbed 545% more energy. Also the Topsis 1 were able to absorb 58% more energy to the baseline. Notably, when comparing specific energy absorption, despite a mass increasing of 21% for Topsis 1 and 90% for Topsis 2, the differences were 43% and 143%, respectively, compared to the baseline. These findings underscore the trade-offs between mass reduction and energy absorption efficiency in structural optimization endeavors.

To predict the behavior of the structures, an analysis using the explicitly dynamic finite element method (FEM) was performed. Figure 5.18 illustrates the deformation characteristics of the Baseline, Topsis 1, and Topsis 2 structures, facilitating a com-

parative analysis between the experimental findings and the finite element deformation models. The precision of the numerical analyses is evident in the alignment of the results, attesting to the accuracy of the simulations. Furthermore, the validation of the finite element model enhances the overall reliability of the study.

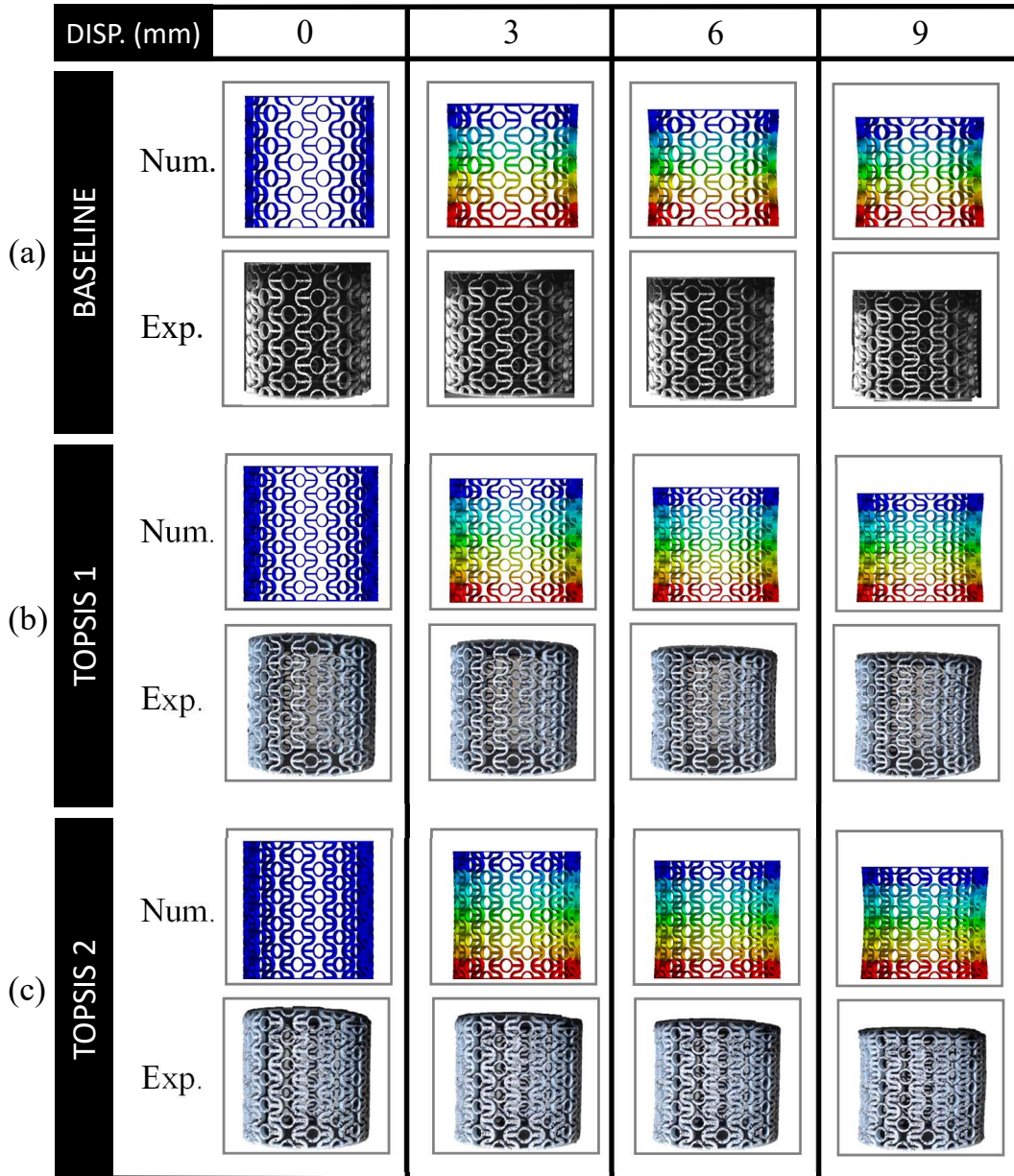


Figure 5.18 – Displacement Explicitly Dynamic Finite Element Analysis: (a) Baseline, (b) TOPSIS 1, (c) TOPSIS 2.

In conclusion, the dynamic explicit analysis results presented in Figure 5.19 demonstrate the Poisson's ratio outcomes for the three auxetic structures. As anticipated, the findings are consistent with the theoretical expectations. Specifically, the mean Poisson's ratio values observed were around of -0.40 for TOPSIS 1, Baseline, and TOPSIS 2, as detailed in Table 5.10. Furthermore, it is noteworthy that the variation in Poisson's ratio across the different displacement levels was minimal, suggesting stable auxetic behavior

for all structures under dynamic loading conditions.

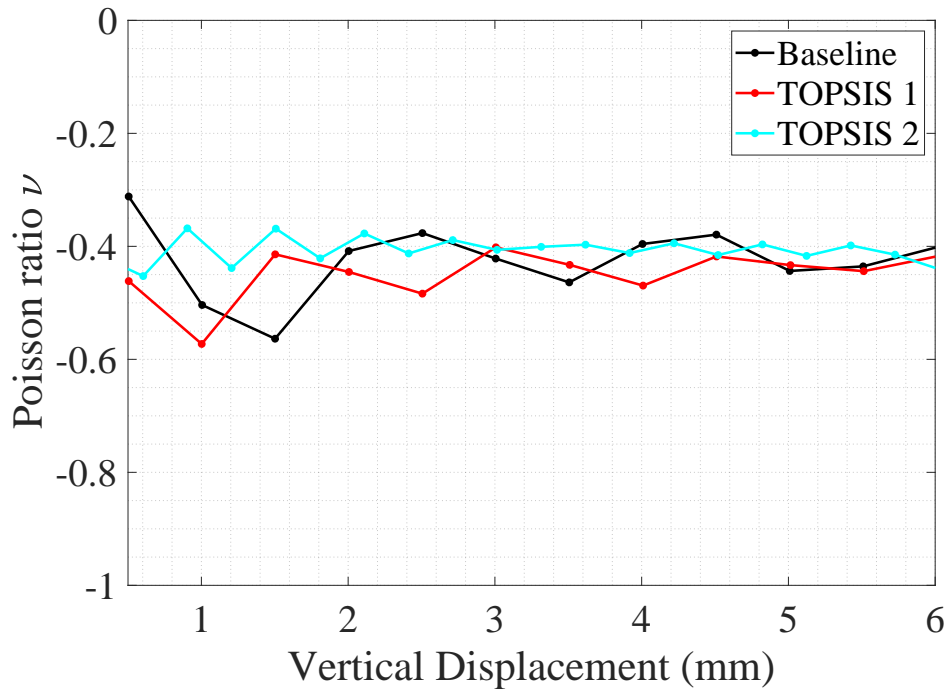


Figure 5.19 – Numerical Poisson ratio result.

## 5.4 CHAPTER CONCLUSION

The models developed using RSM demonstrated high accuracy and reliability, as the optimization results were closely aligned with those obtained from finite element analysis. With adjusted  $R^2$  values exceeding 80% for all models, this robustness was a crucial factor supporting the continuation of the work.

The numerical model was validated with experimental data, yielding robust and reliable results. The RSM methodology demonstrated excellent adaptability to the data, ensuring the generation of reliable outputs for each proposed configuration. The finite element method (FEM) was particularly important in this project, enabling numerous low-cost experiments and providing a detailed understanding of structural behaviors under various conditions. This significantly contributed to the accuracy and effectiveness of the simulations. The combination of these methodological approaches reinforced the validity of the results and the reliability of the model, solidifying its applicability for future research and development.

The NSGA-II algorithm successfully identified optimal points that demonstrated high reliability, as the results generated by the algorithm were in close agreement with those produced by the finite element model.

The results obtained in this work demonstrate the critical importance of optimization analysis in achieving more efficient structural designs. In terms of compression performance, the TOPSIS 1 structure, when compared to the baseline, showed a significant reduction in Stress and Poisson's ratio by 45% and 3%, respectively. Additionally, comparing the TOPSIS 2 structure to the baseline resulted in an impressive 537% reduction in Stress. These findings underscore the effectiveness of the optimization techniques employed and highlight their potential for enhancing structural performance.

Although the optimization process did not involve energy absorption characteristics, the compression experimental tests under quasi-static load allowed for the evaluation of certain auxetic properties. The energy absorbed by the TOPSIS 1 and TOPSIS 2 structures increased by 58% and 545%, respectively, compared to the baseline. Additionally, the maximum resistance force of TOPSIS 1 and TOPSIS 2 increased by 93% and 523%, respectively, when compared to the baseline. These results highlight the significant improvements in auxetic properties achieved through the optimization process.

In conclusion, the optimized auxetic structures demonstrated outstanding performance and versatility, making them highly suitable for applications in mechanical engineering, naval architecture, aerospace, and the automotive industries. These structures offer numerous advantages and opportunities for further development, with the potential to become ubiquitous in everyday applications. As research progresses, their widespread adoption is anticipated, promising transformative impacts across various fields and paving the way for innovative solutions in engineering and design.

## 6 FINAL REMARKS

Auxetic tubular structures have emerged as a recent subject of heightened research interest. Compared to conventional solid tubular structures, they offer numerous attractive advantages, including superior energy absorption capabilities, enhanced bending performance, resistance to twist deformation, exceptional ability to expand under traction force, and reduced weight. Given their outstanding mechanical properties and unique behavior, as discussed and illustrated in preceding sections, auxetic tubular structures have garnered significant attention for applications across diverse fields, ranging from automotive and medical to civil engineering and aerospace.

After conducting a review of auxetic structures, an improved auxetic unit cell inspired by nature was developed. Taking inspiration from the shape of dragonfly wings and aiming to reduce stress concentrations using curved shapes, a unit cell was designed and parameterized. Additionally, the effects of the relationship between the radii, referred to as  $\lambda$ , on the relative density of the structure were evaluated.

The unit cell was then applied to a tubular structure and compared to classical Reentrant unit cells. The two developed structures (DFW-A and DFW-B) exhibited distinct pros and cons. DFW-A, inspired by a higher number of unit cells, demonstrated superior mechanical properties such as energy absorption, specific energy absorption, and main crushing force compared to DFW-B, which was designed with the same weight. However, due to its geometry, DFW-B exhibited reduced stress concentrations. For future work, it is recommended to validate the performance based solely on the quantity of unit cells.

Experimental tests revealed that the novel unit cells exhibited superior mechanical properties. The DFW-A configuration demonstrated an impressive 163% increase in energy absorption compared to the classical reentrant, while the DFW-B configuration showed a substantial 79% enhancement. The alignment of results from numerical analysis further validated the accuracy of the simulations, allowing for the evaluation of Poisson's ratios. DFW-A and DFW-B exhibited Poisson's ratios of -0.5 and -0.3, respectively, while the reentrant structure had a Poisson's ratio of -1.3. Additionally, stress concentration was evaluated, revealing that when the structures were deformed by 12 mm along the y-axis, DFW-A and DFW-B experienced 65% and 118% lower stress, respectively, compared to the conventional reentrant structure.

Subsequently, an optimization process was conducted using a metamodel with Response Surface Methodology (RSM), which proved to be highly accurate and reliable. The optimization results closely aligned with those obtained from finite element analysis (FEA), indicating the robustness of the methodology. With adjusted  $R^2$  values exceeding 80% for all models, this level of precision was pivotal in supporting the continuation of the research. The numerical model underwent validation using experimental data, resulting

in robust and reliable outcomes. The Response Surface Methodology (RSM) exhibited exceptional adaptability to the data, ensuring the generation of reliable outputs for each proposed configuration. The Finite Element Method (FEM) played a pivotal role in this project, facilitating numerous cost-effective experiments and providing comprehensive insights into structural behaviors under diverse conditions. This significantly enhanced the accuracy and efficacy of the simulations. The integration of these methodological approaches bolstered the validity of the results and the reliability of the model, affirming its applicability for future research and development endeavors. Moreover, the NSGA-II algorithm successfully identified optimal points with high reliability, as evidenced by the close agreement between the algorithm-generated results and those produced by the finite element model.

The findings from the optimization process emphasize the crucial role of optimization analysis in developing more efficient structural designs. Concerning compression performance, the TOPSIS 1 structure showed a notable decrease in stress and Poisson's ratio by 45% and 3%, respectively, compared to the initial model. Similarly, the TOPSIS 2 structure exhibited a remarkable 537% reduction in stress relative to the baseline. These results underscore the efficacy of the optimization techniques employed and demonstrate their potential to enhance structural performance. Although the optimization process did not directly address energy absorption characteristics, the compression experimental tests under quasi-static load facilitated the evaluation of specific auxetic properties. The energy absorbed by the TOPSIS 1 and TOPSIS 2 structures increased by 58% and 545%, respectively, compared to the initial model. Additionally, the maximum resistance force of TOPSIS 1 and TOPSIS 2 increased by 93% and 523%, respectively, compared to the baseline. These outcomes highlight the significant advancements in auxetic properties achieved through the optimization process.

In conclusion, the present study introduces an improved, nature-inspired novel unit cell applied in tubular structures, which demonstrated outstanding performance and versatility. These structures are highly suitable for applications in mechanical engineering, naval architecture, aerospace, and the automotive industries. They offer numerous advantages and opportunities for further development, with the potential to become ubiquitous in everyday applications. As research progresses, their widespread adoption is anticipated, promising transformative impacts across various fields and paving the way for innovative solutions in engineering and design.

Finally, suggestions for future research can be drawn from this master dissertation as a continuation, such as analyzing the structure under different conditions like torsion and bending, applying the unit cell concept to other structures such as beams, and finally, performing optimization to enhance the energy absorption ability.

# BIBLIOGRAPHY

- [1] Roderic Lakes. “Foam structures with a negative Poisson’s ratio”. In: *Science* 235.4792 (1987), pp. 1038–1040.
- [2] Kenneth E Evans and Andrew Alderson. “Auxetic materials: functional materials and structures from lateral thinking!” In: *Advanced materials* 12.9 (2000), pp. 617–628.
- [3] Mariam Mir et al. “Review of mechanics and applications of auxetic structures”. In: *Advances in Materials Science and Engineering 2014* (2014).
- [4] Matheus Brendon Francisco et al. “A review on the energy absorption response and structural applications of auxetic structures”. In: *Mechanics of Advanced Materials and Structures* 29.27 (2022), pp. 5823–5842.
- [5] Ariosto B. Jorge et al. “Fundamental Concepts and Models for the Direct Problem”. In: UnB, 2022. Chap. Auxetic Structures: Parametric Optimization, Additive Manufacturing, and Applications.
- [6] Xiang Yu Zhang et al. “A novel type of tubular structure with auxeticity both in radial direction and wall thickness”. In: *Thin-Walled Structures* 163 (2021), p. 107758.
- [7] David T Farrell, Conor McGinn, and Gareth J Bennett. “Extension twist deformation response of an auxetic cylindrical structure inspired by deformed cell ligaments”. In: *Composite Structures* 238 (2020), p. 111901.
- [8] Hui Wang et al. “A novel two-dimensional mechanical metamaterial with negative Poisson’s ratio”. In: *Computational Materials Science* 171 (2020), p. 109232.
- [9] Ramin Hamzehei et al. “3D-printed bio-inspired zero Poisson’s ratio graded metamaterials with high energy absorption performance”. In: *Smart Materials and Structures* 31.3 (2022), p. 035001.
- [10] Ramin Hamzehei et al. “Parrot Beak-Inspired Metamaterials with Friction and Interlocking Mechanisms 3D/4D Printed in Micro and Macro Scales for Supreme Energy Absorption/Dissipation”. In: *Advanced Engineering Materials* ().
- [11] Shu Yang et al. “A comparative study of ballistic resistance of sandwich panels with aluminum foam and auxetic honeycomb cores”. In: *Advances in Mechanical Engineering* 5 (2013), p. 589216.
- [12] F Scarpa, LG Ciffo, and JR Yates. “Dynamic properties of high structural integrity auxetic open cell foam”. In: *Smart Materials and Structures* 13.1 (2003), p. 49.



- [13] F Scarpa et al. “Mechanical properties of auxetic tubular truss-like structures”. In: *physica status solidi (b)* 245.3 (2008), pp. 584–590.
- [14] RS Lakes and K Elms. “Indentability of conventional and negative Poisson’s ratio foams”. In: *Journal of Composite Materials* 27.12 (1993), pp. 1193–1202.
- [15] Guoxing Lu and TX Yu. *Energy absorption of structures and materials*. Elsevier, 2003.
- [16] Milad Oloumi Doudaran, Hamed Ahmadi, and GholamHossein Liaghat. “Crushing performance of auxetic tubes under quasi-static and impact loading”. In: *Journal of the Brazilian Society of Mechanical Sciences and Engineering* 44.6 (2022), pp. 1–24.
- [17] Kai Yang et al. “Design of dimpled tubular structures for energy absorption”. In: *Thin-Walled Structures* 112 (2017), pp. 31–40.
- [18] Wei Huang et al. “Hierarchical structure and compressive deformation mechanisms of bighorn sheep (*Ovis canadensis*) horn”. In: *Acta biomaterialia* 64 (2017), pp. 1–14.
- [19] Jie Fu et al. “Design of bionic-bamboo thin-walled structures for energy absorption”. In: *Thin-Walled Structures* 135 (2019), pp. 400–413.
- [20] Abdallah Ghazlan et al. “Performance of a 3D printed cellular structure inspired by bone”. In: *Thin-Walled Structures* 151 (2020), p. 106713.
- [21] Astha Khanna, Maedeh Zamani, and Ngan F Huang. “Extracellular matrix-based biomaterials for cardiovascular tissue engineering”. In: *Journal of cardiovascular development and disease* 8.11 (2021), p. 137.
- [22] Guan Zhou et al. “Design optimization of a novel NPR crash box based on multi-objective genetic algorithm”. In: *Structural and Multidisciplinary Optimization* 54.3 (2016), pp. 673–684.
- [23] Yuanlong Wang et al. “A negative Poisson’s ratio suspension jounce bumper”. In: *Materials & Design* 103 (2016), pp. 90–99.
- [24] Kaori Kuribayashi et al. “Self-deployable origami stent grafts as a biomedical application of Ni-rich TiNi shape memory alloy foil”. In: *Materials Science and Engineering: A* 419.1-2 (2006), pp. 131–137.
- [25] Murtaza N Ali and Ihtesham Ur Rehman. “An Auxetic structure configured as oesophageal stent with potential to be used for palliative treatment of oesophageal cancer; development and in vitro mechanical analysis”. In: *Journal of Materials Science: Materials in Medicine* 22.11 (2011), pp. 2573–2581.

- [26] Zainab Munib et al. “Auxetic polymeric bone stent for tubular fractures: design, fabrication and structural analysis”. In: *Polymer-Plastics Technology and Engineering* 54.16 (2015), pp. 1667–1678.
- [27] Gaetano Burriesci and Giovanni Bergamasco. *Annuloplasty prosthesis with an auxetic structure*. US Patent 8,034,103. Oct. 2011.
- [28] Rafael Augusto Gomes et al. “Tubular auxetic structures: A review”. In: *Thin-Walled Structures* 188 (2023), p. 110850.
- [29] João Luiz Junho Pereira et al. “A review of multi-objective optimization: methods and algorithms in mechanical engineering problems”. In: *Archives of Computational Methods in Engineering* 29.4 (2022), pp. 2285–2308.
- [30] Qiang Gao et al. “Multi-objective crashworthiness optimization for an auxetic cylindrical structure under axial impact loading”. In: *Materials & design* 143 (2018), pp. 120–130.
- [31] Nejc Novak et al. “Structural Optimization of the Novel 3D Graded Axisymmetric Chiral Auxetic Structure”. In: *physica status solidi (b)* (2022), p. 2200409.
- [32] Matheus Brendon Francisco et al. “Design optimization of a sandwich composite tube with auxetic core using multiobjective lichtenberg algorithm based on meta-modelling”. In: *Engineering Structures* 281 (2023), p. 115775.
- [33] João Luiz Junho Pereira et al. “Lichtenberg algorithm: A novel hybrid physics-based meta-heuristic for global optimization”. In: *Expert Systems with Applications* 170 (2021), p. 114522.
- [34] Parsa Behinfar and Amir Nourani. “Analytical and numerical solution and multi-objective optimization of tetra-star-chiral auxetic stents”. In: *Discover Applied Sciences* 6.2 (2024), p. 39.
- [35] Michael L May. “Heat exchange and endothermy in protodonata”. In: *Evolution* (1982), pp. 1051–1058.
- [36] SR Jongerius and D Lentink. “Structural analysis of a dragonfly wing”. In: *Experimental Mechanics* 50 (2010), pp. 1323–1334.
- [37] Hamed Rajabi et al. “A comparative study of the effects of constructional elements on the mechanical behaviour of dragonfly wings”. In: *Applied Physics A* 122 (2016), pp. 1–13.
- [38] MARK REAVIS and MARVIN LUTTGES. “Aerodynamic forces produced by a dragonfly”. In: *26th Aerospace Sciences Meeting*. 1988, p. 330.

- [39] Nina Gaissert et al. “Inventing a micro aerial vehicle inspired by the mechanics of dragonfly flight”. In: *Towards Autonomous Robotic Systems: 14th Annual Conference, TAROS 2013, Oxford, UK, August 28–30, 2013, Revised Selected Papers 14*. Springer. 2014, pp. 90–100.
- [40] JM Wakeling and CP Ellington. “Dragonfly flight: III. Lift and power requirements”. In: *Journal of experimental biology* 200.3 (1997), pp. 583–600.
- [41] Christopher Dileo and Xinyan Deng. “Design of and experiments on a dragonfly-inspired robot”. In: *Advanced Robotics* 23.7-8 (2009), pp. 1003–1021.
- [42] Bing Xu et al. “Making negative Poisson’s ratio microstructures by soft lithography”. In: *Advanced materials* 11.14 (1999), pp. 1186–1189.
- [43] Liu Yanping and Hu Hong. “A review on auxetic structures and polymeric materials”. In: *Scientific Research and Essays* 5.10 (2010), pp. 1052–1063.
- [44] Kusum Meena and Sarat Singamneni. “A new auxetic structure with significantly reduced stress concentration effects”. In: *Materials & Design* 173 (2019), p. 107779.
- [45] PS Theocaris, GE Stavroulakis, and PD Panagiotopoulos. “Negative Poisson’s ratios in composites with star-shaped inclusions: a numerical homogenization approach”. In: *Archive of Applied Mechanics* 67.4 (1997), pp. 274–286.
- [46] Joseph N Grima and Kenneth E Evans. “Auxetic behavior from rotating squares”. In: (2000).
- [47] Ulrik Darling Larsen, O Signund, and S Bouwsta. “Design and fabrication of compliant micromechanisms and structures with negative Poisson’s ratio”. In: *Journal of microelectromechanical systems* 6.2 (1997), pp. 99–106.
- [48] Neil Gaspar et al. “Novel honeycombs with auxetic behaviour”. In: *Acta Materialia* 53.8 (2005), pp. 2439–2445.
- [49] Joseph N Grima et al. “Auxetic perforated mechanical metamaterials with randomly oriented cuts”. In: *Advanced materials* 28.2 (2016), pp. 385–389.
- [50] Xin Ren et al. “Mechanical properties of foam-filled auxetic circular tubes: Experimental and numerical study”. In: *Thin-Walled Structures* 170 (2022), p. 108584.
- [51] H Cho, D Seo, and DN Kim. “Mechanics of auxetic materials”. In: *Handbook of mechanics of materials* (2019), pp. 733–757.
- [52] D Prall and RS Lakes. “Properties of a chiral honeycomb with a Poisson’s ratio of  $-1$ ”. In: *International Journal of Mechanical Sciences* 39.3 (1997), pp. 305–314.
- [53] Chris W Smith, JN Grima, and KenE Evans. “A novel mechanism for generating auxetic behaviour in reticulated foams: missing rib foam model”. In: *Acta materialia* 48.17 (2000), pp. 4349–4356.

- [54] Katia Bertoldi et al. “Negative Poisson’s ratio behavior induced by an elastic instability”. In: *Advanced materials* 22.3 (2010), pp. 361–366.
- [55] ZiWen Zhang et al. “A novel butterfly-shaped auxetic structure with negative Poisson’s ratio and enhanced stiffness”. In: *Journal of Materials Science* 56.25 (2021), pp. 14139–14156.
- [56] Aniket Ingrole, Ayoun Hao, and Richard Liang. “Design and modeling of auxetic and hybrid honeycomb structures for in-plane property enhancement”. In: *Materials & Design* 117 (2017), pp. 72–83.
- [57] Mengchuan Xu et al. “Mechanical properties and energy absorption capability of AuxHex structure under in-plane compression: Theoretical and experimental studies”. In: *International Journal of Mechanical Sciences* 159 (2019), pp. 43–57.
- [58] Yingli Li and Gengwang Yan. “Vibration characteristics of innovative reentrant-chiral elastic metamaterials”. In: *European Journal of Mechanics-A/Solids* 90 (2021), p. 104350.
- [59] Wenjiao Zhang et al. “In-plane mechanical behavior of novel auxetic hybrid metamaterials”. In: *Thin-Walled Structures* 159 (2021), p. 107191.
- [60] Kusum Meena and Sarat Singamneni. “Novel hybrid auxetic structures for improved in-plane mechanical properties via additive manufacturing”. In: *Mechanics of Materials* 158 (2021), p. 103890.
- [61] Xiao Li Ruan et al. “Mechanical design of antichiral-reentrant hybrid intravascular stent”. In: *International Journal of Applied Mechanics* 10.10 (2018), p. 1850105.
- [62] Meng-Fu Guo, Hang Yang, and Li Ma. “Design and characterization of 3D AuxHex lattice structures”. In: *International Journal of Mechanical Sciences* 181 (2020), p. 105700.
- [63] Jin Woo Lee et al. “A tubular biomaterial construct exhibiting a negative Poisson’s ratio”. In: *PLoS One* 11.5 (2016), e0155681.
- [64] Murtaza Najabat Ali, James JC Busfield, and Ihtesham U Rehman. “Auxetic oesophageal stents: structure and mechanical properties”. In: *Journal of Materials Science: Materials in Medicine* 25.2 (2014), pp. 527–553.
- [65] Wenwang Wu et al. “Mechanical properties of hierarchical anti-tetrachiral metastructures”. In: *Extreme Mechanics Letters* 16 (2017), pp. 18–32.
- [66] Wenwang Wu et al. “Mechanical properties of anti-tetrachiral auxetic stents”. In: *Composite Structures* 185 (2018), pp. 381–392.
- [67] Yuanlong Wang et al. “Parametric analysis of a cylindrical negative Poisson’s ratio structure”. In: *Smart Materials and Structures* 25.3 (2016), p. 035038.

- [68] Qiang Gao et al. “Crashworthiness optimization of cylindrical negative Poisson’s ratio structures with inner liner tubes”. In: *Structural and Multidisciplinary Optimization* 64.6 (2021), pp. 4271–4286.
- [69] Chong Zhang et al. “Tunable compressive properties of a novel auxetic tubular material with low stress level”. In: *Thin-Walled Structures* 164 (2021), p. 107882.
- [70] Wenjiao Zhang et al. “Mechanics of novel asymmetrical re-entrant metamaterials and metastructures”. In: *Composite Structures* 291 (2022), p. 115604.
- [71] Chen Luo et al. “Design, manufacturing and applications of auxetic tubular structures: A review”. In: *Thin-Walled Structures* 163 (2021), p. 107682.
- [72] Xin Ren et al. “Numerical investigation of tubular structures generated by cutting method and pattern scale factor (PSF) method”. In: *Pigment & Resin Technology* (2019).
- [73] Dong Han et al. “Mechanical characterization of a novel thickness gradient auxetic tubular structure under inclined load”. In: *Engineering Structures* 273 (2022), p. 115079.
- [74] Bin Ling et al. “Design and analysis for large magnitudes of programmable Poisson’s ratio in a series of lightweight cylindrical metastructures”. In: *International Journal of Mechanical Sciences* 195 (2021), p. 106220.
- [75] Ali Zolfagharian et al. “3D-printed programmable mechanical metamaterials for vibration isolation and buckling control”. In: *Sustainability* 14.11 (2022), p. 6831.
- [76] Dong Han et al. “Lightweight auxetic tubular metamaterials: Design and mechanical characteristics”. In: *Composite Structures* 311 (2023), p. 116849.
- [77] Robert V Goldstein et al. “Negative Poisson’s ratio for six-constant tetragonal nano/microtubes”. In: *physica status solidi (b)* 252.7 (2015), pp. 1580–1586.
- [78] R Goldstein et al. “Mechanical characteristics for seven-constant rhombohedral crystals and their nano/microtubes”. In: *Letters on materials* 6.2 (2016), pp. 93–97.
- [79] Robert V Goldstein, Valentin A Gorodtsov, and Dmitry S Lisovenko. “Chiral elasticity of nano/microtubes from hexagonal crystals”. In: *Acta Mechanica* 229.5 (2018), pp. 2189–2201.
- [80] Yong Tao Yao, Andrew Alderson, and Kim Lesley Alderson. “Can nanotubes display auxetic behaviour?” In: *physica status solidi (b)* 245.11 (2008), pp. 2373–2382.
- [81] F Scarpa, S Adhikari, and CY Wang. “Nanocomposites with auxetic nanotubes”. In: *International Journal of Smart and Nano Materials* 1.2 (2010), pp. 83–94.
- [82] Ruben Gatt et al. “On the properties of real finite-sized planar and tubular stent-like auxetic structures”. In: *physica status solidi (b)* 251.2 (2014), pp. 321–327.

- [83] Davood Mousanezhad et al. “Elastic properties of chiral, anti-chiral, and hierarchical honeycombs: A simple energy-based approach”. In: *Theoretical and Applied Mechanics Letters* 6.2 (2016), pp. 81–96.
- [84] Ramin Hamzehei et al. “2D triangular anti-trichiral structures and auxetic stents with symmetric shrinkage behavior and high energy absorption”. In: *Mechanics of Materials* 142 (2020), p. 103291.
- [85] Avelino Alves Filho. *Elementos Finitos—A base da tecnologia CAE*. Saraiva Educação SA, 2018.
- [86] Nicholas Karnesis and Gaetano Burriesci. “Uniaxial and buckling mechanical response of auxetic cellular tubes”. In: *Smart Materials and Structures* 22.8 (2013), p. 084008.
- [87] Xin Ren et al. “A simple auxetic tubular structure with tuneable mechanical properties”. In: *Smart Materials and Structures* 25.6 (2016), p. 065012.
- [88] Ming Lei et al. “3D printing of auxetic metamaterials with digitally reprogrammable shape”. In: *ACS applied materials & interfaces* 11.25 (2019), pp. 22768–22776.
- [89] LC Geng et al. “Mechanical properties of selective laser sintering (SLS) additive manufactured chiral auxetic cylindrical stent”. In: *Experimental Mechanics* 59.6 (2019), pp. 913–925.
- [90] Qiang Gao, Wei-Hsin Liao, and Chen Huang. “Theoretical predictions of dynamic responses of cylindrical sandwich filled with auxetic structures under impact loading”. In: *Aerospace Science and Technology* 107 (2020), p. 106270.
- [91] Huan Jiang, Zhennan Zhang, and Yanyu Chen. “3D printed tubular lattice metamaterials with engineered mechanical performance”. In: *Applied Physics Letters* 117.1 (2020), p. 011906.
- [92] Ali Farokhi Nejad et al. “Using finite element approach for crashworthiness assessment of a polymeric auxetic structure subjected to the axial loading”. In: *Polymers* 12.6 (2020), p. 1312.
- [93] Xiang Yu Zhang et al. “A novel combined auxetic tubular structure with enhanced tunable stiffness”. In: *Composites Part B: Engineering* 226 (2021), p. 109303.
- [94] Stefan Tabacu and Nicolae Doru Stanescu. “A theoretical model for the estimate of the reaction force for 3D auxetic anti-tetra chiral tubular structures under tensile loads”. In: *Thin-Walled Structures* 168 (2021), p. 108304.
- [95] Huan Jiang et al. “3D printed tubular lattice metamaterials for mechanically robust stents”. In: *Composites Part B: Engineering* 236 (2022), p. 109809.

- [96] Kemal Solak and Suleyman Nazif Orhan. “Performance evaluation of peanut-shaped tubular auxetics with enhanced stiffness: a finite element study”. In: *Modelling and Simulation in Materials Science and Engineering* 31.1 (2022), p. 015006.
- [97] Chuanbiao Zhang et al. “On the effective elastic constants of anti-tetra chiral tubular structure”. In: *Engineering Structures* 278 (2023), p. 115507.
- [98] XY Yang et al. “Bidirectional evolutionary method for stiffness optimization”. In: *AIAA journal* 37.11 (1999), pp. 1483–1488.
- [99] Xiaodong Huang and YM Xie. “Convergent and mesh-independent solutions for the bi-directional evolutionary structural optimization method”. In: *Finite elements in analysis and design* 43.14 (2007), pp. 1039–1049.
- [100] Ole Sigmund and Kurt Maute. “Topology optimization approaches”. In: *Structural and Multidisciplinary Optimization* 48.6 (2013), pp. 1031–1055.
- [101] Y Mike Xie and Grant P Steven. “Basic evolutionary structural optimization”. In: *Evolutionary structural optimization*. Springer, 1997, pp. 12–29.
- [102] Martin Philip Bendsøe and Noboru Kikuchi. “Generating optimal topologies in structural design using a homogenization method”. In: *Computer methods in applied mechanics and engineering* 71.2 (1988), pp. 197–224.
- [103] Tuan D Ngo et al. “Additive manufacturing (3D printing): A review of materials, methods, applications and challenges”. In: *Composites Part B: Engineering* 143 (2018), pp. 172–196.
- [104] Athul Joseph, Vinyas Mahesh, and Dineshkumar Harursampath. “On the application of additive manufacturing methods for auxetic structures: A review”. In: *Advances in Manufacturing* 9.3 (2021), pp. 342–368.
- [105] Xin Ren et al. “Auxetic nail: Design and experimental study”. In: *Composite Structures* 184 (2018), pp. 288–298.
- [106] Wonjoo Lee et al. “Effect of auxetic structures on crash behavior of cylindrical tube”. In: *Composite Structures* 208 (2019), pp. 836–846.
- [107] Hui Wang et al. “Tunable compression-torsion coupling effect in novel cylindrical tubular metamaterial architected with boomerang-shaped tetrachiral elements”. In: *Materials Today Communications* 31 (2022), p. 103483.
- [108] Farhang Momeni, Xun Liu, Jun Ni, et al. “A review of 4D printing”. In: *Materials & design* 122 (2017), pp. 42–79.
- [109] Xiao Kuang et al. “Advances in 4D printing: materials and applications”. In: *Advanced Functional Materials* 29.2 (2019), p. 1805290.

- [110] Xiaozhou Xin et al. “4D printing auxetic metamaterials with tunable, programmable, and reconfigurable mechanical properties”. In: *Advanced Functional Materials* 30.43 (2020), p. 2004226.
- [111] Dinesh Patidar and RS Rana. “The effect of CO<sub>2</sub> laser cutting parameter on Mechanical & Microstructural characteristics of high strength steel-a review”. In: *Materials Today: Proceedings* 5.9 (2018), pp. 17753–17762.
- [112] SK Bhullar et al. “Influence of negative Poisson’s ratio on stent applications”. In: *Adv. Mater* 2.3 (2013), pp. 42–47.
- [113] Faisal Amin et al. “Auxetic coronary stent endoprosthesis: Fabrication and structural analysis”. In: *Journal of Applied Biomaterials & Functional Materials* 13.2 (2015), pp. 127–135.
- [114] Hong Hu, Zhengyue Wang, and Su Liu. “Development of auxetic fabrics using flat knitting technology”. In: *Textile Research Journal* 81.14 (2011), pp. 1493–1502.
- [115] Andrews Boakye et al. “Design and manufacture of knitted tubular fabric with auxetic effect”. In: *The Journal of The Textile Institute* 109.5 (2018), pp. 596–602.
- [116] Andrews Boakye et al. “Compressive property of an auxetic-knitted composite tube under quasi-static loading”. In: *Autex Research Journal* 20.2 (2020), pp. 101–109.
- [117] Yordan Kyosev. *Braiding technology for textiles: Principles, design and processes*. Elsevier, 2014.
- [118] Sohel Rana and Raul Fangueiro. *Braided structures and composites: production, properties, mechanics, and technical applications*. Vol. 3. CRC Press, 2015.
- [119] Philippe Boisse. *Advances in composites manufacturing and process design*. Woodhead Publishing, 2015.
- [120] Ning Jiang and Hong Hu. “A study of tubular braided structure with negative Poisson’s ratio behavior”. In: *Textile Research Journal* 88.24 (2018), pp. 2810–2824.
- [121] Ning Jiang and Hong Hu. “Auxetic yarn made with circular braiding technology”. In: *physica status solidi (b)* 256.1 (2019), p. 1800168.
- [122] Ali Alavi Nia and Jamal Haddad Hamedani. “Comparative analysis of energy absorption and deformations of thin walled tubes with various section geometries”. In: *Thin-Walled Structures* 48.12 (2010), pp. 946–954.
- [123] Aniket Ingrole, Ayoun Hao, and Richard Liang. “Design and modeling of auxetic and hybrid honeycomb structures for in-plane property enhancement”. In: *Materials & Design* 117 (2017), pp. 72–83.



- [124] Kadir Günaydin, Zana Eren, and Fabrizio Scarpa. “Experimental investigation of auxetic structures subjected to quasi static axial load”. In: *2017 8th International Conference on Recent Advances in Space Technologies (RAST)*. IEEE. 2017, pp. 7–10.
- [125] Xin Ren et al. “Experimental and numerical investigations of aluminum foam-filled auxetic circular tubular metamaterials with elliptical cells”. In: *Construction and Building Materials* 374 (2023), p. 130900.
- [126] Mikhail Andreevich Volkov, Valentin Aleksandrovich Gorodtsov, and Dmitry Sergeevich Lisovenko. “Variability of elastic properties of chiral monoclinic tubes under extension and torsion”. In: *Letters on Materials* 9.2 (2019), pp. 202–206.
- [127] Raushan Singh, Pranjal Singh, and Ajeet Kumar. “Unusual extension–torsion–inflation couplings in pressurized thin circular tubes with helical anisotropy”. In: *Mathematics and Mechanics of Solids* 24.9 (2019), pp. 2694–2712.
- [128] LG Brazier. “On the flexure of thin cylindrical shells and other" thin" sections”. In: *Proceedings of the Royal society of London. Series A, containing papers of a mathematical and physical character* 116.773 (1927), pp. 104–114.
- [129] M Abbaslou, R Hashemi, and E Etemadi. “Novel hybrid 3D-printed auxetic vascular stent based on re-entrant and meta-trichiral unit cells: finite element simulation with experimental verifications”. In: *Materials Today Communications* (2023), p. 105742.
- [130] Matheus Brendon Francisco et al. “Multiobjective Design Optimization of Reentrant Auxetic Model Using Lichtenberg Algorithm Based on Metamodel”. In: (2022).
- [131] Matheus Brendon Francisco et al. “Multiobjective design optimization of double arrowhead auxetic model using Lichtenberg algorithm based on metamodelling”. In: *Structures*. Vol. 45. Elsevier. 2022, pp. 1199–1211.
- [132] Donald R Askeland et al. “The science and engineering of materials”. In: (2003).
- [133] VH Carneiro and H Puga. “Axisymmetric auxetics”. In: *Composite Structures* 204 (2018), pp. 438–444.
- [134] Hang Yang and Li Ma. “Design and characterization of axisymmetric auxetic metamaterials”. In: *Composite Structures* 249 (2020), p. 112560.
- [135] Jie Li et al. “Design and characterization of novel bi-directional auxetic cubic and cylindrical metamaterials”. In: *Composite Structures* 299 (2022), p. 116015.
- [136] Sukhwinder K Bhullar et al. “Fabrication and characterization of nonwoven auxetic polymer stent”. In: *Polymer-Plastics Technology and Engineering* 54.15 (2015), pp. 1553–1559.

- [137] Murtaza Najabat Ali and Ihtesham Ur Rehman. “Auxetic polyurethane stents and stent-grafts for the palliative treatment of squamous cell carcinomas of the proximal and mid oesophagus: a novel fabrication route”. In: *Journal of Manufacturing Systems* 37 (2015), pp. 375–395.
- [138] Caitlin E Jackson et al. “A viewpoint on material and design considerations for oesophageal stents with extended lifetime”. In: *Journal of Materials Science* 57.1 (2022), pp. 3–26.
- [139] JB Choi and RS Lakes. “Design of a fastener based on negative Poisson’s ratio foam”. In: *Cellular Polymers* 10.3 (1991), pp. 205–212.
- [140] Yan Yao et al. “A novel auxetic structure based bone screw design: Tensile mechanical characterization and pullout fixation strength evaluation”. In: *Materials & design* 188 (2020), p. 108424.
- [141] Hailun Tan et al. “Crashworthiness design and multi-objective optimization of a novel auxetic hierarchical honeycomb crash box”. In: *Structural and Multidisciplinary Optimization* 64.4 (2021), pp. 2009–2024.
- [142] ChunYan Wang et al. “Structure design and multi-objective optimization of a novel NPR bumper system”. In: *Composites Part B: Engineering* 153 (2018), pp. 78–96.
- [143] Weiwei Wang et al. “Reliability-based optimization of a novel negative Poisson’s ratio door anti-collision beam under side impact”. In: *Thin-Walled Structures* 154 (2020), p. 106863.
- [144] Faris Tarlochan. “Sandwich structures for energy absorption applications: A review”. In: *Materials* 14.16 (2021), p. 4731.
- [145] Kenneth E Evans and Andrew Alderson. “Auxetic materials: functional materials and structures from lateral thinking!” In: *Advanced materials* 12.9 (2000), pp. 617–628.
- [146] Kenneth E Evans et al. “Molecular network design”. In: *Nature* 353.6340 (1991), pp. 124–124.
- [147] Roderic Lakes. “Foam structures with a negative Poisson’s ratio”. In: *Science* 235.4792 (1987), pp. 1038–1040.
- [148] Cheng-Che Tung et al. “Bio-inspired, helically oriented tubular structures with tunable deformability and energy absorption performance under compression”. In: *Materials & Design* 222 (2022), p. 111076.
- [149] Rafael Gomes et al. “A novel dragonfly wing shape auxetic tubular structure with negative Poisson’s ratio”. In: *Smart Materials and Structures* (2024).

- [150] Swapnil Vyavahare and Shailendra Kumar. “Numerical and experimental investigation of FDM fabricated re-entrant auxetic structures of ABS and PLA materials under compressive loading”. In: *Rapid Prototyping Journal* 27.2 (2021), pp. 223–244.
- [151] Chulho Yang, Hitesh D Vora, and Young Chang. “Behavior of auxetic structures under compression and impact forces”. In: *Smart Materials and Structures* 27.2 (2018), p. 025012.
- [152] Mohammad Raquibul Hasan et al. “Potential of Recycled PLA in 3D Printing: A Review”. In: *Sustainable Manufacturing and Service Economics* (2024), p. 100020.
- [153] Mohammad Javad Ramezani and Omid Rahmani. “Potential and Applications of Auxetic Tubular: A Review”. In: *Functional Composites and Structures* (2024).
- [154] Steven A Weissman and Neal G Anderson. “Design of experiments (DoE) and process optimization. A review of recent publications”. In: *Organic Process Research & Development* 19.11 (2015), pp. 1605–1633.
- [155] Kalyanmoy Deb et al. “A fast and elitist multiobjective genetic algorithm: NSGA-II”. In: *IEEE transactions on evolutionary computation* 6.2 (2002), pp. 182–197.
- [156] Haiping Ma et al. “A comprehensive survey on NSGA-II for multi-objective optimization and applications”. In: *Artificial Intelligence Review* 56.12 (2023), pp. 15217–15270.
- [157] Yusliza Yusoff, Mohd Salihin Ngadiman, and Azlan Mohd Zain. “Overview of NSGA-II for optimizing machining process parameters”. In: *Procedia Engineering* 15 (2011), pp. 3978–3983.
- [158] Xiaolin Deng et al. “Multiobjective optimization for the crashworthiness design of bioinspired sinusoidal honeycombs”. In: *Applied Physics A* 128.5 (2022), p. 438.
- [159] Feng Jiang et al. “Blast response and multi-objective optimization of graded re-entrant circular auxetic cored sandwich panels”. In: *Composite Structures* 305 (2023), p. 116494.
- [160] Abishek Kafle et al. “3D/4D Printing of polymers: Fused deposition modelling (FDM), selective laser sintering (SLS), and stereolithography (SLA)”. In: *Polymers* 13.18 (2021), p. 3101.